



HAL
open science

Fast charging strategies of a lithium-ion battery using aging model

Sara Mohajer

► **To cite this version:**

Sara Mohajer. Fast charging strategies of a lithium-ion battery using aging model. Automatic. Université de Bordeaux, 2019. English. NNT : 2019BORD0027 . tel-04571526

HAL Id: tel-04571526

<https://theses.hal.science/tel-04571526v1>

Submitted on 8 May 2024

HAL is a multi-disciplinary open access archive for the deposit and dissemination of scientific research documents, whether they are published or not. The documents may come from teaching and research institutions in France or abroad, or from public or private research centers.

L'archive ouverte pluridisciplinaire **HAL**, est destinée au dépôt et à la diffusion de documents scientifiques de niveau recherche, publiés ou non, émanant des établissements d'enseignement et de recherche français ou étrangers, des laboratoires publics ou privés.

THÈSE PRÉSENTÉE
POUR OBTENIR LE GRADE DE

DOCTEUR DE
L'UNIVERSITÉ DE BORDEAUX

ECOLE DOCTORALE DES SCIENCES PHYSIQUES ET DE L'INGENIEUR
SPECIALITE : AUTOMATIQUE ET PRODUCTIQUE, SIGNAL ET IMAGE

Par

Sara MOHAJER
MSc Energy Science and Technology - University of Ulm

STRATEGIES DE CHARGE RAPIDE DE BATTERIES LITHIUM-ION
PRENANT EN COMPTE UN MODELE DE VEILLISSEMENT

(FAST CHARGING STRATEGIES OF A LITHIUM-ION BATTERY USING AGING MODEL)

Sous la direction de : **Jocelyn SABATIER**

Professeur, Université de Bordeaux

Co-directeur : **Patrick LANUSSE**

Maître de Conférences, Bordeaux INP

Devant la commission d'examen formée de :

MM. Thierry POINOT	Professeur, ENSIP, Université de Poitiers	<i>Président</i>
Christophe FORGEZ	Professeur, UTC, Compiègne	<i>Rapporteur</i>
Delphine RIU	Professeur, Grenoble INP, Saint Martin d'Hères	<i>Rapporteur</i>
Xavier ROBOAM	Directeur de Recherche CNRS, LAPLACE, Toulouse	<i>Examineur</i>
Olivier COIS	Directeur Industriel, Robert Bosch GmbH, Stuttgart	<i>Encadrant industriel</i>
Rainer HOERLEIN	Ingénieur, Robert Bosch GmbH, Stuttgart	<i>Invité</i>

le 05/03/2019

Laboratoire de l'Intégration du Matériau au Système – UMR 5218 CNRS

Université Bordeaux, Bordeaux INP

351 cours de la Libération-33405 TALENCE cedex- France

Titre :

Strategies De Charge Rapide De Batteries Lithium-Ion Prenant en Compte Un Modele De Vieillessement

Résumé :

Un modèle décrivant les phénomènes physiques internes de batteries lithium-ion est développé pour une détection précise de leur état, avec application au domaine de l'industrie automobile. Pour pouvoir utiliser le modèle à des fins de contrôle de charge rapide, un observateur de vieillissement est tout d'abord conçu et intégré au modèle de batterie. Dans un second temps, une stratégie de contrôle de charge rapide robuste est conçue. Elle est basée sur un contrôleur Crone capable de gérer les grandes incertitudes paramétriques du modèle de batterie tout en atteignant l'objectif de charge rapide. Enfin, quelques simplifications du modèle de batterie, de la technique d'optimisation et de la définition des profils de charge rapide sont proposées et évaluées afin de rendre l'ensemble de la stratégie de recharge rapide applicable à un système embarqué de gestion de batterie.

Mots clés :

Batteries Lithium-ion, Modele de vieillissement, Contrôle de charge rapide

Title :

Fast Charging Strategies of a Lithium-ion Battery Using Aging Model

Abstract :

A physics-based battery model is developed for an accurate state-detection of batteries in the automotive industry. In order to use the model for the purpose of fast charging control an aging observer is designed and integrated to the battery model. In a subsequent step a robust fast charging control is introduced to design a controller able to deal with large parametric uncertainties of the battery model while achieving the fast charging target. Finally some simplifications in the battery model structure, in the optimization technique and in the definition

of fast charging profiles are proposed and evaluated to make the whole model applicable for an onboard battery management system.

Keywords :

Lithium-ion batteries, Aging model, Fast charging control

Abstract

The motivation for advancement of electric vehicles and as a result, the battery management systems (BMS) has led to dedicate more research to battery modelling. Batteries are known as the most expensive component of an electric vehicle. Thus increasing the lifetime of the batteries are of great importance for the advancement of electromobility. For this purpose, advanced battery management systems have proved to be the best solution for improvement of battery lifetime and performance.

Battery state detection is based on a battery model in the battery management system. In this thesis a physics-based battery model is designed which is able to model the behavior of the battery in a wide operating range with a reasonable computational complexity. Besides that, an aging observer is included in the model to estimate the aging of the battery in terms of capacity loss. The battery model is validated using several real-world driving cycles and current profiles with RMS error of 0.0147 V in terminal voltage estimation. The model has shown a very good accuracy especially in comparison with the state of the art battery modelling approaches, while having a comparable computational effort.

In the following step, a fast charging controller is designed using a robust fractional order control strategy. The charging controller adapts the operating limitations based on the estimated capacity loss so that the fast charging target will be achieved while minimizing the battery degradation. Using the optimal charging profiles generated by a prior trajectory planning the aging is reduced up to 15% in comparison to the convenient CCCV (Constant Current Constant Voltage) charging protocol. The performance of the controller is examined by applying uncertainties in the model parameters and a good tracking accuracy is observed.

In the last chapter, several possible simplifications are proposed to be considered in the model structure, in the optimization algorithm, and in the definition of the fast charging profile patterns. Thereby, the model and the fast charging algorithms are adapted to be used for an onboard application such as the battery management system of the electric vehicles.

Résumé

Les batteries sont reconnues comme étant les composants les plus onéreux d'un véhicule électrique. Ainsi, l'augmentation de la durée de vie des batteries est d'une importance capitale vers la démarche d'électrification. Pour atteindre cet objectif, les systèmes de contrôle de batteries (Battery Management System – BMS) ont été démontrés comme étant la meilleure solution pour exploiter au maximum les capacités de la batterie et ainsi améliorer ses performances tout au long de sa vie. L'estimation des états internes de la batterie se base sur un modèle implémenté dans le BMS. Dans cette thèse, un modèle inspiré par des principes physiques a été développé : il est capable de modéliser le comportement de la batterie dans une large plage de fonctionnement avec un temps de calcul et une complexité raisonnable. De plus, un observateur de vieillissement a été inclus dans le modèle pour estimer le vieillissement de la batterie en termes de perte de capacité. Le modèle de batterie a été validé en utilisant différents cycles de conduite basés sur des mesures et profils de courant. Le modèle a montré une très bonne précision par rapport à l'état de l'art actuel des modèles de batterie, tout en ayant un temps de calcul comparable.

Dans un second temps, un régulateur de charge rapide a été développé en utilisant une commande robuste d'ordre non-entier. Le régulateur de charge adapte les limites de fonctionnement de la batterie en estimant la perte de capacité afin que le temps de charge désiré soit atteint avec un vieillissement minimal de la batterie. La performance du régulateur est évaluée en appliquant des incertitudes sur les paramètres du modèle et une bonne précision a été observée.

Dans le dernier chapitre, des simplifications sont proposées au niveau de la structure du modèle, de l'algorithme d'optimisation et de la génération de profils de courant de charge rapide. Ainsi, le modèle et l'algorithme de charge rapide sont adaptés pour être implémentés sur des systèmes embarqués à l'image du BMS.

To the memory of my father.

Acknowledgements

I would like to express my deepest appreciation to all those who provided me the possibility to complete this thesis. A special gratitude I give to my advisors at the university, Prof. Dr. Jocelyn Sabatier and Dr. Patrick Lanusse, whose suggestions and encouragements helped me to coordinate my project. I thank them for their consistent support, patience, and inspirations during my thesis work. They made me realize that sometimes, a deep understanding of the problem and doing a careful analysis in a simpler way can be more efficient and beautiful than a complicated numerical simulation. I am also truly grateful to them for the wonderful and memorable trips to Bordeaux.

Furthermore, I would also like to acknowledge with much appreciation the crucial role of the staff of *Bosch Battery Systems GmbH* and our department leader Dr. Olivier Cois, who gave me the permission to conduct this research and use all the required equipment and the necessary material for my thesis. Discussions with Dr. Cois also greatly encouraged me to pursue my career as an engineer in industry. His intelligent way of dealing with real world engineering challenges and profound problem solving technique inspired me to think out of the box and helped me in developing my professional skills. Another appreciation goes to my teammates, who helped me by giving brilliant suggestions for improving the results. I would like to thank my wonderful colleagues, Vincent, Sergio, Julia and Sabine; especially for our cheerful chats during the coffee breaks. Furthermore, I truly appreciate their help for preparing the French summary of my thesis. The friendship I developed there is an unforgettable memory.

Finally yet importantly, I would like to appreciate the support and love of my family, my beloved father, my dearest mother and my amazing sisters who despite the distance between us have always brought hope and happiness to my life. I would like to thank my husband Milad, whose love made my life much enjoyable and colorful and his support gave me a lot of strength, and motivated me going through some of the difficult days of my PhD life.

Table of Contents

Chapter 1	1
1.1 Electromobility emersion and evolution	2
1.2 Principles of Lithium ion battery	3
1.3 Challenges in the field of electromobility, battery management system, a promising solution	5
1.4 Overview of the dissertation	7
Chapter 2	10
2.1 Introduction	11
2.2 Different battery modelling approaches	11
2.3 Fractional battery model	15
2.3.1 Model calibration	19
2.3.2 Model validation	22
2.4 Conclusion and future work	24
Chapter 3	26
3.1 Introduction	27
3.2 Function-based model for electrode potential	28
Figure 3-1 ELcell setup for potential measurement (described in - ELcell setup	30
3.3 Concentration profile in the electrodes	31
3.4 OCV formula for the cell at Begin Of Life (BOL) and Middle Of Life (MOL)	31
3.4.1 Derivation of OCV formula for aged cells at MOL.....	32
3.5 Balancing: a requirement for optimization problem	34
3.6 Aging correction of OCV curve at MOL	37
3.7 Conclusion and future work	39
Chapter 4	41
4.1 Review on aging mechanisms and aging modelling techniques	42
4.1.1 Classification of aging mechanisms based on location in the cell	43
4.1.2 Classification of aging mechanisms based on time	45
4.2 Implementation of electro-thermal aging model	49

4.2.1 Thermal model	49
4.2.2 Aging Model	50
4.3 Validation of the coupled Electro-thermal aging model	59
4.3.1 Validation of the Electro-thermal Model	59
4.3.2 Validation of Aging Model	60
4.4 Conclusion and future work.....	64
Chapter 5.....	65
5.1 Concept of intelligent charging and bibliography analysis.....	66
5.2 Trajectory planning	68
5.3 Model linearization	71
5.4 State-space representation of the nonlinear battery system	71
5.5 Determination of the system operating points.....	72
5.6 Uncertain linear model of the nonlinear battery model.....	73
5.7 Robust controller design.....	74
5.7.1 Overview of control system design and performance assessment	74
5.7.2 Closed-loop control.....	78
5.7.3 CRONE controller design	84
5.7.4 CRONE controller performance analysis	87
5.8 Conclusion and future work.....	90
Chapter 6.....	92
6.1 Empirical simplification of charging profiles.....	93
6.1.1 Affine profile pattern	94
6.1.2 Polynomial profile pattern	95
6.2 Simplifications in the structure of the battery model.....	97
6.2.2 Simplification of the nonlinear thermal model by Volterra series	102
6.3 Simplification in the optimization scheme	112
6.4 Conclusion and future work.....	116
Chapter 7.....	120
Appendix A - <i>ELcell</i> setup	125

LIST OF FIGURES

Figure 1-1 Evolution of electromobility [1]	3
Figure 1-2 Schematic diagram of a Li-ion battery and main reactions [2]	4
Figure 1-3 Schematic diagram of a PHEV pack manufactured by A123 Systems	6
Figure 2-1 Single particle model (on the right) based on spatial discretization of a fully electrochemical model along x-axis (on the left). Having only one particle for each electrode, we can consider the value at each node to be an averaged quantity over the electrode [22].....	13
Figure 2-2 Different types of battery models used in battery management systems (Single particle and Pseudo-two dimensional models from [24])	15
Figure 2-3 Concentration gradient through the sphere, representing the single particle model .	16
Figure 2-4 Comparison of $G(s)$ and its approximation $H(s)$	16
Figure 2-5 Comparison of fractional transfer function and its approximation in a frequency domain limited to the range including the BMS sampling frequency (approx. 70 rad.s^{-1}).	18
Figure 2-6 Block diagram implementation of the electrical fractional model	18
Figure 2-7 OCP curves of Anode (left) and Cathode (right) against the respective lithiation degree	21
Figure 2-8 Validation results of applying extended Artemis drive cycle to the fractional model .	23
Figure 2-9 Voltage simulation and respective absolute estimation error for fractional battery model and order 7 ECM.	24
Figure 3-1 ELcell setup for potential measurement (described in Appendix A)	30
Figure 3-2 OCP fitting at BOL (for the negative electrode (left) and the positive electrode (right)	30
Figure 3-3 Model of cell with two connected tanks (similar concept proposed in [44])	31
Figure 3-4 Flowchart showing the cell balancing algorithm.....	35
Figure 3-5: balancing error surface.....	36
Figure 3-6: OCP balancing and reconstructed OCV.....	37
Figure 3-7: Balanced anode OCP fitting and the respective error	37
Figure 3-8: Balanced cathode OCP fitting and the respective error	38
Figure 3-9 Comparison of balanced OCPs and reconstructed OCV	38
Figure 3-10 Aged OCV correction (comparison of model and measurement (top) and its respective error (bottom))	39
Figure 4-1 Aging mechanisms on anode and its interphase with electrolyte [48].....	44
Figure 4-2 Aging mechanisms on cathode and its interphase with electrolyte [4]	45
Figure 4-3 Calendar aging measurement results for SDI prismatic cells.....	46
Figure 4-4 cyclic test results - aging as a function of (a): cycle depth, (b): temperature, and (c): C-rate	48
Figure 4-5 Schematic diagram showing capacity loss caused by crack propagation on anode [53].....	48
Figure 4-6 SDI 28 Ah cell opening at BOL	52
Figure 4-7 SDI 28 Ah cell opening at EOL	52

Figure 4-8 Full cell with reference electrode	53
Figure 4-9 Variation of half-cell OCPS and full-cell OCV curves with aging.....	54
Figure 4-10 Desired intercalation reaction vs. undesired SEI formation at the interphase of anode and electrolyte [64]	54
Figure 4-11 SEI layer thickness growth	57
Figure 4-12 Aging map obtained by interpolation of measurement points at different C-rates in SOC range of 15-95%	57
Figure 4-13 Coupled electro-aging thermal model [71].....	59
Figure 4-14 Comparison of simulated and measured voltage and the respective absolute error under dynamic driving cycle	60
Figure 4-15 Aging model requirements	61
Figure 4-16 Investigation of temperature effect on aging	61
Figure 4-17 1C and 3C charging profiles and respective cycle depth	62
Figure 4-18 1C and 3C validation profiles and corresponding temperature and capacity loss ...	62
Figure 4-19 Cyclic behavior of the electro-thermal aging model using two different profiles	63
Figure 4-20 Investigation of C-rate and SOC effect on aging	63
Figure 5-1 Fast charging function in BMS.....	66
Figure 5-2 Trajectories obtained at $T=35^{\circ}\text{C}$ for a cell at BOL in SOC range of 5-80% with fixed charging time of 20 minutes	70
Figure 5-3 Determination of operating points for an optimal charging profile at 10°C and BOL.	73
Figure 5-4 Frequency responses of transfer function $J_{sr}(s)/I_{ch}(s)$ for various operating points ...	74
Figure 5-5 Unity-feedback control system.....	75
Figure 5-6 Feedback-Feedforward control system	77
Figure 5-7 Criteria for analysis of stability degree.....	78
Figure 5-8 Closed-loop configuration for the fast charging control.....	79
Figure 5-9 Robustness of stability degree in presence of uncertainties for 2 nd generation CRONE controller	81
Figure 5-10 Generalized template for the 3 rd generation of CRONE controller	82
Figure 5-11 Nichols chart of the nominal plant and associated uncertainties	85
Figure 5-12 Magnitude plots of the four sensitivity functions	86
Figure 5-13 3 rd generation CRONE controller	86
Figure 5-14 Block diagram of the fast charging controller	87
Figure 5-15 Reference tracking in case of parameter variations.....	88
Figure 5-16 Cascade charging controller	89
Figure 5-17 Charging in presence of process uncertainties using the cascade controller	90
Figure 6-1 Affine-shape profile pattern.....	94
Figure 6-2 Polynomial-shape profile pattern	95
Figure 6-3 Performance comparison of the optimal patterns with state of the art CCCV.....	96
Figure 6-4 Current profile for validation of the second proposal.....	98
Figure 6-5 Side reaction current (I) by assuming a variable SEI thickness (II) by assuming a constant SEI thickness and (III) relative error of both cases	98
Figure 6-6 Cell terminal voltage (I) before and (II) after breaking the j_{sr} loop	99
Figure 6-7 Simplified model of the electrodes	100

Figure 6-8 Coupled aging-thermal- Butler-Volmer model after simplification 100

Figure 6-9 Variation of the electrode overpotential against input current in Butler-Vomer sub-model 101

Figure 6-10 Input-Output System representation of coupled thermal-BV sub-model 102

Figure 6-11 Block diagram of the first order Volterra kernel 105

Figure 6-12 Block diagram of the second order Volterra kernel 106

Figure 6-13 Simplified block diagram of the second order Volterra kernel 107

Figure 6-14 Simplified block diagram of the third order Volterra kernel 108

Figure 6-15 Replacing the Thermal-BV sub-system by its Volterra approximated equivalent ... 108

Figure 6-16 Interconnection of the elementary blocks with a simpler structure 108

Figure 6-17 Magnitude Bode plot of the Volterra kernels: (a) first kernel magnitude plot, (b) second order kernel magnitude plot third order kernel magnitude plot at frequencies of (c-1) $\omega_3 = 0.01\text{rads}$, (c-2) $\omega_3 = 1\text{rads}$, and (c-3) $\omega_3 = 100\text{rads}$ 109

Figure 6-18 Comparison of Nonlinear model and Volterra-based model in aging estimation .. 110

Figure 6-19 Optimization cost function against iteration number 111

Figure 6-20 Optimization results and respective aging estimated by the nonlinear model 112

Figure 6-21 Gradient-based dichotomous optimization 114

Figure 6-22 Comparison of Matlab fmincon optimizer with self-written gradient-based dichotomous optimization method in minimization of capacity loss 116

Figure 6-23 Charging profile optimization framework using the concepts introduced in chapter 5 and 6 118

LIST OF TABLES

<i>Table 2-1 Prismatic Samsung SDI 28 cell specifications from manufacturer</i>	19
<i>Table 2-2 Electrochemical model parameters for Samsung SDI 28 Ah PHEV cells ((1) and (2): the method used to obtain electrode stoichiometries are explained in details in chapter 3)</i>	21
<i>Table 4-1 Calendar life test specifications</i>	46
<i>Table 4-2 Cyclic life test specifications</i>	47
<i>Table 4-3 Lumped thermal parameters</i>	49
<i>Table 4-4 Half-cell capacity measurements for SDI 28 Ah at BOL and EOL</i>	53
<i>Table 4-5 Aging model parameters</i>	55
<i>Table 5-1 Battery state and output variables</i>	72
<i>Table 5-2 Unity-feedback Control system components</i>	75
<i>Table 6-1 Test specification for validation of Volterra-based model</i>	110
<i>Table 6-2 Sensitivity analysis of cost function C_{loss} versus optimization parameter d</i>	114

GLASSORY

EV: Electric Vehicle

PHEV: Plug-in Hybrid Electric Vehicle

HEV: Hybrid Electric Vehicle

BMS: Battery Management System

MOR: Model Order Reduction

SPM: Single Particle Model

P2D: Pseudo-two Dimensional

CCCV: Constant Current Constant Voltage

MCC: Multi-stage Constant Current

ARTEMIS: Assessment and Reliability of Transport Emission Models and Inventory Systems

SEI: Solid Electrolyte Interphase

RMS: Root Mean Square

EIS: Electrochemical Impedance Spectroscopy

BOL: Begin of Life

MOL: Middle of Life

EOL: End of Life

SOC: State of Charge

SOH: State of Health

C-rate: Current rate

CRONE: Commande Robuste d'Ordre Non Entier

Chapter 1

INTRODUCTION

1.1 Electromobility emersion and evolution	2
1.2 Principles of Lithium ion battery	3
1.3 Challenges in the field of electromobility, battery management system, a promising solution	5
1.4 Overview of the dissertation.....	7

1.1 Electromobility emersion and evolution

The desire to reduce the greenhouse gas emission and the pollution caused by fossil fuels such as gasoline and diesel in the recent years has led into looking for more environmentally friendly and sustainable alternatives. Among the currently available renewable energy sources, chemical storage systems are highly reliable. The most important feature makes them more widely used, is providing the portable power to many applications. Chemical storage is the most popular mean of using renewable energy storage systems. The batteries, which are studied in this work, are the kind of electrochemical systems that convert the electrochemical energy into electricity as a result of certain chemical reactions. Due to the high energy and power density and excellent performance of Lithium ion batteries, they are widely used as a portable power source in many applications such as laptop computers, load-leveling systems in homes and electric vehicle that is studied in this work.

Figure 1-1 represents the step-by-step evolution of electrification in the automotive industry over time. The introduction of electrification begins with development of micro-hybrid vehicles with start/stop systems at standstill and low speed, and coasting at higher speeds or including braking energy recovery systems. Increase of electrification level was followed by emersion of mild-hybrid electric vehicles initially equipped with electric motor assist systems and boost recuperation modules. Next level of electrification was achieved by production of full-hybrid and plug-in hybrid electric vehicles incorporating pure electric drives, but still in presence of an internal combustion engine. Finally, the ultimate level of electrification was introduction of battery electric vehicles simply referred as electric vehicles, where internal combustion engines are replaced by a high voltage (HV) battery and electric drives.

For the development of future powertrain systems, the main market driver is CO₂-reduction. As shown on the diagram in figure 1-1, the best alternative to achieve this target is using the pure electric vehicles. However, higher levels of electrification lead to increase of respective manufacturing costs. Among the electric vehicle components, usually the battery is the most expensive component. Hence, the performance, cost and durability of the energy storage are critical for the overall feasibility, commercialization and mass production of electric vehicles.

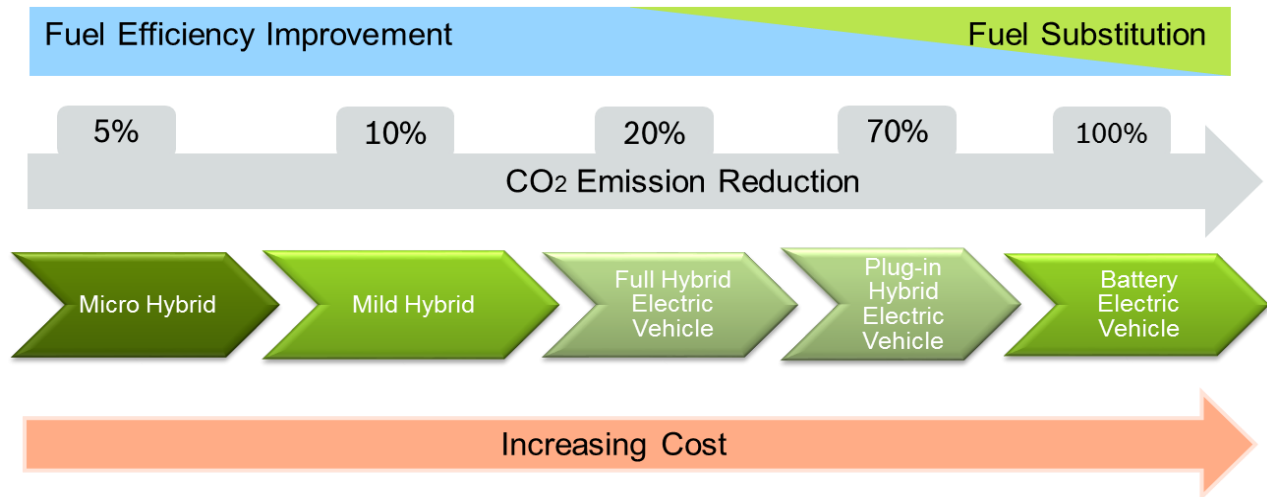


Figure 1-1 Evolution of electromobility [1]

Nowadays, high voltage Li-ion batteries are commonly used in the automotive industry whether in Electric Vehicles (EV), Hybrid Electric Vehicles (HEV), or Plug-in Hybrid Electric Vehicles (PHEV). For the efficient use of batteries in such applications, it is crucial to understand the characteristics of the Lithium ion batteries. Generally, those characteristics are related to the underlying electrochemical reactions, migration and diffusion of chemical species during charging and discharging inside the batteries, which is briefly explained in next section.

1.2 Principles of Lithium ion battery

Li-ion batteries are nowadays considered as the best candidates to promote commercialization of electric vehicles thanks to their good power and energy characteristics. A schematic view of the most commonly used Li-ion batteries is depicted in Figure 1-2. The main working principle of Li-ion batteries is as follows. During the charging process the positive electrode (Cathode) releases the Li ions to the negative electrode (Anode) referred as intercalation or insertion reaction (1-1). The discharge process negative electrode supplies the positive electrode with Li ions known as de-intercalation or extraction reaction (1-2).

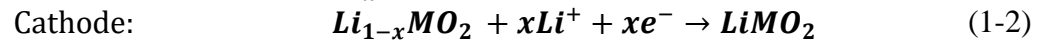
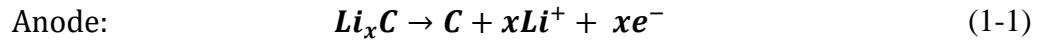
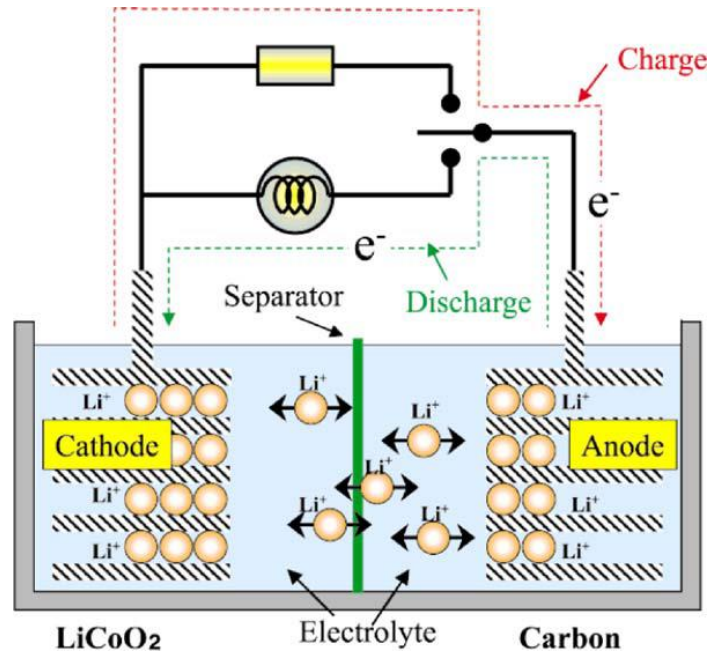


Figure 1-2 Schematic diagram of a Li-ion battery and main reactions [2]

There exists a diverse range of Li-ion batteries depending on the technology and the material used for anode, cathode, electrolyte, and separator. Most Li-ion batteries use carbon materials such as graphite and hard carbon as the anode active material. Some metal oxides, such as Lithium Titanate ($Li_4Ti_5O_{12}$) and Niobium Pentoxide (Nb_2O_5), can also be used as an anode active material. These anode active materials also referred as intercalating material, accept Li ions when charged and release them during discharge. The reaction potentials for these materials are much lower than that of standard hydrogen electrodes. Therefore, the electrolyte should be stable even at these lower potentials. This is the reason why organic electrolytes that consist of organic solvents and lithium salts are used for Li-ion batteries rather than aqueous electrolytes. The cathode active materials should contain elemental Lithium in the composition to provide a Li-ion source for cell reactions with the conventional anode active materials. Lithium cobaltate ($LiCoO_2$) was used as the cathode active material during the first stage of Li-ion battery commercialization. A similar compound, $LiNiO_2$, had also been studied intensively. However, it was not used because of its thermal instability. Substituted derivatives of this compound, formulated as $LiM_xNi_{1-x}O_2$ (M:

metal element other than nickel such as Co, Mn, Al, Mg), were developed instead and used in several applications [3].

Li-ion batteries have high single-cell voltages of approximately 3-4.3 V, which is due to the lower potentials of the anode active materials. The high specific energy of Li-ion cell is a result of its high cell voltage, because specific energy is the product of the cell voltage and the specific capacity, where 3–4.3 V is an extraordinarily high cell voltage for secondary batteries. The specific energies for Li-ion batteries are 1.5 times as large as that for Ni-MH batteries, of which the single-cell voltage is only 1.2 V, despite having specific capacities greater than those of Li-ion batteries [4].

In this study, a prismatic Li-ion cell with 28 Ah nominal capacity manufactured by *Samsung SDI* (*SDI* stands for *Samsung* with the initial letter *S*, *'Display'* and *'Digital'* with *D* and *'Interface'* and *'Internet Component'* with *I*), referred as *SDI 28 Ah* cells. This cell has been used in production of the plug-in *Porsche Cayenne S E-Hybrid* cars. It has energy capacity of 10.8 kWh, which enables an all-electric driving range of 18 to 36 km, depending on the driving style and route topography. It can be fully charged from a normal household power socket in less than four hours. By using a high current power supply, the charging time is almost halved to two hours [5]. The cell anode is made of Graphite and the material of the cathode is a 1:1:1 composition of Nickel, Manganese, and Cobalt (referred as NMC). The cell electrolyte is mainly composed of ethylene carbonate (EC), dimethyl carbonate (DMC), and ethyl methyl carbonate (EMC) (simply can be referred as EC/DMC/EMC electrolyte) with 1:1:1 ratio.

1.3 Challenges in the field of electromobility, battery management system, a promising solution

As discussed in section 1.1, one of the barriers to commercialization of electrified vehicles is high investment and manufacturing costs. Various solutions exist to reduce the costs such as standardization of cell and pack production, employing new business strategies, and utilizing advanced technologies such as high-energy materials for production of electrodes. But among all the alternatives, incorporating a Battery Management System (BMS) in the battery pack, is identified as the most promising and viable solution [6–8].

Battery management involves implementing functions to monitor the state of the battery and taking predictive measures to optimize the system performance. BMS, is a protective device built into the battery packs that can ensure optimum use and safe operation of the batteries.

To maintain safe operation and preventing the misuse of the batteries, BMS sets limitations on the peak voltage and minimum voltage of each cell during charging and discharging. The BMS also controls the maximum charging and discharging currents and monitors the cell temperature to avoid hazardous reactions such as thermal runaway [9].

Another obstacle for further commercialization of Li-ion batteries is their lifetime. In order to improve the battery longevity, the operation methods of batteries should be optimized. The operation during discharge depends mainly on the demand of the user, while the charging method can be optimized by the manufacturer to minimize the battery degradation and the charging time. Therefore, one of the important tasks of BMS is control of charging and discharging of the batteries. During charging, the BMS prevents overcharging of the cells. During discharge it monitors the level of discharge and by tracking the State of Charge (SOC), it interrupts the discharge current when the battery is empty and signals the value to the user of the portable device. A schematic diagram of a battery pack is shown in Figure 1-3 including main components such as BMS, cell, etc.

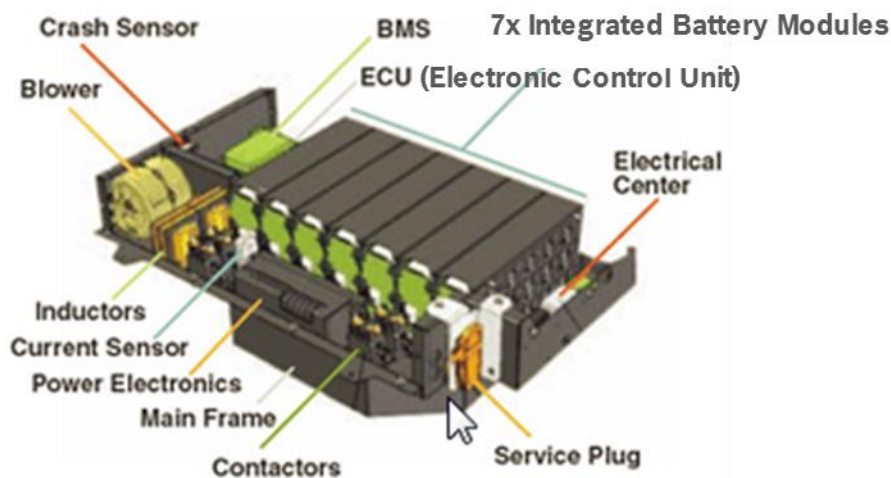


Figure 1-3 Schematic diagram of a PHEV pack manufactured by A123 Systems

BMS performs the mentioned tasks by monitoring SOC, the remaining usable capacity or in other words State of Health (SOH), the internal cell temperature and by controlling the battery

charging current. State prediction can only be achieved based on analysis of an advanced battery model that is able to show the battery behavior with its physical and electrochemical properties, and can accurately capture the battery dynamics

Significant number of studies have been devoted for further advancement of battery modelling and state detection to design more accurate and less conservative battery management systems. For example, one of the main motivations to have a more accurate and reliable BMS, is to extend the usable capacity of the cell (i.e. utilizing greater SOC range) by setting dynamic voltage limits rather than constant voltage limits used by conventional BMS units. Extending the usable capacity permits to increase the limited driving range of the electrified vehicles, which is a major disadvantage comparing to convenient cars with combustion engines. This goal can be achieved by a precise aging estimation, temperature and power prediction and physics based battery resistance model.

There are some challenges associated with the modeling of batteries. Batteries are not stationary and their dynamical behavior depends on many parameters like temperature, SOC, etc. Besides that, in general the electrochemical storage systems and so batteries, are highly nonlinear [10]. Most of the battery parameters cannot be measured but should be estimated by designing a proper state observer. Thus, it is necessary to devote more resources on development of advanced battery models and battery management systems.

1.4 Overview of the dissertation

In this dissertation, chapter 2 is devoted to an overview of various battery modelling approaches. The fractional battery model is chosen as the best candidate for modeling of the PHEV cell under investigation. Subsequently implementation, calibration and finally validation of the fractional model is explained in details.

Chapter 3 proposes a precise model for estimation of Open Circuit Voltage (OCV), which is the main contributor to the cell terminal voltage. The method is afterwards extended to consider aging effects and their impact on the OCV curves, followed by some validation results.

In chapter 4, firstly the degradation mechanisms of batteries are comprehensively investigated. In the following sections, the aging mechanisms of the case study are identified by interpreting the results of some aging measurements. Afterwards, mathematical techniques are introduced to simulate the aging of the cells with high accuracy and reasonable computational

effort. A thermal model is also implemented and calibrated to be coupled to the aging model and to consider the temperature effect on degradation. Validation tests have been carried out to verify the accuracy of the coupled electro-thermal aging model.

Chapter 5 summarizes different open-loop and closed-loop strategies to optimize the operation of batteries during fast charging. Afterwards, a closed-loop method is proposed which permits to minimize the aging effects during fast charging of batteries in presence of large parametric uncertainties. The method is explained in details in subsequent sections. As a first step, offline trajectory planning is performed to collect optimal charging profiles, then using a numerical linearization technique the battery model is linearized. In the next step, the linearized model is used to identify the operating points of the system. By observing a large uncertainty in the phase and magnitude of the linearized model of the original nonlinear battery model, a robust control methodology is introduced and used to design a fractional-order controller for achieving the intelligent charging targets. Finally, the performance of the controller is analyzed by applying some uncertainties to the parameters of the model.

Chapter 6 is dedicated to improve the simulation time of the model-based charging profile optimization (introduced in chapter 5) in order to make it appropriate for an onboard application. Possible simplifications are proposed in subsequent sections regarding the definition of fast charging profiles, the structure of the battery model and finally the optimization scheme. Validity of each proposal is verified by showing some simulation results.

Chapter 2

AN OVERVIEW OF BATTERY MODELLING APPROACHES WITH AN EMPHASIS ON FRACTIONAL MODELLING AND ITS IMPLEMENTATION

Summary

2.1 Different battery modelling approaches.....	11
2.2 Fractional battery model	15
2.2.1 Model calibration	19
2.2.2 Model validation	22
2.3 Conclusion and future work.....	24

2.1 Introduction

Previous chapter has shown the interest of battery models for the design of battery management systems. After a comparison of battery models proposed in the literature, this chapter focuses on fractional order model:

- how it is obtained
- how it can be implemented
- how it can be calibrated

In the final sections of this chapter, several validation results will verify the accuracy of the implemented fractional battery model.

2.2 Different battery modelling approaches

The battery model simulates the behavior of the system in response to different operating conditions. It should be able to represent the underlying electrochemical phenomena with optimized number of parameters and reasonable computational effort. The two main classes of models proposed in the literature for lithium-ion batteries modelling [11] are:

- equivalent circuit models;
- electrochemical models.

Equivalent circuit models (ECM) include large class of battery models in the literature such as enhanced equivalent circuit models including Kalman filter proposed by Plett [12] or purely impedance-based models developed by Buller *et al.* [13]. ECM describes the underlying phenomena in the batteries by employing usually a combination of capacitors, resistors, voltage sources, and lookup tables. Capacity fade is often represented by a capacitor with a decreasing capacity, while temperature dependence is modeled by a resistor-capacitor combination. Current research in this area includes adopting the circuit based models by continuously updating the parameters using the data obtained from current and voltage measurement. Such models can be simulated very quickly but are not accurate outside of the operating conditions for which they were developed or as the battery degrades. The parameters also lack any physical meaning, limiting the physical insight that can be gained from these models. Another disadvantage associated with ECM is its limited prediction capability compared to physics-based electrochemical models. These models usually neglect mass-transfer limitations due to solid-phase diffusion, resulting in

prediction errors when used over a wide operating region. Despite these limitations, ECMs are popular in development of BMS software because of the very low computational requirements of simulation. [14]

Electrochemical models are promising candidates for development of advanced battery management systems. They provide the possibility to interpret the model response based on real physical parameters. Physical models for battery state detection was firstly introduced by John Newman [15]. This model is based on well-proven electrochemical and thermodynamic concepts, and describes the mechanisms that take place in the battery during operation. Two main classes of electrochemical model are found in the literature summarized as follows:

Pseudo-two-dimensional models (P2D): The P2D models include diffusion in the solid-phases and electrolyte as well as cell kinetics governed by Butler-Volmer equation with in-depth details. It has two independent spatial variables: x dimension, to track the variables across the thickness of the cell, and r dimension to track the lithium concentration radially in the solid electrode particles. Having multiple spatial variables increases the number of equations to be solved and leads to a very high computational effort. Thus by having numerous coupled nonlinear partial differential equations (PDEs), simulation time may take from seconds to minutes. An extensive review on P2D electrochemical model is done by Jokar *et al.* [16]

Single Particle Model (SPM): The SPM includes the effects of transport phenomena in a simple way, thereby making electrochemical models realizable for on-board applications. In this model, a detailed distribution of local concentration and potential in solution phase are ignored to increase computational run time without compromising accuracy. The SPM is simple and fast in the simulation. The only bottleneck is its limited application only for cells with thin electrodes (mainly high power cells used for HEV and PHEV application) and high C-rates usually greater than 5 C (*C-rate*: charging or discharging current normalized against the cell capacity). A simple schematic of the model is presented in **Figure 2-1**.

The efficiency of the single particle fractional models for modelling and state of charge estimation was highlighted in several studies [17–21]. SPM should be simplified without sacrificing its accuracy to implement a model appropriate for real-time applications. Several techniques have been developed to approximate the partial differential equations representing an electrochemical model by ordinary differential equations.

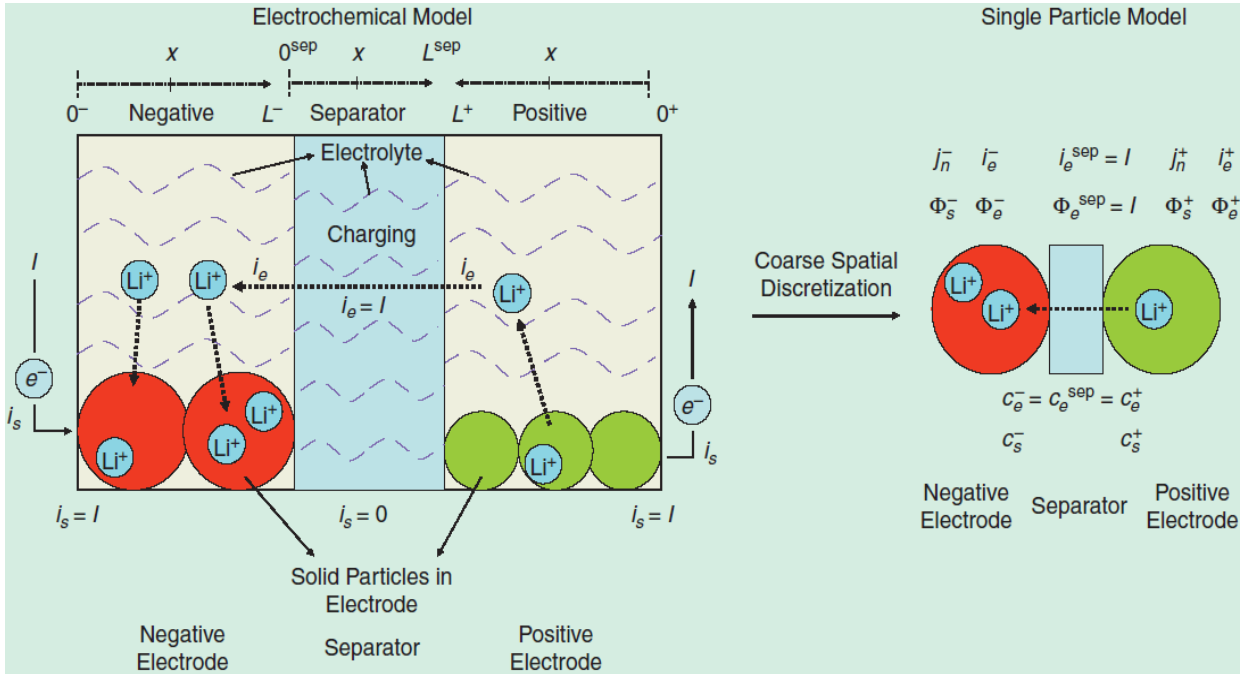


Figure 2-1 Single particle model (on the right) based on spatial discretization of a fully electrochemical model along x -axis (on the left). Having only one particle for each electrode, we can consider the value at each node to be an averaged quantity over the electrode [22].

Single particle model developed by Chaturvedi *et al.* [22] involves numerical techniques to discretize the spatial domain to yield a system of Differential Algebraic Equations (DAE). The main assumption is regarding volume-averaged quantities for the states, e.g. average concentration through that electrode. This assumption may not be valid for other types of cell chemistry such as EV cells with thick electrodes or batteries used for high power applications such as power tools where the average surface concentration in the solid phase does not match the concentration along x axis. In this work, Model Order Reduction (MOR) is used to further simplify the model structure but it leads to generate coefficients for the model, difficult to physically interpret.

Another interesting study in this field is done by Gu and Wang [23]. They designed a thermal-electrochemical coupled model of a lithium ion cell used in electric vehicles within a Computational Fluid Dynamics (CFD) framework. Their 2D electrochemical model considers ohmic and reaction heat generation effects. The ion concentration profile within the spherical particle is resembled to a parabolic profile. This kind of profile can describe the concentration gradient under steady state conditions with a good accuracy but unable to simulate the transient behavior. Thus its application is limited to the cells with sluggish electrochemical reactions. To

address the limitations of Wang's study, Smith [15] found a 5th order transfer function using Finite Element Method (FEM) for solid state diffusion and incorporated the transient solid state Li diffusion sub-model into the previously developed CFD model of Gu and Wang [23]. The problem with such an approach using FEM, is the way to obtain finite element node sizes. They are usually obtained by trial and error and may not be optimal at long times or different operating condition.

The fractional order electrochemical model of Sabatier *et al.* [20, 21] is built upon the CFD model originally proposed by Smith by including transient and steady state diffusion effects. The novelty of this model is suggesting several simplifying hypotheses and introduction of a fractional model as an approximation for the analytical solution of the diffusion equation involving only two tuning variables. The frequency domain approximation used for this model is based on fractional calculus, which is a branch of mathematics, specifically applicable to model the diffusion phenomena in highly complex systems such as ultra-capacitors, fuel cells, and batteries.

However the developed model by Sabatier *et al.* [20, 21] does not take into account neither aging nor cell thermal behaviour. These limitations have been addressed in this work that provides an electrochemical model,

- with a reduced number of parameters due to fractional parts to take into account diffusion phenomenon,
- accurate even thermal and state of health variations.

This topic is discussed in details in chapter 4. Moreover and in relation to the other existing models in the literature, the proposed physically-based battery model describes the dependency of degradation mechanisms to SOC, temperature and C-rate. This feature provides a very good agreement of the model to the experiments.

Considering the requirements and characteristics of the cell under investigation (PHEV cell) and based on the mentioned features of the fractional electrochemical model [20, 21], this class of battery modelling is employed in this study. As a summary, comparison of main classes of battery modelling approaches used for application of vehicular BMS is shown on **Figure 2-2**. ECM provides the least demanding method to model the cell behavior with the minimum accuracy, while fully electrochemical P2D model offers a detailed behavior of the cell with high computational effort. It can be concluded from the literature review presented in this section and also on the diagram, that the single particle model is a good compromise between accuracy and complexity.

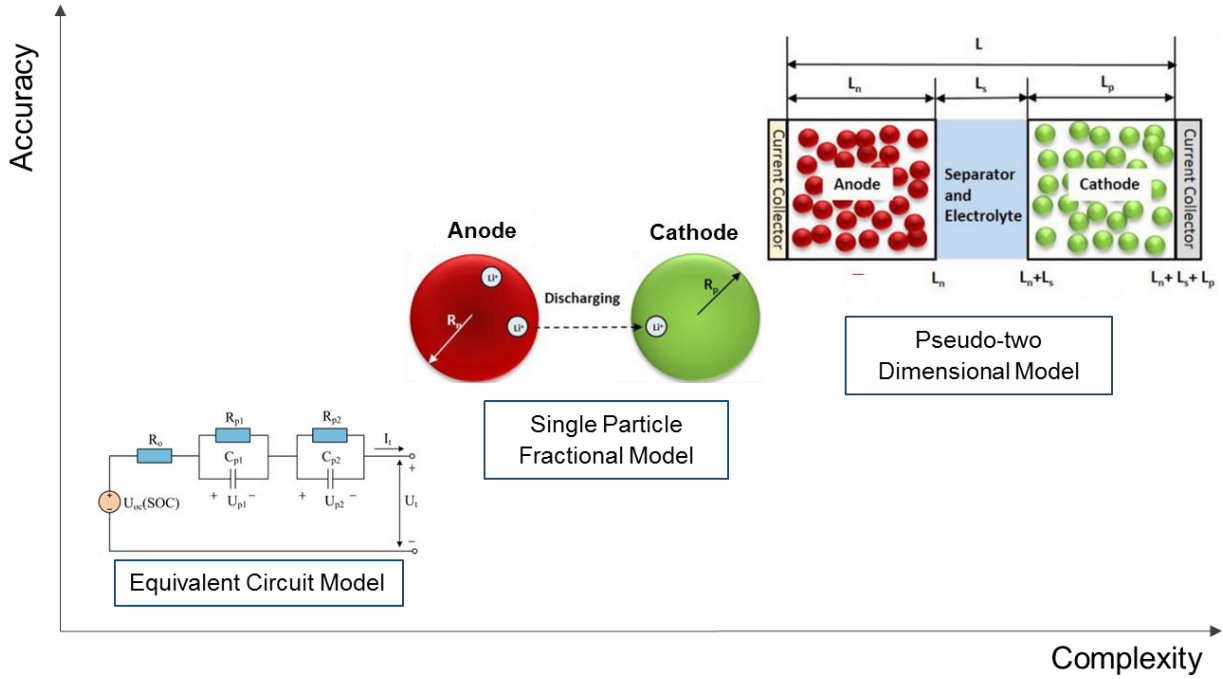


Figure 2-2 Different types of battery models used in battery management systems (Single particle and Pseudo-two dimensional models from [24])

2.3 Fractional battery model

Fractional battery modeling is based on the solution of Fick's first law of diffusion and by employing several simplifying hypotheses [20, 21] in relation to Smith's model [15]. According to Fick's law and if a cell electrode is viewed as a single spherical particle [25] (see **Figure 2-3**), lithium ions concentration gradient in the particle is described by the following relations:

$$\frac{\partial c_s}{\partial t} = \frac{D_s}{r^2} \frac{\partial}{\partial r} \left(r^2 \frac{\partial c_s}{\partial r} \right) \quad \left\{ \begin{array}{l} \frac{\partial c_s}{\partial t} \Big|_{r=0} = 0 \\ D_s \frac{\partial c_s}{\partial r} \Big|_{r=R_s} = -\frac{j_{mean}^{Li}}{a_s F} \end{array} \right. \quad (2-1)$$

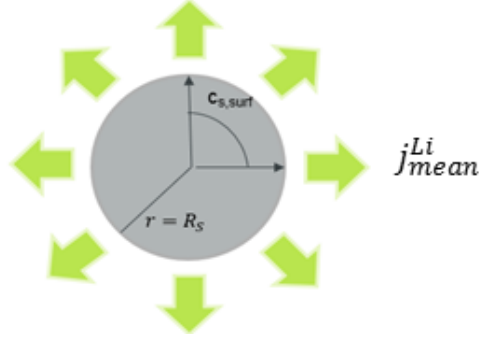


Figure 2-3 Concentration gradient through the sphere, representing the single particle model

In relation (2-1), D_s is the diffusion coefficient, r is the radius of the sphere, and $J_{\text{mean}}^{\text{Li}}$ is the average current density. Analytical solution of such a differential equation is the following transfer function:

$$G(s) = \frac{C_s|_{r=R_s}}{J_{\text{mean}}^{\text{Li}}(s)} = - \frac{R_s}{FD_s a_s \left(\sqrt{\frac{s}{D_s}} \coth \left(\sqrt{\frac{s}{D_s}} R_s \right) - 1 \right)}. \quad (2-2)$$

An analysis of the Bode diagram of $G(s)$ has been proved that a simplified transfer function $H(s)$, defined by (2-3), can approximate the dynamics of the battery in the best way with only two parameters simplifying the original transfer function:

$$H(s) = \frac{K_1}{s} \left(1 + \frac{s}{\omega_{cs}} \right)^{0.5}. \quad (2-3)$$

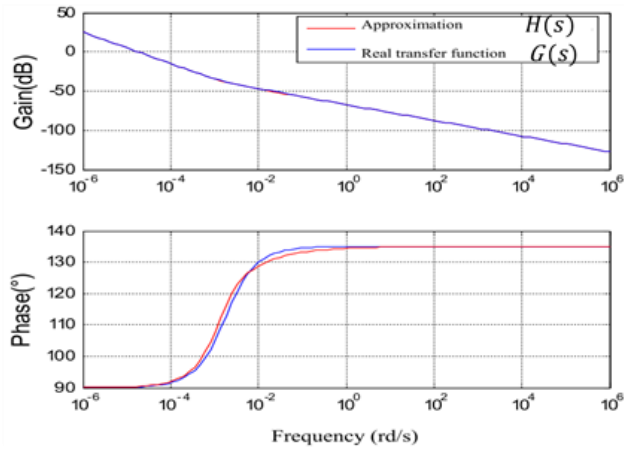


Figure 2-4 Comparison of $G(s)$ and its approximation $H(s)$.

There exists other possibilities to do a frequency-domain approximation such as using Pade approximation used by Prasad and Rahn [26]. The disadvantage of employing *Padé approximation* is that it generates too many coefficients for the approximated transfer function without a physical meaning that cannot be easily interpreted. As explained in [20], gain K_I is the coefficient of the lowest degree term of Taylor expansion of (2-3). Corner frequency ω_{cs} is a function of diffusion coefficient and is obtained by a limit study to (2-2) at high frequencies.

For an easier initialization of the system and also to make the variable *SOC* appear, the model structure is improved comparing to [20, 27]. Thereby $H(s)$ is split into two sub-functions representing respectively the average concentration $H_{avg}(s)$ (correlates to the steady-state ion concentration from the center to the surface of the particle) and partial gradient of ion concentration on the particle surface $H_{part}(s)$ (associated with the ion concentration gradient under dynamic conditions):

$$H(s) = H_{avg}(s) + H_{part}(s) \quad (2-4)$$

with

$$H_{avg}(s) = \frac{C_{s,avg}}{j_{mean}^{Li}} = \frac{K_1}{s} \quad (2-5)$$

and

$$H_{part}(s) = \frac{\Delta C_s}{j_{mean}^{Li}} = H(s) - H_{avg}(s) = \frac{K_1}{s} \left(\left(1 + \frac{s}{\omega_{cs}} \right)^{0.5} - 1 \right). \quad (2-6)$$

In order to implement the battery model in the battery control unit, a discrete form of $H(s)$ is required. This discrete form is obtained in three stages according to the method proposed by Oustaloup *et al.* [28]:

- approximation of the fractional transfer function $H_{part}(s)$ using the Oustaloup recursive algorithm

$$H_{app1}(s) = \frac{K_1}{s} \left(\left(\frac{1 + \frac{s}{\omega_{cs}}}{1 + \frac{s}{\omega_h}} \right)^{0.5} - 1 \right) \approx \frac{K_1}{s} \left(\prod_{k=1}^N \frac{1 + \frac{s}{\omega_{zk}}}{1 + \frac{s}{\omega_{pk}}} - 1 \right) \quad (2-7)$$

- first order elements expansion of the approximation which can then be easily implemented in state-space environment

$$H_{\text{app}2}(s) = \frac{K_1}{s} \left(\prod_{k=1}^N \frac{(1 + \frac{s}{\omega_{zk}})}{(1 + \frac{s}{\omega_{pk}})} - 1 \right) \approx K_1 \sum_{k=1}^N \frac{A_k}{1 + \frac{s}{\omega_{pk}}} \quad (2-8)$$

- discrete-time approximation of $H_{\text{app}2}(s)$ using forward Euler approach $s \approx \frac{1-z^{-1}}{T_s}$.

By increasing the number of zeros and poles in (2-7) and by using other algorithms [29], higher accuracy can be achieved. Figure 2-5 shows that by choosing $N = 7$, a good fit between the approximated integer-order function and fractional order is obtained on a wide frequency band.

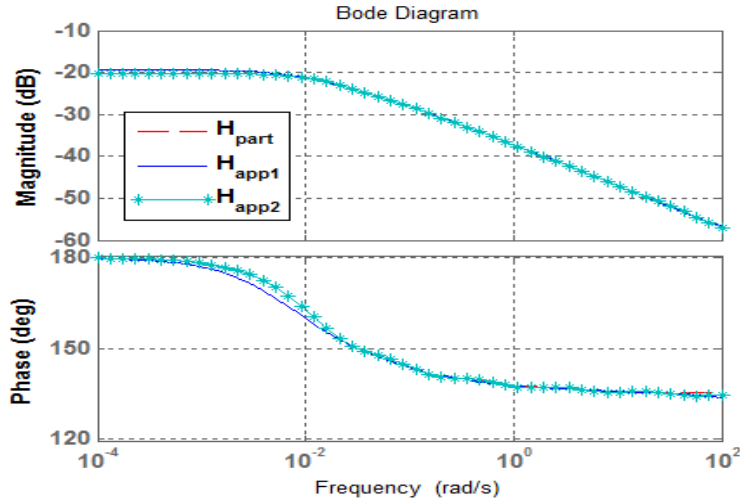


Figure 2-5 Comparison of fractional transfer function and its approximations in a frequency domain compatible with the BMS sampling frequency.

Figure 2-6 shows the fractional transfer function for one electrode defined by (2-3) that has been implemented in *Matlab/Simulink*. The fractional battery model consists of two sub-models, for each electrode. Thus the same structure but with different set of parameters has been used for both anode and cathode to calculate the terminal voltage out of electrode potentials.



Figure 2-6 Block diagram implementation of the electrical fractional model

As shown in Figure 2-6, the electrode potential is composed of two parts, one from open circuit potential under equilibrium conditions and the other from charge transfer kinetics governed by Butler-Volmer equation, characterized by R_{ct} resistance. In order to compute the overpotential caused by charge transfer kinetics denoted by $\eta_{charge\ transfer}$, the following relation is used which is indeed the inverse of Butler-Volmer equation (i is replaced by *charge transfer* in $\eta_{charge\ transfer}$ to distinguish between anode (n) and cathode (p)):

$$\eta_i = \frac{RT}{\alpha_i F} \sinh^{-1} \left(\frac{J_i}{2a_s^i i_{0i}} \right) \quad i \in \{n, p\} \quad (2-9)$$

In this relation, R is the universal gas constant $8.314 \text{ (J.mol}^{-1}.\text{K}^{-1})$, F is the Faraday constant $96485 \text{ s.A.mol}^{-1}$, and T stands for temperature. α_i is charge transfer coefficient, $J_i \text{ (A.m}^{-2})$ denotes the current density, a_s^i is the specific area and $i_{0i} \text{ (A.m}^{-2})$ presents the exchange current density respectively for each of the electrodes.

2.3.1 Model calibration

At this step, the proposed electrode model in Figure 2-6, should be parametrized. The datasheet of the studied cell, Samsung 28 Ah cells contains only some electrical limit values for its safe operation. The relevant data to our study from the datasheets are given below:

Parameter	Value (unit)
Nominal capacity	28 (Ah)
Nominal voltage	3.75 (V)
Charging cut-off voltage	4.3 ± 0.03 (V)
Discharge cut-off voltage	2.75 (V)
Cell weight	758.4 (g)
Cell dimension	Height: 65.00 (mm) Diameter: 8.40 (mm)
Operating temperature	Charge : 0 to 45°C Discharge: -20 to 60°C

Table 2-1 Prismatic Samsung SDI 28 cell specifications from manufacturer

Thus for full characterization of the model, combination of the following methods have been used to acquire the necessary electrochemical data:

- data from *Comsol* simulation
- data from measurement and literature
- parameter fitting.

Some physical parameters are based on the results obtained from a P2D model of Newman [15, 30] developed in *Comsol Multiphysics* at Bosch Research and Technology Center in North America. The rest of electrochemical parameters are acquired from the measurements performed by Institut für Stromrichtertechnik und elektrische Antriebe (*ISEA* – Institute for current converter technology and electrical drives) at the RWTH Aachen University [31].

For example for porosity and particle radius measurement, mercury porosimetry was carried out using two measurement devices with different pressure ranges. The data of the two devices were merged using the *SOLID* software to obtain respective porosity of each electrode and the separator. Consequently using Mayer and Stowe approach particle radius for each electrode is computed [32].

For precise calculation of solid diffusion coefficient, GITT (Galvanostatic Intermittent Titration Technique) method is employed. Anode and cathode coin cells are made and used for this purpose. The test is carried out at room temperature. In a GITT measurement, the cell is excited with a current pulse (here 150 s at $C/20$) from the equilibrium state. By applying the GITT current, an increasing voltage deviation is observed in addition to the pure ohmic voltage drop. This is attributed to the formation of a concentration gradient in the active material. Thereby this feature is used for calculation of diffusion coefficient. [33]

In order to characterize the transport and kinetic properties of the cell, firstly an impedance spectroscopy test was performed on half-cell level to measure the impedance of each electrode. By measuring the impedance in medium frequency range, R_{ct} of each electrode is obtained. Subsequently, by having the values of electrodes charge transfer resistance, exchange current density is computed by fitting the data to Butler-Volmer relation. A list of the resulting data from *Comsol* simulation as well as the mentioned experiments can be found in Table 2-2.

Parameter	Anode	Separator	Cathode
<i>Design specification and geometric data</i>			
Active material	Graphite		NMC
Thickness	46.6 (μm)	18.7 (μm)	43.0 (μm)
Particle radius	6.3 (μm)		2.13 (μm)
Porosity (%)	29.2 %	39.49 %	20.9 %
Specific interfacial area			
<i>Solid and Electrolyte phase concentration</i>			
Maximum solid phase concentration	31390 (mol.m^{-3})		48390 (mol.m^{-3})
Stoichiometry at 0% SOC ⁽¹⁾	0.18365		0.9174
Stoichiometry at 100% SOC ⁽²⁾	0.9152		0.40299
<i>Kinetic and transport properties</i>			
Diffusion coefficient	3.1623×10^{-14} ($\text{m}^2.\text{s}^{-1}$)		1.4125×10^{-15} ($\text{m}^2.\text{s}^{-1}$)
Charge transfer exchange current density	36 (A.m^{-2})		26 (A.m^{-2})
Charge transfer coefficients	0.5	0.26	0.5
Li ⁺ transference number	0.26		0.26
High frequency resistance (Begin of Life)	0.6 ($\text{m}\Omega$)		
Specific heat capacity	0.7 ($\text{J.g}^{-1}.\text{K}^{-1}$)		
Heat transfer coefficient	10 ($\text{W.m}^{-2}.\text{K}^{-1}$)		

Table 2-2 Electrochemical model parameters for Samsung SDI 28 Ah PHEV cells ((1) and (2): the method used to obtain electrode stoichiometries are explained in details in chapter 3)

Another important necessary data concerns the electrode Open Circuit Potential (OCP) and the cell Open Circuit Voltage (OCV) measurements which are discussed in details in chapter 3. Moreover for a cell at its Begin of Life (BOL), half-cell open circuit potential measurement is performed. The resulting OCP curves of Samsung SDI cells are given in **Figure 2-7**.

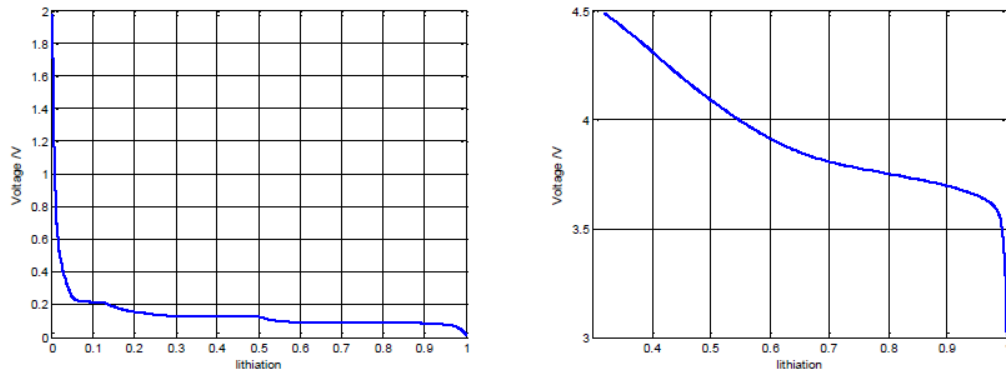


Figure 2-7 OCP curves of Anode (left) and Cathode (right) against the respective lithiation degree

For the rest of parameters, whether for the unmeasurable parameters or in case of observing deviations due to inaccurate measurements, optimization and fitting of the model is conducted. The parameter identification has been performed by nonlinear least squares (curve fitting) method. Therefore, the terminal voltage simulated by the model has been fitted to the measurement under applying dynamic driving cycle current profile. The following relation shows the objective function for the fitting process:

$$SSE = \sum_{k=1}^{n_{\text{meas}}} (U_{\text{meas}} - U_{\text{sim}})^2. \quad (2-10)$$

The optimization function minimizes the sum of squared errors obtained from deviation of simulated voltage from the measured one over the whole measurement data.

2.3.2 Model validation

The fractional model presented in the previous section and the associated calibration method are validated using a real-world driving cycle. Extended Artemis driving cycle used for model validation is designed at *Bosch* which is very similar to well-known Artemis drive cycle [34], but with some adaptations to the cell performance and its application for PHEVs as shown by Figure 2-8. It covers various driving manoeuvres such as driving with rather constant speed at the highways or driving uphill or downhill recuperation in different areas including urban and rural roads as well as motorways. According to the cell operating limits provided by the manufacturer (see **Table 2-1**), some adaptations are taken into account in the design of the driving scheme. For instance short fast charging regimes are also incorporated into the original Artemis driving profile with maxim current of 3 C, applied for approximately 5 minutes as well as relaxation phases (point (I) on current diagram in **Figure 2-8**). Moreover maximum discharging current is applied for 10 seconds (point II on the current diagram in **Figure 2-8**). These modifications to the original Artemis driving cycle permit to capture all different driving dynamics.

Extended Artemis driving cycle is applied to the fractional battery model and the simulated terminal voltage of the model is compared with the measurements on the first diagram in **Figure 2-8**. The second diagram represents the voltage deviation between the measurements and the simulation. There is a good agreement between the simulation and measurement with the average absolute error below 0.1 V and the maximum error of 0.4 V. The peak error takes place at the deepest discharge level where the maximum discharging current at point (II) is applied.

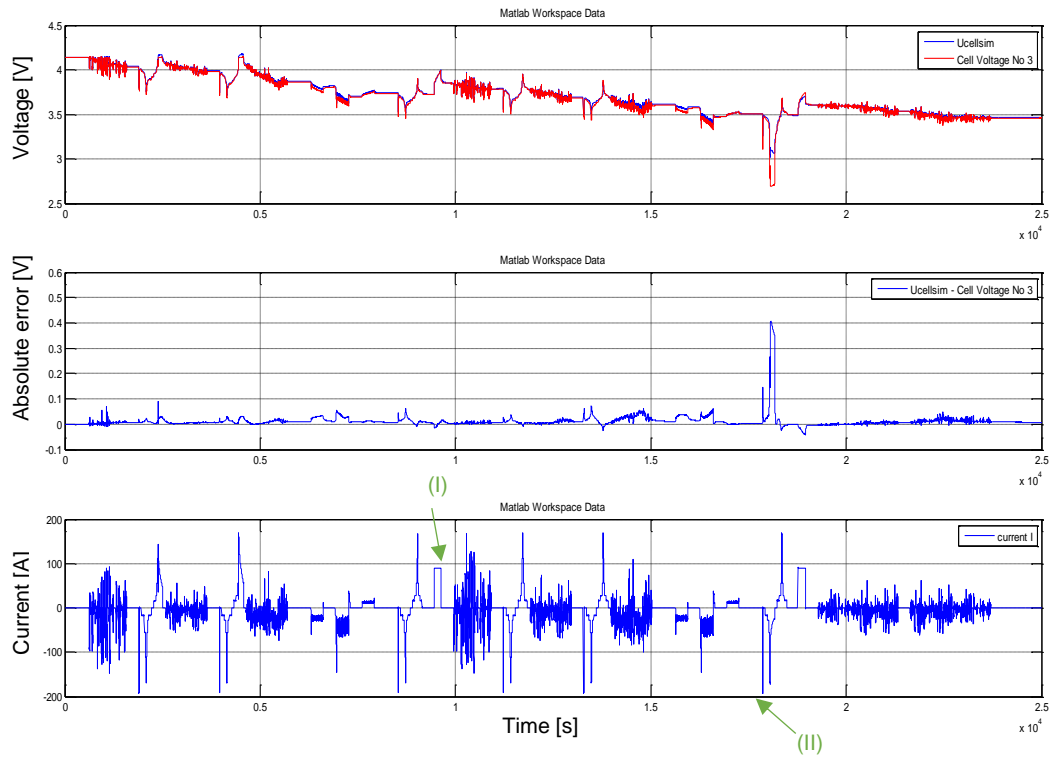


Figure 2-8 Validation results of applying extended Artemis drive cycle to the fractional model

In another validation test the fractional model accuracy is compared to the state-of-the-art battery modelling approach of ECM. The ECM used for validation consists of an order 7 RC (Resistor-Capacitor) circuit and a voltage source representing OCV of the cell, so that the model structure could be compared to the similar fractional model converted to seven first-order elements.

It can be concluded from the diagrams of Figure 2-9, that the simulated voltage by both of the models are in a good accordance, while the voltage estimation error using fractional model has greatly reduced comparing to the ECM model. This analysis proves the superiority of the fractional battery model over ECM in estimation of battery voltage with less computational effort only having two adjustable parameters with physical meaning (K_I : gain correlated to cell capacity and ω_{cs} : corner frequency correlated to diffusion) comparing to ECM with at least 14 resistors and capacitors to be parameterized without any physical background.

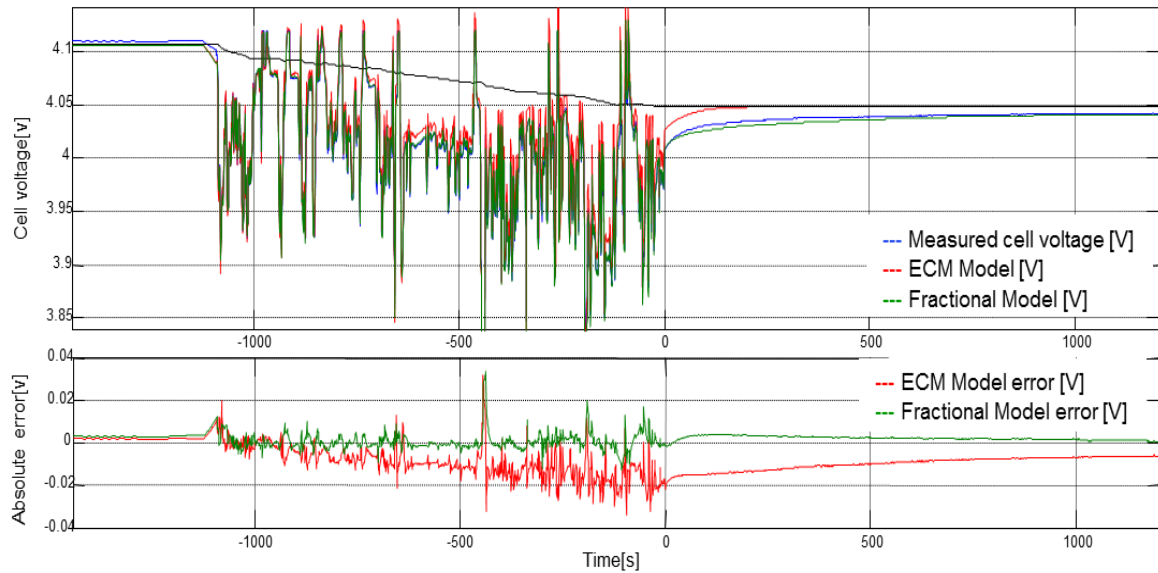


Figure 2-9 Voltage simulation and respective absolute estimation error for fractional battery model and order 7 ECM.

2.4 Conclusion and future work

In this chapter an overview of various battery modelling approaches is presented. Advantages and disadvantages associated with each approach and their application are discussed in section 2.2. The cell used as our case study is a high power Samsung SDI 28 Ah cell for PHEV application. According to the cell specifications and application, a single particle model is chosen for simulation of the battery behaviour in this work. In section 2.3 the concept of incorporating fractional calculus in development of single particle model is introduced. The model is calibrated based on the data acquired from *Comsol*, experiments and manufacturer datasheets. Subsequently the model accuracy is verified by means of a real world driving cycle. It shows promising results and the error lies in an acceptable range for BMS applications. This is why this kind of model is adopted in the next chapters of this manuscript.

For future work, one would expand the concept of fractional battery model for high energy cells with thicker electrodes where the assumptions of a quasi-constant concentration along x -axis on **Figure 2-1** is no more valid. Thus a volume averaged concentration cannot be considered for thick electrodes of EV cell [22]. Also if this model is going to be used for different cell chemistries, more adaptations are required. For example in case of cells with Si-based anodes, influence of hysteresis in the charge and discharge OCV curve needs to be taken into account [35]. A detailed

discussion on the OCV/OCP calculation which has the highest contribution to voltage estimation is demonstrated in chapter 3. The model explained in this chapter was considered at its Begin of Life (BOL). Thus the influence of aging leading to capacity loss will be discussed in chapter 4 in details, where a thermal and aging model are coupled to the fractional model to fully characterize a comprehensive model enabling accurate state detection over the entire life time of the battery.

Chapter 3

AGING CORRECTION OF OCV/OCP MODEL

Summary

3.1 Introduction	27
3.2 Function-based model for electrode potential.....	28
3.3 Concentration profile in the electrodes	31
3.4 OCV formula for the cell at BOL and MOL.....	31
3.4.1 Derivation of OCV formula for aged cells at MOL.....	32
3.5 Balancing: A requirement for optimization problem.....	34
3.6 Aging correction of OCV curve at MOL.....	37
3.7 Conclusion and future work	39

3.1 Introduction

State of Charge (SOC) similar as a fuel gauge for the batteries, is an important indicator for reliable operation of the batteries. Accurate information from the available cell capacity can prolong the lifetime of the cell by taking appropriate measures during the operation. In contrast to a fuel gauge, SOC cannot be measured, but should be estimated. There are different methods for SOC estimation in the literature which can be classified into direct and indirect approaches. The direct measurements include Coulomb counting, which is indeed current integration that is a suitable way of online SOC estimation, but the bottleneck of this approach is its open-loop nature that might generate an accumulated estimation error originating from the error in current measurements. The other direct method which is the focus in this chapter is the direct OCV curve inversion method. In this method, the voltage is measured continuously and the corresponding SOC is obtained whether from a lookup table or from a function. This method is a good candidate for SOC estimation for onboard applications. Other indirect methods can be also employed such as Extended Kalman Filtering (EKF), which is a very reliable method based on an advanced battery model but with high computational effort. [36]

Thus the need for accurate capacity estimation (permissible BMS error for our case study < 3.5%) leads to find an appropriate OCV adaptation strategy, since both are strongly interconnected. This chapter describes the development of a function-based method for describing the Open Circuit Voltage (OCV) of a cell, measured under equilibrium conditions to be used for direct estimation of the available capacity and respectively SOC. The developed method is later on expanded to the aged cells, by taking into account the influence of aging on the variation of respective OCV curves. Alteration of OCV curves by aging is discussed in details in the study by Schmidt *et al.* [37] This influences the performance of OCV-based estimation of SOC and consequently performance and lifetime of the battery.

Aging correction of OCV curves is investigated by Cheng *et al.* [38] where a purely mathematical approach is used to track the changes in the OCV curves caused by aging. Despite the good results and its computational efficiency, this method does not consider the physical phenomena such as Li intercalation mechanism. Physics-based methods facilitate analysis and interpretation of root-causes for OCV curve variation and consequently more accurate SOC and SOH estimation algorithms. Some works have been focused on this topic such as the study by

Honkura *et al.* [39]. In this work, they have employed differential voltage analysis method to reproduce the half-cell OCP curves and the full cell OCV curves after degradation. In another paper by Dubarry *et al.* [40], an incremental capacity analysis is applied to identify various contributions to capacity loss, whereas the open circuit voltage measurements is used to trace the state of charge as the cell degrades in order to accurately correlate the capacity degradation with SOC. The disadvantage of the approaches being introduced in these papers is high computational effort required to model the OCV curves by large number of parameters. Therefore the aim of this study is to explore a strategy to model the OCV curves by a physics-based model involving reduced number of parameters for BMS application. The solution later on discussed is using a polynomial description of the two electrodes Open Circuit Potential (OCP) and analysis of the impact of aging on this description. The analysis is based on the following hypothesis:

Hypothesis (I): It is supposed that the two electrodes OCP are invariant with age, and that only the extreme values of stoichiometry change.

This hypothesis is derived from Redlich-Kister equation comprehensively discussed in [41], that is the relation used for describing the OCP of electrodes as a function of ion concentration. Under constant temperatures the coefficients of Redlich-Kister equation (relation (3-5) explained in next section) remain constant and they are regarded as intrinsic characteristics of the electrodes.

3.2 Function-based model for electrode potential

The electrode stoichiometry is defined as the ratio of inserted lithium quantities ($Q_{i,t}$) over the theoretical maximum quantity of Li ions that can be inserted ($Q_{i,max}$):

$$x_i(t) = \frac{Q_i(t)}{Q_{i,max}(t)} \quad i \in \{n, p\} \quad (3-1)$$

with:

$$Q_{i,max} = \epsilon_{s,i} \delta_i A_i c_{s,i,max}. \quad (3-2)$$

where $\epsilon_{s,i}$ denotes the electrode porosity, $c_{s,i,max}$ is the maximum lithium concentration, A represents the electrode surface and δ_i is the electrode thickness.

Modified Nernst equation is used to describe the OCP of positive (p) and negative (n) electrodes [41]:

$$U_i(x_i, T) = V_{Nernst}(x_i, T) + V_{INT}(x_i) \quad i \in \{n, p\} \quad (3-3)$$

with:

$$V_{Nernst}(x_i, T) = E_i^0 + \frac{RT}{F} \ln\left(\frac{1-x_i}{x_i}\right), \quad (3-4)$$

Based on the definition in [42], V_{INT} is the term added to the Nernst equation, derived from Redlich-Kister relation that takes into account the non-ideal interaction of ions in the cell and it is defined by:

$$V_{INT}(x_i) = \sum_{k=0}^{K_i} A_{i,k} \left[(2x_i - 1)^k + 1 - \frac{2x_i k (1-x_i)}{(2x_i - 1)^{(1-k)}} \right]. \quad (3-5)$$

At this step, relation (3-4) is simplified to a polynomial function (relation (3-8)). Using the following relation:

$$\ln \frac{(1-x_i)}{x_i} = \ln(1-x_i) - \ln x_i = \ln(1-x_i) - \ln(1-(1+x_i)), \quad (3-6)$$

an expansion of $\ln\left(\frac{1-x_i}{x_i}\right)$ on interval of [0,1] is thus given by:

$$\ln\left(\frac{1-x_i}{x_i}\right) = -\sum_{k=0}^{\infty} \frac{x_i^{k+1}}{k+1} - \sum_{k=0}^{\infty} (-1)^{k+1} \frac{x_{i-1}^{k+1}}{k+1}. \quad (3-7)$$

Thus relation (3-4) can be approximated by:

$$V_{Nernst}(x_i, T) \simeq E_i^0 + \frac{RT}{F} - \sum_{k=0}^N \frac{1}{k+1} [(-1)^{k+1}(x_i - 1)^{k+1} - x_i^{k+1}] = \tilde{V}_{Nernst}. \quad (3-8)$$

Assuming a large value for N (the polynomial degree) in relation (3-8), a good approximation can be achieved so that the difference between V_{Nernst} and \tilde{V}_{Nernst} is minimized. Using \tilde{V}_{Nernst} , and by expanding V_{INT} , the following polynomial relation for cell's OCP is derived:

$$U_i(x_i, T) = E_i^0 + \sum_{k=1}^{K_i} C_{i,k}(x_i)^k \quad i \in \{n, p\}. \quad (3-9)$$

Half-cell (OCP) measurements are performed using *ELcell* setup shown in Figure 3-1, which facilitates the potential measurements with respect to a reference electrode. For anode potential measurement, CC-charging with C/50 until reaching 25 mV is used and for cathode, CC-discharging with C/50 until reaching voltage of 1.2 V.



Figure 3-1 ELcell setup for potential measurement (described in - ELcell setup)

Then the potential measurements are fitted to relation (3-9), with $K_i = 20$. As shown in Figure 3-2, a good accordance (absolute error (ΔOCP) less than 5 mV) between measurements and the model is achieved. Relation (3-9) for OCP modelling is thus validated.

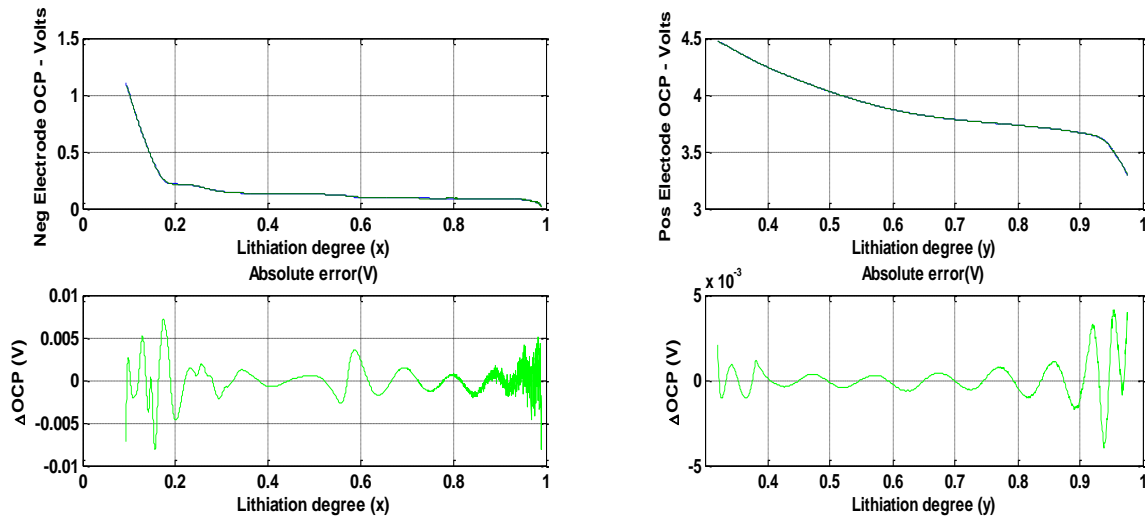


Figure 3-2 OCP fitting at BOL (for the negative electrode (left) and the positive electrode (right))

3.3 Concentration profile in the electrodes

For generalizing the developed function to the cell level, the cell is modelled by two connected tanks as shown in **Figure 3-3** and as proposed in [43]. For this purpose the following parameters are defined:

- $Q_{i,max}$: the maximum theoretical capacity of electrode
- Q_i : the actual capacity at time t and $i\%$ ($0 < i < 100$) SOC
- $Q_{i,0}$ and $Q_{i,100}$: the capacity at 0% (discharge capacity) and 100% SOC

Based on the above definitions we get the following relations:

$$\text{Cell full capacity} \quad Q_{cell} = Q_{n,100} - Q_{n,0} = Q_{p,0} - Q_{p,100} \quad (3-10)$$

$$\text{Available capacity at } i\% \text{ SOC} \quad Q_{av} = Q_n - Q_{n,0} = Q_p - Q_p \quad (3-11)$$

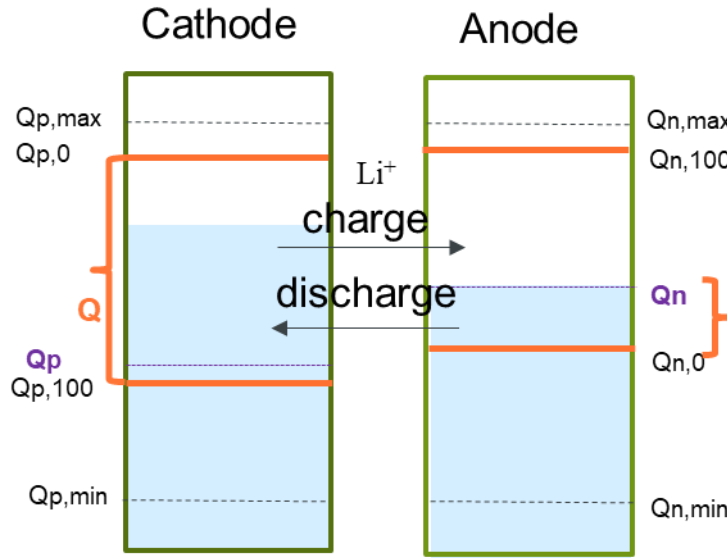


Figure 3-3 Model of cell with two connected tanks (similar concept proposed in [44])

3.4 OCV formula for the cell at Begin Of Life (BOL) and Middle Of Life (MOL)

According to the defined parameters in Figure 3-3, the SOC and the electrode stoichiometry are defined by:

$$SOC = \frac{Q_i - Q_{i,0}}{Q_{i,100} - Q_{i,0}} = \frac{Q_{n,100} - \int Idt - Q_{n,0}}{Q_{n,100} - Q_{n,0}} = \frac{Q_{p,100} + \int Idt - Q_{p,0}}{Q_{p,100} - Q_{p,0}} = 1 \mp \frac{\int Idt}{Q_{i,100} - Q_{i,0}} \quad (3-12)$$

$$x_i = \frac{Q_i}{Q_{i,max}} = \frac{Q_{i,100} \mp \int Idt}{\alpha_i (Q_{i,100} - Q_{i,0})} = \frac{Q_{i,100} \mp \int Idt - Q_{i,0} + Q_{i,0}}{\alpha_i (Q_{i,100} - Q_{i,0})} \quad i \in \{n, p\}. \quad (3-13)$$

If it is supposed that $Q_{i,max}$ is written as:

$$Q_{i,max} = \alpha_i (Q_{i,100} - Q_{i,0}) \quad (3-14)$$

where parameter α_i is a real number, and introducing parameter $\beta_i = \frac{Q_{i,0}}{\alpha_i(Q_{i,0}-Q_0)}$ (3-15), then:

$$x_i = \frac{Q_{i,100} \mp \int Idt - Q_{i,0}}{\alpha_i (Q_{i,100} - Q_{i,0})} + \frac{Q_{i,0}}{\alpha_i (Q_{i,100} - Q_{i,0})} = \frac{SOC}{\alpha_i} + \beta_i \quad i \in \{n, p\}. \quad (3-16)$$

At this point, using relation (3-16), the OCV formula for the cell can be calculated:

$$U_p = E_p^0 + \sum C_{p,k} x_p^k = E_p^0 + \sum C_{p,k} \left(\frac{SOC}{\alpha_p} + \beta_p \right)^k \quad (3-17)$$

$$U_n = E_n^0 + \sum C_{n,k} x_n^k = E_n^0 + \sum C_{n,k} \left(\frac{SOC}{\alpha_n} + \beta_n \right)^k \quad (3-18)$$

$$OCV = U_p - U_n. \quad (3-19)$$

Parameters $Q_{i,0}$ and $Q_{i,100}$ depend on aging, thus parameters α_i and β_i also depend on aging. Therefore, in the case of having the half-cell measurements, OCV of the cell after aging (at MOL) can be taken into account by optimization of 4 parameters: $\alpha_p, \beta_p, \alpha_n, \beta_n$.

3.4.1 Derivation of OCV formula for aged cells at MOL

It is supposed that aging only impacts the value of $Q_{i,100}$ and $Q_{i,0}$. As a consequence the value of Q_{av} is affected. However, SOC=100 % is always defined for $U_{100} = 4.2 V$ whatever the aging is. Thus parameters $\Delta Q_{i,100}, \Delta Q_{i,0}, \delta Q_i$ are introduced to take into account the aging phenomena such that:

$$Q_{i,100}^{aged} = Q_{i,100}^{new} + \Delta Q_{i,100} \quad (3-20)$$

$$Q_{i,0}^{aged} = Q_{i,0}^{new} + \Delta Q_{i,0} \quad (3-21)$$

$$Q_{i,max}^{aged} = Q_{i,max}^{new} \delta Q_i \quad (3-22)$$

It means that, by aging both of the electrode capacities at SOC of 0% and 100% and also the cell full capacity changes. At BOL the following relations hold for cathode and anode respectively:

$$\begin{aligned} U_p &= E_0^p + \sum C_{p,k} \left(Q_{p,100}^{new} + K \int Idt \right)^k \\ U_n &= E_n^0 + \sum C_{n,k} \left(Q_{n,100}^{new} - K \int Idt \right)^k. \end{aligned} \quad (3-23)$$

After expansion, it thus can be demonstrated that:

$$\begin{aligned} U_p &= \bar{E}_p^0 + \sum \bar{C}_{p,k} \left(\int Idt \right)^k \\ U_n &= \bar{E}_n^0 + \sum \bar{C}_{n,k} \left(\int Idt \right)^k. \end{aligned} \quad (3-24)$$

By replacing relations (3-20), (3-21) and, (3-22) into equation (3-9) for an electrode at BOL, the formula for the OCP at MOL is derived:

$$U_i^{aged} = E_i^0 + \sum_k C_{i,k} (x_i^{aged})^k \quad (3-25)$$

By using relation (3-1), relation (3-25) becomes:

$$U_i^{aged} = E_i^0 + \sum_k C_{i,k} \left(\frac{Q_i^{aged}}{Q_{i,max}^{aged k}} \right) \quad (3-26)$$

and based on relation (3-13):

$$U_i^{aged} = E_i^0 + \sum_k C_{i,k} \left(\frac{Q_{i,100}^{new} + \Delta Q_i \pm \int Idt}{\delta Q_i Q_{i,max}^{new}} \right)^k. \quad (3-27)$$

From (3-27) the following relations are obtained for the negative electrode:

$$\begin{aligned} U_n^{aged} &= E_n^0 + \sum C_{n,k} \left(\frac{\frac{Q_{n,100}^{new}}{\delta Q_n} + \frac{\Delta Q_n}{\delta Q_n} - \frac{1}{\delta Q_n} \int I dt}{Q_{n,max}^{new}} \right) \\ &= E_n^0 + \sum_k C_{n,k} \left(\frac{Q_{n,100}^{new} - \left(Q_{n,100}^{new} - \frac{Q_{n,100}^{new}}{\delta Q_n} - \frac{\Delta Q_n}{\delta Q_n} + \frac{1}{\delta Q_n} \int Idt \right)}{Q_{n,max}^{new}} \right). \end{aligned} \quad (3-28)$$

According to relations (3-23) and (3-24) for the aged anode potential:

$$U_n^{aged} = \bar{E}_n^0 + \sum_k \bar{C}_{n,k} \left(\underbrace{Q_{n,100}^{new} - \frac{Q_{n,100}^{new}}{\delta Q_n} - \frac{\Delta Q_n}{\delta Q_n}}_{a_n} - \underbrace{\frac{1}{\delta Q_n} \int I dt}_{b_n} \right)^k \quad (3-29)$$

and by analogy, for the positive electrode:

$$U_p^{aged} = \bar{E}_p^0 + \sum_k \bar{C}_{p,k} \left(\frac{(Q_{p,100}^{new} + (-Q_{p,100}^{new} + \frac{Q_{p,100}^{new}}{\delta Q_p} + \frac{\Delta Q_p}{\delta Q_p} + \frac{1}{\delta Q_p} \int I dt))}{Q_{p,max}^{new}} \right)^k \quad (3-30)$$

and again referring to relations (3-23) and (3-24):

$$U_p^{aged} = \bar{E}_p^0 + \sum_k \bar{C}_{p,k} \left(\underbrace{-Q_{p,100}^{new} + \frac{Q_{p,100}^{new}}{\delta Q_p} + \frac{\Delta Q_p}{\delta Q_p}}_{a_p} - \underbrace{\frac{1}{\delta Q_p} \int I dt}_{b_p} \right)^k. \quad (3-31)$$

Therefore to summarize, the following steps are required to modify the OCV curve of an aged cell:

1. Fitting the OCP measurements at BOL with the polynomial function of relation (3-24), and polynomial coefficients \bar{E}_i^0 and $\bar{C}_{i,k}$;
2. Optimizing the a_i and b_i parameters so that OCV at MOL can be fitted to the following relations:

$$OCV = U_p - U_n = \bar{E}_p^0 + \sum_k \bar{C}_{p,k} \left(a_p + b_p \int I dt \right)^k - \left(\bar{E}_n^0 + \sum_k \bar{C}_{n,k} \left(a_n + b_n \int I dt \right)^k \right). \quad (3-32)$$

The optimization problem is solved by minimizing the deviation between the model and the measurements. The objective function is:

$$SSE = \sum_k (OCV_{model,k} - OCV_{meas,k})^2. \quad (3-33)$$

3.5 Balancing: a requirement for optimization problem

As it can be seen in relation (3-32), anode OCP is subtracted from cathode OCP in order to calculate OCV. The problem is that the two half-cell potentials need to be adjusted before doing the subtraction. For this purpose, an algorithm (**Figure 3-4**) is used to determine the extreme electrode potential values at 0 and 100% SOC, and then the other points will be automatically

adjusted. After cell balancing, the potentials can be subtracted and the overall OCV curve can be reconstructed from the half-cell measurements.

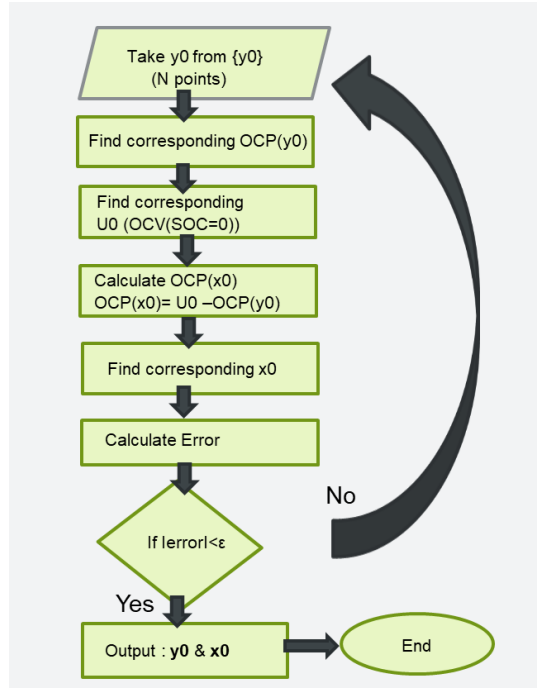


Figure 3-4 Flowchart showing the cell balancing algorithm

For a given y_0 a good x_0 can be deduced because at $SOC = 0$, the OCV value is:

$$SOC = 0 \rightarrow OCV_{min} = U_0. \quad (3-34)$$

As $OCP_p(y_0)$ is known, therefore:

$$P_n(x_0) = OCP_p(y_0) - U_0. \quad (3-35)$$

Thus x_0 is the value of x such as the previous relation holds. The same thing can be done at $SOC = 100\%$.

For a given y_{100} the corresponding x_{100} can be deduced so that the OCV at $SOC = 100\%$ is U_{100} . This can be done using the fitted polynomials so that:

$$OCP_n(x_{100}) = OCP_p(y_{100}) - U_{100}. \quad (3-36)$$

Then the question is to find the best values of y_0 and y_{100} to minimize the error between $OCV(SOC)$ and $OCP_p(SOC) - OCP_n(SOC)$.

Since the fitted polynomials for OCP_p and OCP_n are respectively function of y and x , thus the following relation in the interval of $y \in [y_0, y_{100}]$ and $x \in [x_0, x_{100}]$ can be used:

$$y = (y_{100} - y_0)SOC + y_0, \quad (3-37)$$

$$x = (x_{100} - x_0)SOC + x_0. \quad (3-38)$$

Using the explained approach, the stoichiometries of anode and cathode are calculated based on the error surface minima represented by **Figure 3-5** and defined by the following relation:

$$Min(Error) = Min(OCV(SOC) - (OCP_p(SOC) - OCP_n(SOC))) \quad (3-39)$$

The following results are obtained:

$$x_0 = 0.18365, \quad x_{100} = 0.9152,$$

$$y_0 = 0.9174, \quad y_{100} = 0.40299.$$

These values are very close to those proposed in [17].

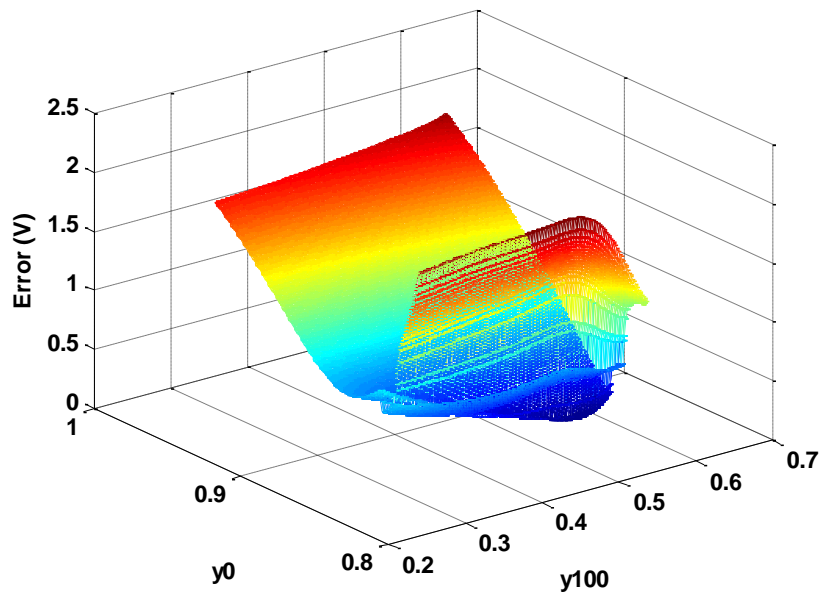


Figure 3-5: balancing error surface

Using the obtained stoichiometry values, the anode and cathode potentials are balanced and the respective OCV can be constructed by subtraction of half-cell potentials. Comparison between the reconstructed OCV and the measured OCV is shown in **Figure 3-6**.

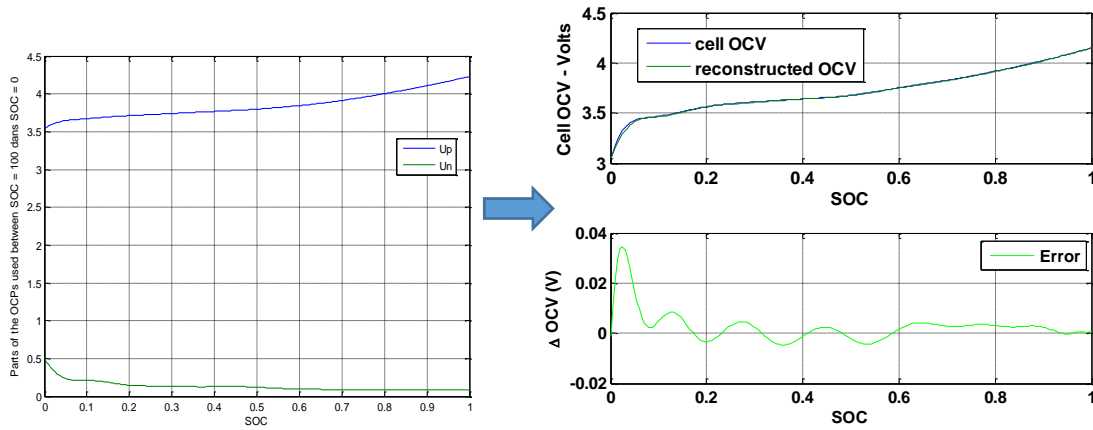


Figure 3-6: OCP balancing and reconstructed OCV

3.6 Aging correction of OCV curve at BOL

Based on the approach described in section 3.4 , Figure 3-7 represents the balanced anode OCP fitting at BOL using polynomial of degree 20 (relation (3-24)).

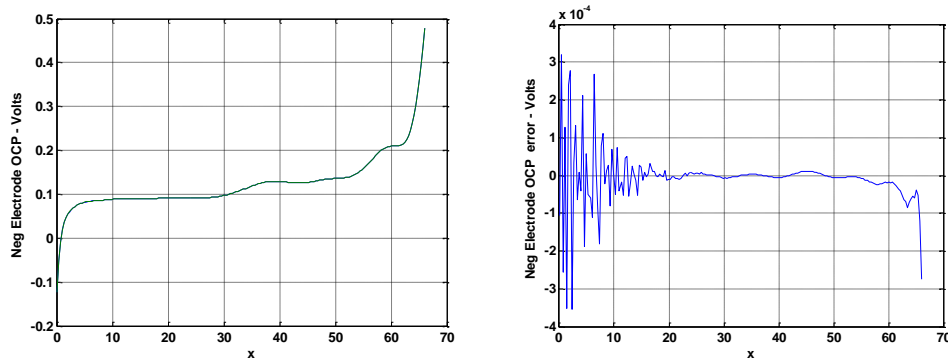


Figure 3-7: Balanced anode OCP fitting and the respective error

Equivalently, balanced cathode OCP fitting at BOL using polynomial of degree 20 (relation (3-24)) is represented by **Figure 3-8**.

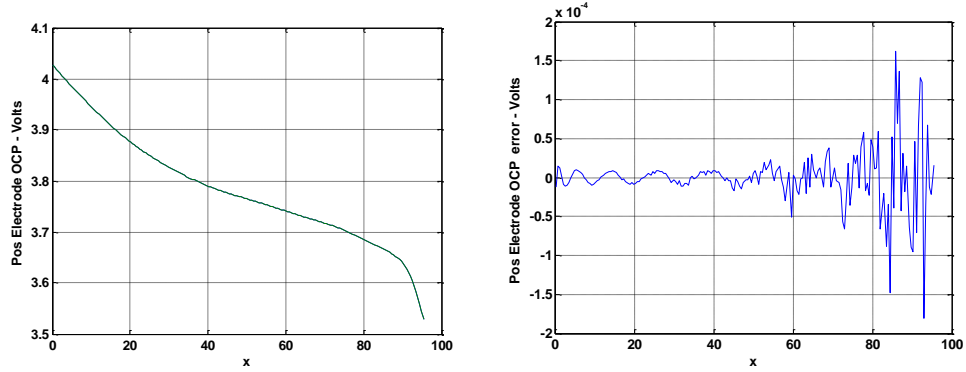


Figure 3-8: Balanced cathode OCP fitting and the respective error

In **Figure 3-9**, the difference between the half-cell electrode potentials and the reconstructed OCV for the new and aged cell can be observed.

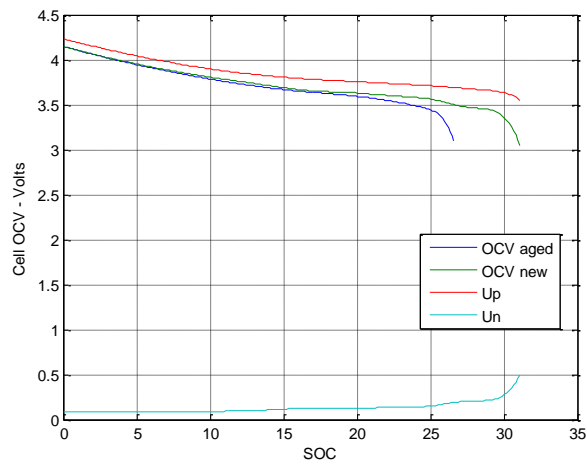


Figure 3-9 Comparison of balanced OCPs and reconstructed OCV

At this step, parameters a_n, b_n, a_p and b_p for correction of OCV curve at MOL are optimized as based on the objective function of relation (3-33). The difference between the model and the real OCV at MOL is represented by **Figure 3-10**. The difference between the two curves is also shown.

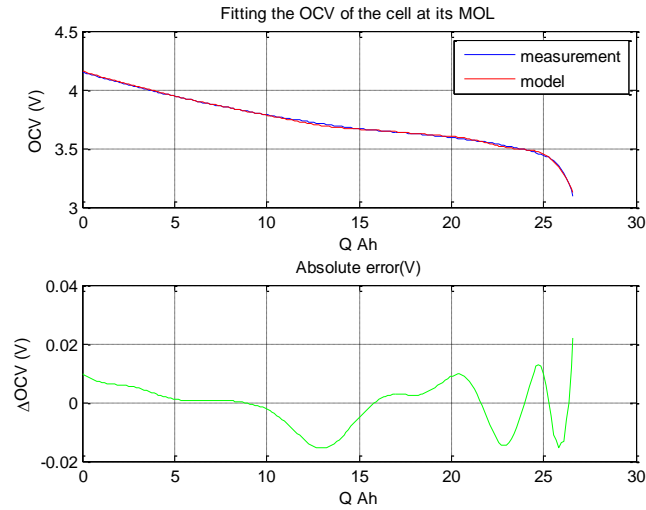


Figure 3-10 Aged OCV correction (comparison of model and measurement (top) and its respective error (bottom))

3.7 Conclusion and future work

A polynomial function was used to represent the behavior of electrode potentials and it was extended to the cell level to simulate the OCV curves at BOL. After introducing aging parameters, the method was modified so that including the aged cell OCV curves. The parameters were optimized in order to minimize the difference between the model and the measurements.

As a requirement for the optimization problem, the cell OCP was adjusted using an algorithm described in section 3.5 .

It can be noticed from **Figure 3-10**, that after aging, the proposed method permits to adjust the cell OCV with an error close to 20 mV. Such an error is too large for implementation in a BMS and might have two origins:

- The balancing method proposed in section 3.5 , permits the cell OCV fitting within an error close to 20 mV. Such an error has an impact certainly on the accuracy of the OCV adjustment method proposed.
- *Hypothesis (I)* in section 3.1 is perhaps not met and electrode heterogeneities have an impact on the shape of the electrode OCPs.

In the future work the effect of heterogeneous aging on the same electrode needs to be taken into account to improve the accuracy of the model. This reveals the interest to well understand the aging mechanisms in lithium ion cells, which is the focus of the next chapter.

Chapter 4

AGING MODELLING

Summary

4.1 Review on aging mechanisms and aging modelling techniques	42
4.1.1 Classification of aging mechanisms based on location in the cell	43
4.1.1.1 Aging on the negative electrode	43
4.1.1.2 Aging on the positive electrode	44
4.1.2 Classification of aging mechanisms based on time	45
4.1.2.1 Calendar aging	45
4.1.2.2 Cyclic aging	47
4.2 Implementation of Electro-thermal aging model.....	49
4.2.1 Thermal model	49
4.2.2 Aging Model	50
4.2.2.1 SEI Growth Model	52
4.2.2.2 Decoupling of calendar and cycling aging	57
4.3 Validation of the coupled Electro-thermal aging model	59
4.3.1 Validation of the Electro-thermal Model	59
4.3.2 Validation of Aging Model	60
4.4 Conclusion and future work	64

Aging of batteries can be investigated with respect to the application, whether short-term e.g. under fast charging or long-term e.g. cycling of battery until End of Life (EOL). In this study, the developed model is designed for generation of fast charging algorithms. Thus the degradation is considered to be caused mainly by formation of solid electrolyte interphase (SEI) layer growth [45] on the anode which is mostly seen by short to middle-term usage of battery during fast charging. In case of long-term cycling, further phenomena such as loss of active material may happen that can be modelled by other techniques explained in section 4.1.2.2. Since temperature is identified as a key factor to provoke battery degradation, a thermal model is designed and coupled to the aging model to take into account its influence in section 4.2.1 .

4.1 Review on aging mechanisms and aging modelling techniques

Battery aging is a complicated process where various environmental conditions and utilization scenarios interact with each other to provoke different degradation effects. Driving cycle and the road profile has a great impact on aging of the battery packs. Driving with rather a constant speed in residential areas has less destructive impact on the vehicle battery than driving with frequent acceleration on highways which requires more available peak power. Besides that, environmental conditions especially the ambient temperature greatly affects battery longevity. Various exothermic reactions are likely to happen in a battery during operation (whether charge or discharge mode) and high temperature is of course a triggering factor for such reactions leading to degradation. These kind of factors depending on external conditions and their interaction are really difficult to be predicted, and quantified in the context of aging estimation.

In most of the studies on battery aging, capacity fade and internal resistance increase of the cell are identified as aging indicators. Capacity fade results in reduction of the available driving range of the electrified vehicles, while resistance increase mainly leads to fading of available power. There is no clear correlation between capacity fade and resistance increase. Depending on the type of cell either capacity fade or resistance increase can be used for quantification of aging. Usually for EV cells with large sizing, there is less concern regarding the available range. But for high power PHEV cells with smaller size, reduction in the available range is a problem to be addressed [46]. Thus capacity fade is the metric used to quantify the aging of PHEV cell under investigation in this work.

A great number of chemical and mechanical mechanisms are associated with aging of Lithium-ion batteries depending on the cell chemistry. Comprehensive review of these mechanisms can be found in a study by Barré *et al.* [47] and Vetter *et. al* [48]. In general, operating and storing the cells at extreme environmental conditions such as very high or very low temperatures, very large or very low initial SOC levels are very destructive. Moreover, charging with large SOC swings, or at elevated voltage exposure, or by applying large charging current amplitudes adversely influence the lifespan of the batteries.

Various aging mechanisms can be categorized whether based on the location that they happen or based on the time that it takes. These classifications are explained in next section. Both cases involve one of the following adverse consequences on the battery performance [47]:

- 1- primary capacity fade due to loss of mobile cyclable Li ions (caused by side reactions and formation of SEI layer);
- 2- secondary capacity fade due to loss of active material (caused by material dissolution, particle isolation, structural deformation, ...);
- 3- resistance increase (caused by film formation and electrode delamination inducing loss of electrical contact and impedance rise).

4.1.1 Classification of aging mechanisms based on location in the cell

Due to a different chemical composition of anode and cathode, the aging mechanisms happening on each side differs from the other. Aging of electrolyte is mainly observed at the interphase between each electrode and the electrolyte and is considered with other aging phenomena at the electrodes [48].

4.1.1.1 Aging on the negative electrode

The operating voltage of the lithium-ion battery is outside of the electrochemical stability window of electrolyte. Hence by reduction of electrolyte at the interphase of the anode a protective film referred as Solid Electrolyte Interphase (SEI) is formed. Growth of the SEI layer mainly happens during the first charging cycles and it slows down after a while. SEI acts as a protective layer towards corrosion of electrode and guarantees safety. However, gradual growth of the layer leads to loss of mobile Li ions and thereby capacity loss. Moreover rising thickness of the layer increases the cell internal resistance leading to power fade. *Figure 4-1* summarizes the major aging phenomena at the anode and its interphase with electrolyte. Another phenomenon depicted in the figure is graphite exfoliation. It is caused by diffusion of solvent through SEI layer and its insertion

to the layered structure of graphite. Gas formation and expansion of anode are the potential consequences of this mechanism. Li-plating is the dominating mechanisms at low temperature. It is a result of Li precipitation on the surface of anode that leads to dendrite formation and finally short circuit and safety issues [49].

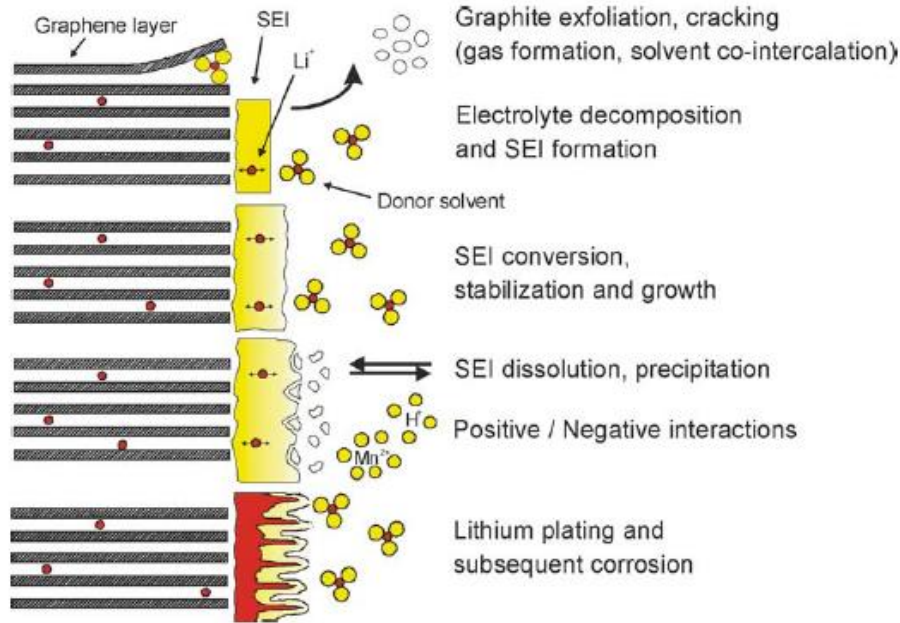


Figure 4-1 Aging mechanisms on anode and its interphase with electrolyte [48]

4.1.1.2 Aging on the positive electrode

Contribution of cathode in overall aging of Li-ion batteries is negligible comparing to anode. Studies have proved insignificant modification of cathode structure at different levels of cycling [50]. The cathode of cell under investigation is principally composed of $\text{LiCo}_{1/3}\text{Ni}_{1/3}\text{Mn}_{1/3}\text{O}_2$ commonly referred as NMC. The main aging mechanisms associated with NMC material is metal dissolution observed at high temperatures that induces capacity fade of cathode. Besides that, due to exposure of cathode to high voltage, structural deformation is another common aging phenomenon discovered on the cathode side. This phenomenon blocks the Li diffusion pathways, leading to a decrease of the cathode rate capability [51]. A summary of the main degradation mechanisms are given in **Figure 4-2**. It includes further phenomena such as oxidation of electrolyte at the surface of cathode resulting in film formation, binder decomposition triggering loss of contact with the electrode surface and finally corrosion of current collector.

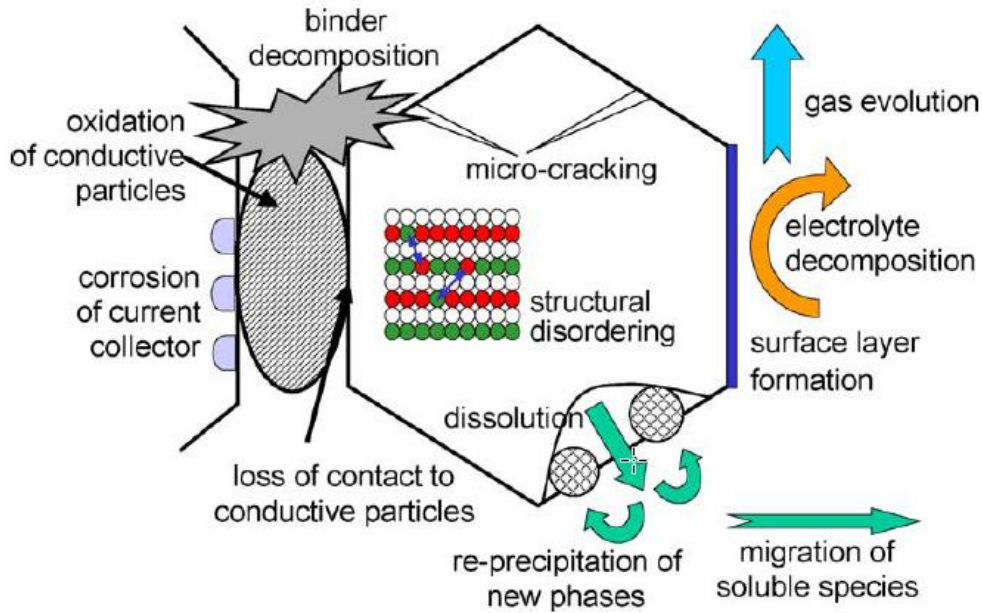


Figure 4-2 Aging mechanisms on cathode and its interphase with electrolyte [4]

4.1.2 Classification of aging mechanisms based on time

Another classification of aging mechanisms can be done based on the time it takes to happen. According to time criterion, aging happening by storage on a large time-scale is referred as calendar aging while aging caused by usage of the cell (charge or discharge) in a short to medium time-scale is called cycling aging.

4.1.2.1 Calendar aging

Calendar aging is the degradation caused by self-discharge current during storage of the batteries (i.e. zero input current). This type of aging is highly dependent on the storage conditions. An experiment on SDI cells was performed to evaluate the impact of storage conditions on calendar aging. For this experiment, the cell was stored at different temperatures and initial SOC levels and the actual capacity was measured in 10 different time intervals up to 140 days. The test specifications are listed in *Table 4-1*.

Experiment No.	Test Conditions	
	Temperature [°C]	SOC [%]
#1	25 °C	100%
#2		95%
#3		30%
#4		15%
#5		10%
#6	35 °C	100%
#7		95%
#8		30%
#9		15%
#10		10%
#11	50 °C	100%
#12		95%
#13		30%
#14		15%
#15		10%
#16	60 °C	100%
#17		95%
#18		30%
#19		15%
#20		10%

Table 4-1 Calendar life test specifications

Each 3D diagram in **Figure 4-3** presents the variation of the actual capacity against the storage time and initial SOC at a certain temperature, including 25, 35, 50, and 60 °C. It can be observed on both diagrams that, storing the cells at higher temperature and high SOC has led to pronounced reduction of cell capacity.

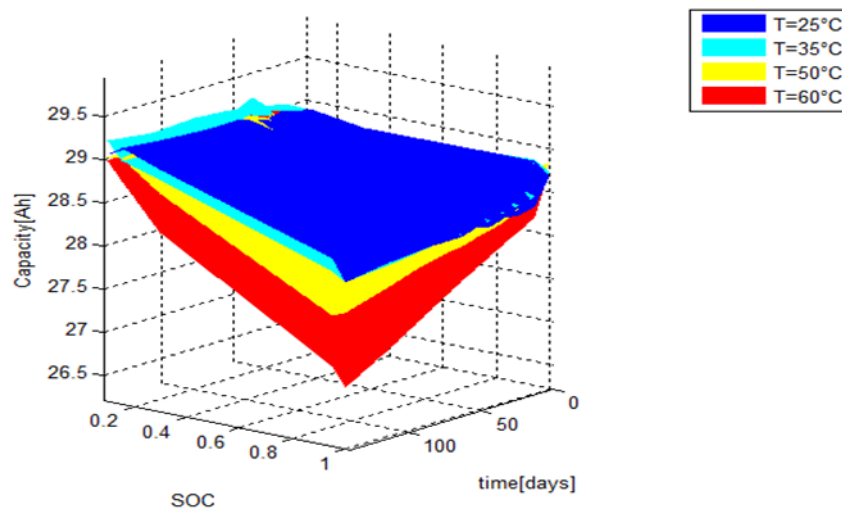


Figure 4-3 Calendar aging measurement results for SDI prismatic cells

The reason lies in the disequilibrium condition provided by high initial SOC; that means a large concentration gradient between anode and electrolyte. Also higher temperature is a triggering factor for parasitic reactions such as corrosion [47].

4.1.2.2 Cyclic aging

Successive charge and discharge of batteries during operation provoke cycling aging. Ecker *et al.* [52] has done a thorough investigation on calendar and cycling aging of Graphite/NMC based batteries. It has been proven that cycling aging is substantially larger comparing to calendar aging. Among various factors associated with cyclic aging, most important severity factors are: cycling temperature, cycle depth (ΔSOC), charging/discharging C-rate and voltage [47]. The impact of these factors on aging of the considered cells was evaluated by performing some experiments, based on the test specifications presented in *Table 4-2*.

No.	Content	Test Conditions				
		T / °C	SOC / %	ΔSOC / %	Charge current	Discharge Current
#1	Cycle depth impact	35 °C	90% ↔ 30%	60%	1C	2C
#2			90% ↔ 20%	70%		
#3			90% ↔ 10%	80%		
#4			90% ↔ 5%	85%		
#5			100% ↔ 0%	100%		
#6	Temperature impact	0 °C	95% ↔ 15%	80%	1C	2C
#7		10 °C				
#9		25 °C				
#10		45 °C				
#11		60 °C				
#12	Charge rate impact	35 °C	95% ↔ 15%	80%	0.33C	2C
#13					0.5C	2C
#14					1C	2C
#15					2C	2C
#16					3C	2C
#17				4C	2C	

Table 4-2 Cyclic life test specifications

The results are depicted on three diagrams in *Figure 4-4*, each presenting the impact of a certain specific aging factor on value of cell aging rate (mAh.kAh^{-1}), calculated by division of capacity fade (mAh) by total charge throughput (kAh). The cell behavior in these experiments confirms the influence of the mentioned factors. Aging rate has greatly increased by charging the cell with larger SOC swing (*Figure 4-4* (a)) and larger C-rate (*Figure 4-4* (c)). In *Figure 4-4* (b), at extremely low and extremely large temperature, capacity fade dramatically rises, and the minimum aging is observed for moderate operating temperature of 25 °C.

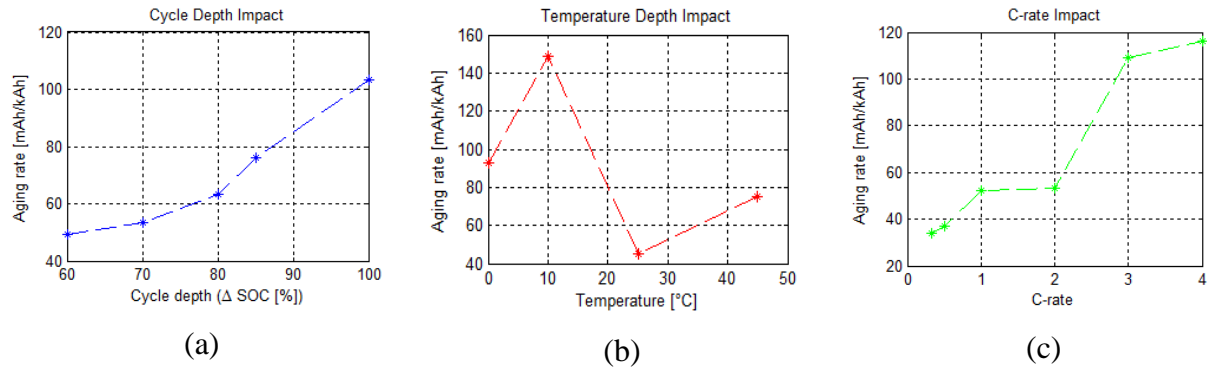


Figure 4-4 cyclic test results - aging as a function of (a): cycle depth, (b): temperature, and (c): C-rate

For a long-term cycling study until End of Life (EOL) of the cell or by cycling under extremely large charge and discharge rates, the graphite structure undergoes a deformation and cracks due to the stress exposed by intense intercalation/de-intercalation of Li-ions. Formation of cracks creates new surface area during cycling. These fresh surfaces act as catalysis for SEI formation. At high charge or discharge rates, the diffusion induced fracture and crack propagation results in a higher side reactions rates. A schematic presentation of the electrochemical and mechanical degradation model in this study is shown in Figure 4-5 [53]. In order to consider the effect of high mechanical stresses inducing fractures in the electrode structure, it is necessary to couple the chemical aging mechanisms to the mechanical aging effects by implementing a coupled electrochemical-mechanical-thermal model. Loss of active material due to mechanical stress can be modelled by semi-empirical relations such as the method described in [54].

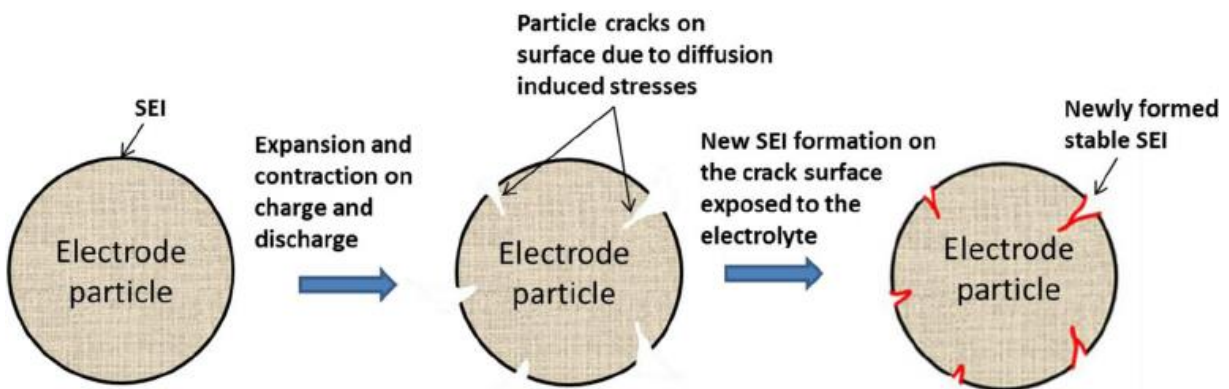


Figure 4-5 Schematic diagram showing capacity loss caused by crack propagation on anode [53].

Our focus is on medium-term cycling during fast charging or by cycling using mild HEV driving cycles therefore potential mechanical deformations are neglected. All the important

degrading factors and mechanisms are taken into account for design of an efficient and comprehensive aging model in next section.

4.2 Implementation of electro-thermal aging model

In this section a thermal model and an aging model are designed and coupled to the electrochemical model (already described in chapter 2) to estimate battery State of Health (SOH). Before deciding on the strategy to model and simulate degradation of our case study, a review on various types of aging models is presented and measurement results of post-mortem are discussed. According to the comparison between different aging modeling methods and more importantly experimental observations, the best strategy is chosen.

4.2.1 Thermal model

Cell temperature plays an important role in the kinetics of charge transfer during intercalation process and in the rate of side reactions. This is the motivation to build a separate thermal model for monitoring of variable cell temperature and to couple it with the electrical fractional model. Thermal management is not the focus of this work, therefore an efficient simple thermal model as proposed in [55] has been implemented.

The thermal model adopts a lumped-parameter approach based on heat transfer equation that is given by:

$$mC_p \frac{dT(t)}{dt} = Q_{\text{gen}}(t) - Q_{\text{loss}}(t) \quad (4-1)$$

The thermal parameters being used are shown in Table 4-3 *Lumped thermal parameters*

Symbol	Parameter	Unit
m	Mass of the cell	g
C_p	Specific heat capacity	J.g-1.K-1
U_{pol}	Polarization voltage	V
R_f	High frequency resistance	m Ω
I	Input current	A
α	Heat transfer coefficient	W.m-2.K
A	Cell surface area	m ²
T_{amb}	Ambient temperature	K

Table 4-3 *Lumped thermal parameters*

The generated heat is obtained by:

$$Q_{\text{gen}}(t) = U_{\text{pol}}(t)I(t) + R_f I(t)^2. \quad (4-2)$$

$U_{\text{pol}}(t)$ characterizes the irreversible heat generation due to polarization of the electrodes. The second term in (4-2), is caused by voltage drop over internal resistor of R_f . The convective exchanged heat with the environment is:

$$Q_{\text{loss}}(t) = \alpha A(T(t) - T_{\text{amb}}). \quad (4-3)$$

4.2.2 Aging Model

Different approaches are found in the literature for battery lifetime estimation and prediction, namely: *analytical models with empirical fitting*, *statistical models*, and *physics-based models*. These three classes of modelling approaches are briefly reviewed in this section.

Analytical models with empirical fitting - The analytical and empirical models account for estimation and prediction of aging parameters through measurements. Empirical models can be parameterised without a comprehensive understanding of the electrochemical cell structure. Empirical models have the advantage of simplicity. The main disadvantages of such models are the inaccuracy of the measurements and not being able to produce a prediction of internal cell behaviour. An example of this methodology, is *Coulomb counting* approach that includes measuring the current flowing in and out of the battery and integrating over time to calculate SOH. This approach can be used in BMS due to its simplicity to apply. However, it requires a recalibration at regular intervals which is a difficult task in real time [56]. Another powerful method is by using information from *Electrochemical Impedance Spectroscopy (EIS)*. In this framework SOH is related to the battery impedance. The advantage of EIS approach is its scalability for various battery chemistries. However it requires laboratory setup and advanced hardware, which makes it no applicable for on-line aging estimation e.g. for EV and HEV cases [57]. *Extended Kalman Filter (EKF)* method which involves in designing of an optimal state observer for nonlinear systems, is another example in this category. G. L. Plett [58] presented a complete solution for extended Kalman filter theory for battery state estimation. One disadvantage of this approach is the computational complexity and lack of stability in case of nonlinear systems such as batteries. Other studies such as the *semi-empirical model* for capacity fade proposed by Ramadass [59] includes an analytical aging estimation method. In this work solvent reduction reaction during charging process is identified as the main source of degradation. Another example is the empirical aging model

developed by Ecker *et al.* [60] that incorporates an impedance-based electric-thermal model coupled to the aging model to simulate the dynamic interaction between aging of the battery and the thermal effects as well as electric behaviour. Another interesting work in this category, is the cycle life model implemented by Ning *et al.* [61]. It is the first principle cycle life model based on lithium ion loss in the parasitic reaction and film resistance rise.

Statistical methods - This type of strategy requires an extensive set of data. Statistical methods are not based on chemical and physical formulations and do not need any analytical information on the aging mechanisms. Precision of statistical approaches depend on data and it may need many full battery characterizations to collect the required data sets. Despite its high accuracy, time-consuming data acquisition makes this type of battery aging estimation method an unrealizable solution for on-board applications [62].

Physics-based models - In this type of aging modelling, the behavior of the battery is correlated to a physical model and the model parameters provide information about the battery performance and conditions e.g. voltage, current, temperature, electrolyte concentration, etc. This type of model can be established according to underlying physical phenomena using a SPM or P2D model. The physics-based models need specific knowledge of the physical and chemical properties of the battery e.g. electrolyte volume, density and porosity of the active materials. They are powerful tools to understand the different interactions between different physical phenomena and the trends about operating condition effects on aging. Another advantage of physical models is that they include all internal battery behavior parameters inherently for more precision. However the implementation of a fully physics-based aging model is questionable on a BMS. Therefore considering some simplifications makes it realizable for online aging estimation [63].

Multimodal, physics-based aging model of Safari *et al.* [65] relates the aging to solvent-decomposition reaction leading to the growth of SEI. The model is able to estimate the calendar and cycle life of Li-ion batteries with good accuracy. An interesting investigation using physics-based methodology concept is done by Pinson and Baznat [64]. Capacity fade prediction of batteries is based on a single particle model. The model has showed accurate fit with experiments. It has been assumed that the SEI formation is the main degradation mechanism. The designed model is also extended to porous electrodes and showed that even at high rates a homogeneous SEI formation occurs within the electrode. Another example in this category is the phenomenological degradation model by Narayanrao *et al.* [65]. In this model the particle fracture, SEI formation and isolation are described in

phenomenological expressions and are coupled with a P2D model. A coupled mechanical-chemical degradation model is proposed by Deshpande *et al.* [66]. They have studied the capacity fade of graphite-LiFePO₄ cells in presence of mechanical fatigue leading to irreversible capacity loss by crack formation. This type of model can be especially used for lifetime prediction until EOL of the cell, and this strategy is thus adopted in the sequel.

4.2.2.1 SEI Growth Model

Based on the observations from post-mortem analysis of the cell under investigation, aging is only considered on the anode side. **Figure 4-6** SDI 28 Ah cell opening at BOL shows an opened SDI 28 Ah fresh cell at BOL and **Figure 4-7** shows the same cell at its EOL. According to the post-mortem experimental observations, aging has essentially happened on the anode. At the surface of the fresh cell anode, some spots can be observed which could be due to high lithiation at the discharged state. The same kinds of spots are visible on the separator at BOL. After cycling and by opening the cell at its EOL, large number of spots are observed at the anode due to aging, which is an evidence for electrolyte decomposition at its interphase with electrolyte. However, no significant change is seen on the cathode. At EOL, a change of color can be seen on the separator in the border areas.

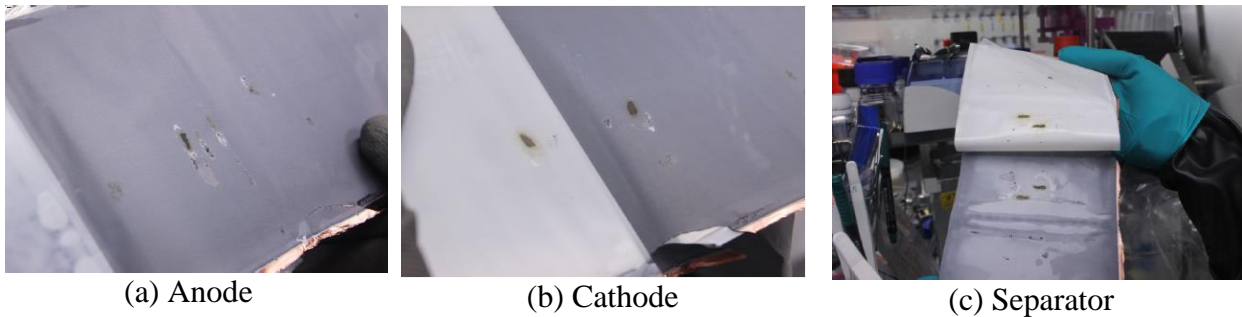


Figure 4-6 SDI 28 Ah cell opening at BOL

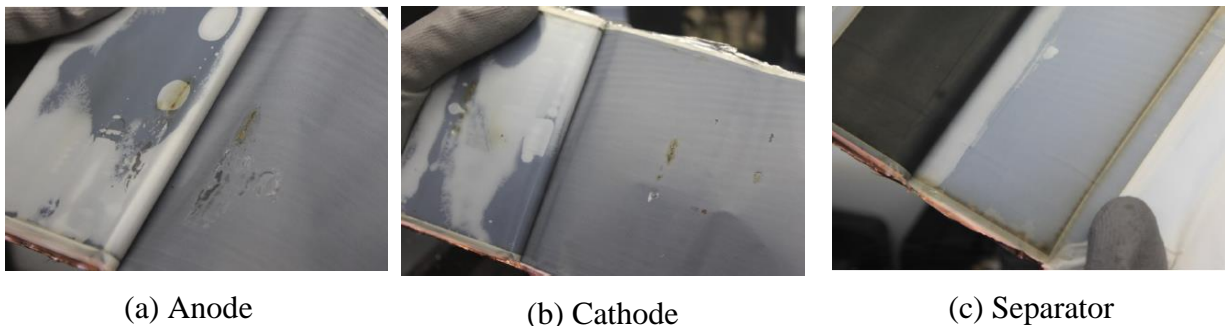


Figure 4-7 SDI 28 Ah cell opening at EOL

In another aging experiment on the same type of cell, charge and discharge cycles using a constant current profile with rate of C/50 is performed both on the anode and the cathode. Respective half-cell discharge capacity is measured as shown in **Table 4-4**. It can be seen that anode has lost around 12% of its initial capacity while the variation of capacity at the cathode is negligible. This is another proof for dominance of aging at the anode side.

Electrode/Aging level	Discharge capacity [mAh]	Rel. capacity
Anode/BOL	5.40 ± 0.03	100%
Anode/EOL	4.75 ± 0.02	88% ± 0.3%
Cathode/BOL	4.83 ± 0.05	100%
Cathode /EOL	4.97 ± 0.08	102.9% ± 1.7%

Table 4-4 Half-cell capacity measurements for SDI 28 Ah at BOL and EOL

The last experiment is carried out on full-cell level by inserting an additional Li-reference electrode. The full-cell OCV as well as half-cell potential of each electrode are measured against the reference electrode at BOL and after cycling by discharging current profile with rate of C/20 within the operating voltage range of SDI 28 Ah cells (V_{min} : 3.0 V and V_{max} : 4.15 V). The same test has been repeated on two samples of the same cell in the experimental set-up shown in **Figure 4-8**:

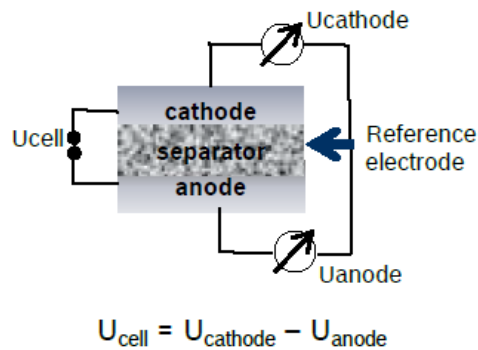


Figure 4-8 Full cell with reference electrode

The comparison between the OCP and OCV of aged and fresh cells are shown in **Figure 4-9**.

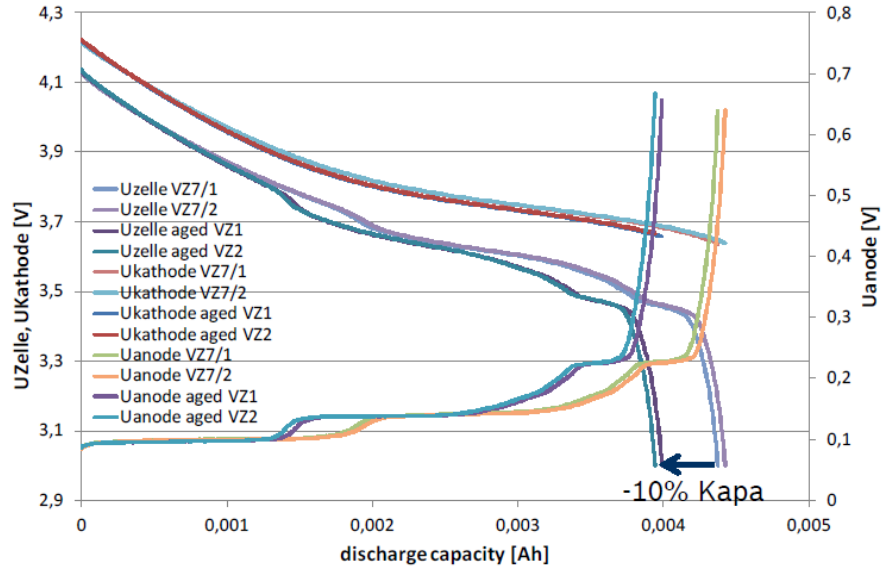


Figure 4-9 Variation of half-cell OCVs and full-cell OCV curves with aging

The study by Imamura *et al.* [67] suggests that such a change in the OCV curve of an aged cell is correlated to capacity fade as a consequence of cyclable Li-ion loss. The relative capacity loss after cycling is around 10%. In these measurements no loss of anode active material is visible.

Based on all the mentioned experimental observations, SEI formation is identified as the main source of aging on the anode. The structure of the SEI growth model is basically driven from the equations proposed in [45]. The side-reaction of interest for aging modeling is given by:



where S stands for the solvent and P for the undesired product of the side reaction. **Figure 4-10** shows the main intercalation reaction as well as the unwanted reaction of electrons with solvent and mobile Li ions inducing SEI formation.

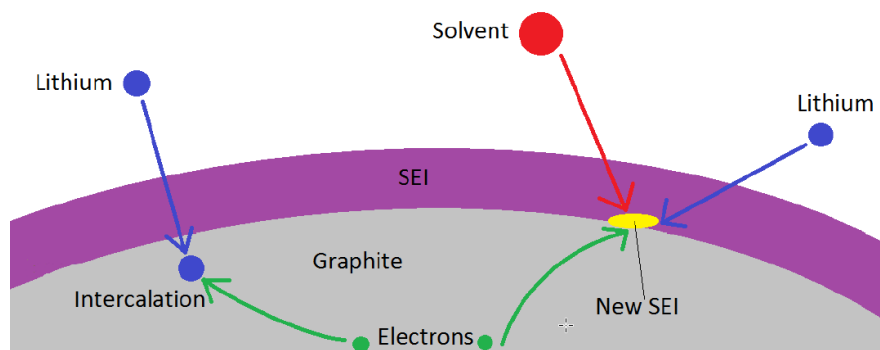


Figure 4-10 Desired intercalation reaction vs. undesired SEI formation at the interphase of anode and electrolyte [64]

Assuming a constant temperature T , Tafel equation calculates the current (denoted by j_{sr}) produced by the side reaction, as a result of undesired reduction of Li ions:

$$j_{sr} = -a_s^n j_{0,sei} \exp\left(-\frac{nF\alpha_n}{RT}\eta_{sei}\right). \quad (4-5)$$

Thus the remaining current for the diffusion reaction j_{remain} , is calculated by subtraction of the main intercalation reaction j_i , and the side reaction current given by relation:

$$j_{remain} = j_i - j_{sr}. \quad (4-6)$$

All the electrochemical parameters and respective values and units are defined in Table 4-5. Some parameters are directly taken from [45] and the rest have been obtained by fitting to the measurements on the cell under investigation.

Symbol	Parameter	Unit
a_s^n	Specific surface area	m ⁻¹
$j_{0,sei}$	Exchange current density	A.m ⁻²
α_n	Symmetry factor	-
n	Number of transferred electrons	-
E_a	Activation Energy	kJ.mol ⁻¹
δ_{sei}	SEI layer thickness	m
M_{sei}	Molar mass of SEI layer	kg.mol ⁻¹
ρ	Density of SEI layer	kg.m ⁻³
κ_{sei}	SEI layer conductivity	S.m ⁻¹
$R_{sei,init}$	Initial resistance of SEI layer	$\Omega.m^2$
R_p	Resistance of side reaction product	$\Omega.m^2$
I_{ch}	Charging current	A

Table 4-5 Aging model parameters

The SEI overpotential η_{sei} , is defined as a function of anode potential φ_{en} , of the potential drop through SEI layer with inner resistance of R_{sei} and of the reference potential of SEI formation U_{sei}^{ref} , assumed to be 0.4 V:

$$\eta_{sei} = \varphi_{en} - R_{sei}I - U_{sei}^{ref}, \quad (4-7)$$

where anode potential φ_{en} is described by:

$$\varphi_{en} = \eta_n + U_n + R_{sei}I. \quad (4-8)$$

As explained in [68], η_n is obtained by manipulating the Butler-Volmer equation that defines the kinetics of Li ion intercalation:

$$\eta_n = \frac{2RT}{F} \sinh^{-1} \left(\frac{j_I}{2a_s^n j_0^n} \right), \quad (4-9)$$

where j_I is the intercalation current density (obtained by subtraction of charging current and side reaction current) and j_0^n is the exchange current density of intercalation reaction. For easier implementation of the model in Simulink, (4-9) is simplified via relation:

$$\eta_n = \frac{2RT}{F} \log \left(\left(\frac{j_I}{2a_s^n j_0^n} \right) + \sqrt{\left(\frac{j_I}{2a_s^n j_0^n} \right)^2 + 1} \right). \quad (4-10)$$

Under fast charging conditions, the increase of temperature has a substantial influence on the rate of side reactions. Therefore (4-5) needs to be modified, in order to consider the Arrhenius dependency of side reaction current to the temperature variation. Equation (4-5) thus becomes:

$$j_{sr} = -a_s^n j_{0,sei} \exp\left(\frac{E_a}{R} \left(\frac{1}{T_{ref}} - \frac{1}{T}\right)\right) \exp\left(-\frac{nF\alpha_n}{RT} \eta_{sei}\right). \quad (4-11)$$

The SEI thickness (δ_{sei}) and resistance (R_{sei}) can be computed by the following relations [45]:

$$\frac{\partial \delta_{sei}}{\partial t} = \frac{M_{sei}}{2F\rho} j_{sr}, \quad (4-12)$$

$$R_p(t) = \frac{\delta_{sei}}{\kappa_{sei}}, \quad (4-13)$$

$$R_{sei}(t) = R_{sei,init} + R_p(t). \quad (4-14)$$

Based on experimental observations [69], the thickness growth of SEI layer decreases gradually after some cycles by primary formation of passivation layer over the surface of electrode. In order to ensure that the SEI growth model provides such a behavior, an exponential term has been added to (4-11). The updated equation obtained is thus:

$$j_{sr} = -a_s^n j_{0,sei} \exp(-\lambda \delta_{sei}) \exp\left(\frac{E_a}{R} \left(\frac{1}{T_{ref}} - \frac{1}{T}\right)\right) \exp\left(-\frac{nF\alpha_n}{RT} \eta_{sei}\right), \quad (4-15)$$

where λ is the SEI decay rate constant (m^{-1}). Figure (4-5) shows the simulation results using the modified aging equation (4-15) and by imposing a 1C charge and discharge current profile with

SOC swing of 70% to the model. Stabilization in the growth of SEI layer is achieved after approximately 150 cycles.

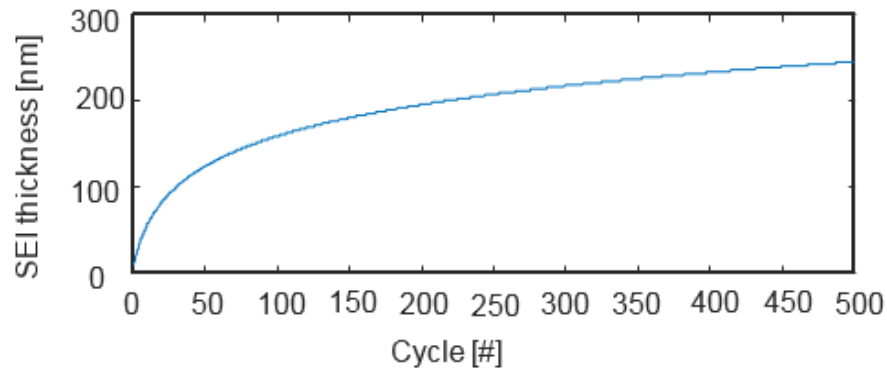


Figure 4-11 SEI layer thickness growth

4.2.2.2 Decoupling of calendar and cycling aging

Figure 4-12 shows the aging measurement in terms of aging rate (mAh.kAh^{-1}), at different C-rates and for certain variation of SOC in the cell. It can be observed that the capacity loss is substantially larger at higher charging C-rates.

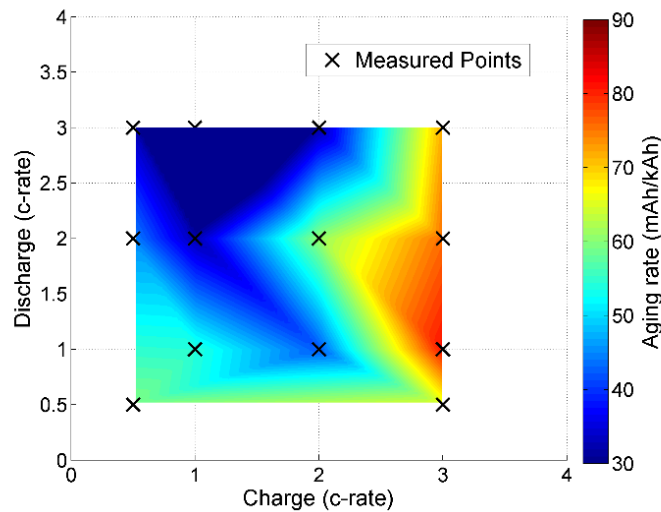


Figure 4-12 Aging map obtained by interpolation of measurement points at different C-rates in SOC range of 15-95%

The aging model should be able to mimic such a behavior with good accuracy in order to guarantee a superior fast charging strategy. Such a requirement was impossible with (4-15) and that is why an additional coefficient K_η has been introduced in order to scale the inverse Butler-Volmer overpotential η_n . Equation (4-15) is thus rewritten as:

$$j_{sr} = -a_s^n j_{0,sei} \exp(-\lambda \delta_{sei}) \exp\left(\frac{E_a}{R} \left(\frac{1}{T_{ref}} - \frac{1}{T}\right)\right) \exp\left(\frac{-nF\alpha_n}{RT} (K_\eta \eta_n + U_n - U_{sei}^{ref})\right), \quad (4-16)$$

or

$$j_{sr} = C_T \exp(-\lambda \delta_{sei}) \exp\left(\frac{-E_a}{RT}\right) \exp\left(\frac{-nF\alpha_n}{RT} K_\eta \eta_n\right) \exp\left(\frac{-nF\alpha_n}{RT} U_n\right), \quad (4-17)$$

where

$$C_T = -a_s^n j_{0,sei} \exp\left(\frac{nF\alpha_n}{RT} U_{sei}^{ref}\right) \exp\left(\frac{E_a}{RT_{ref}}\right). \quad (4-18)$$

It can be concluded from (4-18), that the time-dependent (calendar) aging effects and current-dependent (cycling) aging effects have been decoupled. That provides the possibility of better interpretation of each mechanism on the cell aging and to emphasize on the influence of C-rate on capacity fade during cycling and especially fast charging. Equation (4-18) can be rearranged as:

$$j_{sr} = C_T f_1(t) f_2(T) f_3(I_{ch}) f_4(SOC), \quad (4-19)$$

with

$$f_1(t) = \exp(-\lambda \delta_{sei}),$$

$$f_2(T) = \exp\left(\frac{-E_a}{RT}\right),$$

$$f_3(I_{ch}) = \exp\left(\frac{-nF\alpha_n}{RT} K_\eta \eta_n\right),$$

$$f_4(SOC) = \exp\left(\frac{-nF\alpha_n}{RT} U_n\right).$$

To the author's best knowledge, this study is the first one, proposing a physically-based battery model capable of showing the dependency of degradation mechanisms as a function of SOC, temperature and C-rate. This feature provides a very good agreement of the model to the experiments. By starting the charging process at higher SOC levels, activation energy of parasitic reactions, which is the energy barrier needs to get overcome, decreases. This results in promoting the rate of side reactions [70]. Therefore it is very useful to monitor the influence of SOC on capacity loss by the decoupled function $f_4(SOC)$.

4.3 Validation of the coupled Electro-thermal aging model

The developed electro-thermal aging model obtained is represented by Figure 4-13. It has been validated by different tests as shown in the next sections, verifying the requirements for correct prediction of battery behavior based on experimental observations on the cell under study.

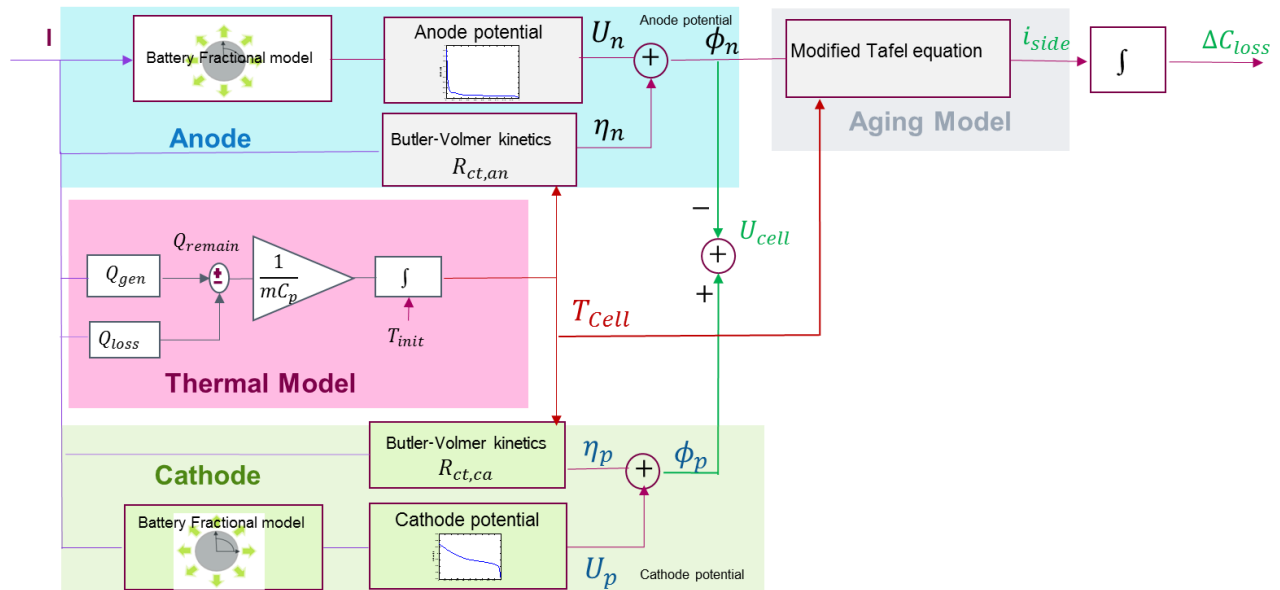


Figure 4-13 Coupled electro-aging thermal model [71]

4.3.1 Validation of the Electro-thermal Model

The implemented electrical fractional model is validated against cell voltage measurements under a dynamic driving cycle conditions changing the SOC of the cell repeatedly from 100% to 0% and vice versa (see **Figure 4-14**). The driving cycle profile, is an extended Artemis drive cycle explained in section 2.3.2 including different driving conditions such as: accelerating, braking, driving uphill and on highways with constant speed, and downhill recuperation.

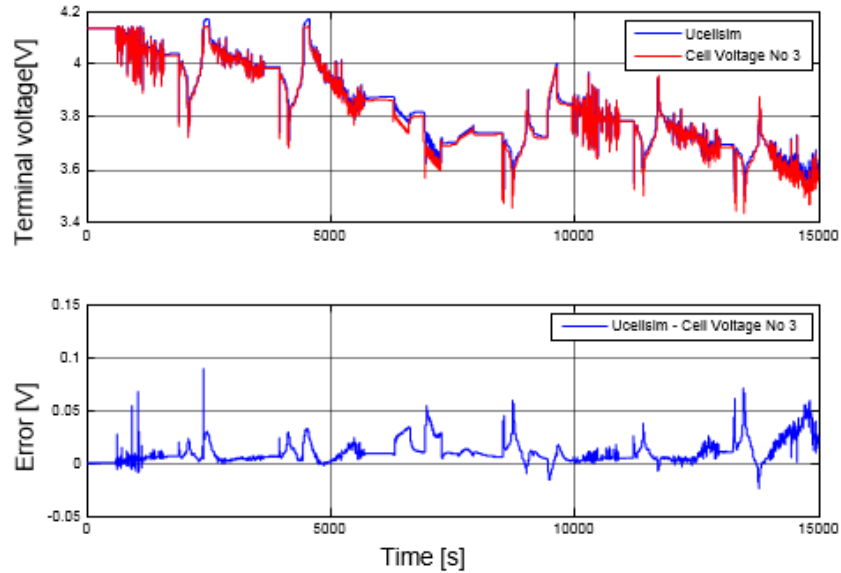
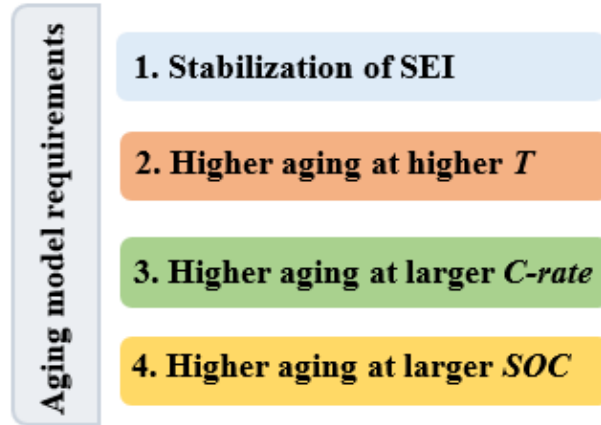


Figure 4-14 Comparison of simulated and measured voltage and the respective absolute error under dynamic driving cycle

Figure 4-14 confirms the validity of the electrical fractional model since the simulated voltage and measured one are in a very good agreement with RMS error of 0.0147 V. The error peaks are due to the nonlinearities not taken into account in the model. The maximum error of 0.09 (V) occurs at deep discharge levels ($SOC < 5\%$) and by abrupt voltage variations during long phases of applying large charging currents.

4.3.2 Validation of Aging Model

According to our experimental observations, a comprehensive aging model is expected to fulfil the requirements sketched in **Figure 4-15**. As explained in section 4.2.2.2 Decoupling of calendar and cycling aging, the aging formula shown by (4-19) is already driven by considering each requirement. The correlation between the requirements and respective sub-functions is clearly displayed in Figure 4-15. The analysis on the SEI growth shown in **Figure 4-11** confirms satisfying of the first requirement.



$$j_{sr} = C_T f_1(t) f_2(T) f_3(I_{ch}) f_4(SOC)$$

Figure 4-15 Aging model requirements

Figure 4-16 represents the influence of the temperature on capacity loss to validate the second requirement. The normalized capacity has been measured by simulating the electro-thermal aging model using a 1C Hybrid Pulse Power (HPC) current profile. The test has been conducted in SOC range of 50 to 60% at three different temperatures of 5, 25, and 45°C. It can be observed that the capacity decreases substantially at elevated temperatures due to higher kinetics of side reactions. Thus the second requirement has been met.

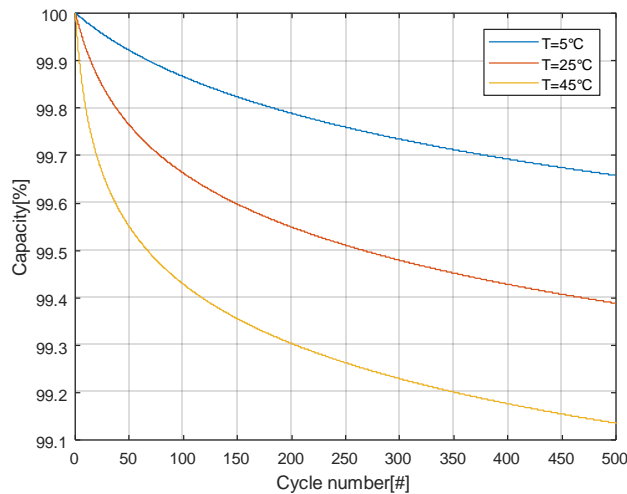


Figure 4-16 Investigation of temperature effect on aging

In order to verify the capability of the aging model in prediction of larger aging at higher C-rate, a validation test is carried out. For this aim, two charge and discharge current profiles are

designed having the same cycle depth and length (correlated to the same calendar aging), one profile with 1C and the other with 3C rate (See **Figure 4-17**).

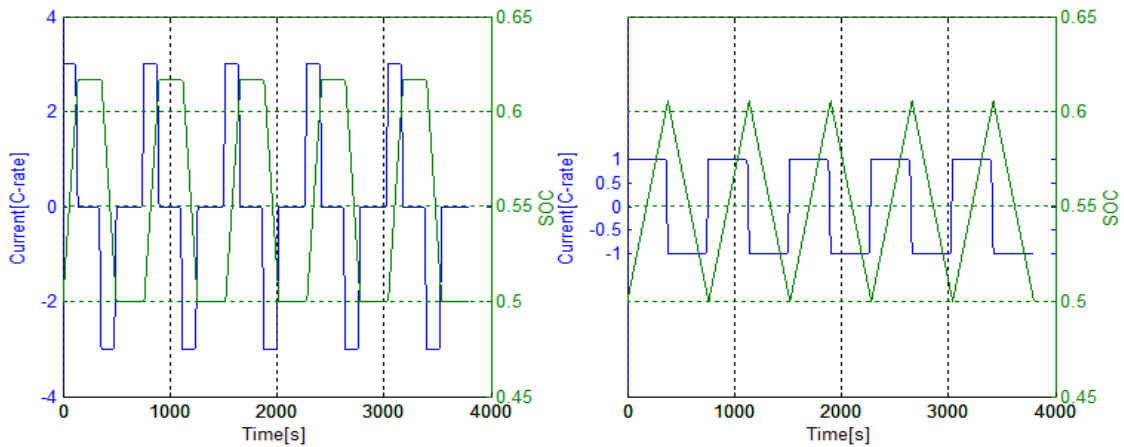


Figure 4-17 1C and 3C charging profiles and respective cycle depth

The mentioned current profile are applied to the developed electro-thermal aging model and the corresponding cell temperature and capacity loss have been measured and compared on the diagrams in **Figure 4-18**. The cell is at initial temperature of 20°C and initial SOC of 50%. There is a significant larger increase in the cell temperature (approximately 6°C increase in temperature for 3C profile comparing to 1.5 °C increase for 1C profile) and consequently a large capacity loss using 3C profile than 1C profile, as expected from a valid aging model.

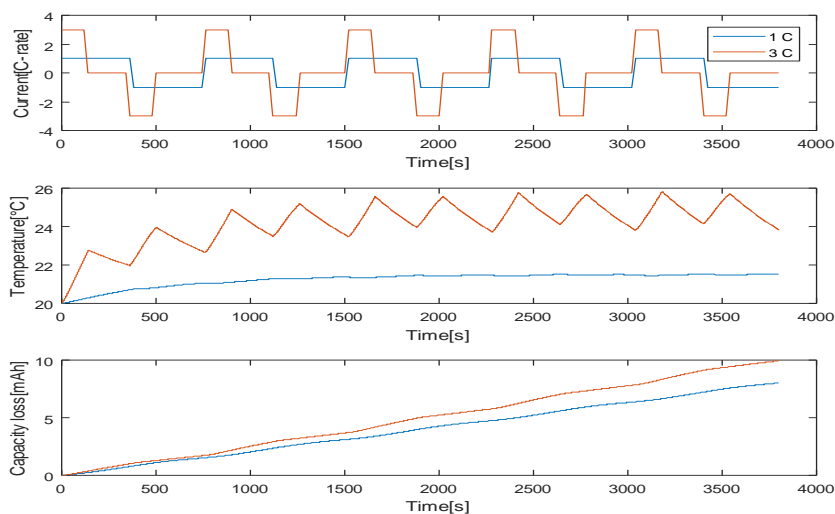


Figure 4-18 1C and 3C validation profiles and corresponding temperature and capacity loss

In another validation test, cyclic behavior of the model after several cycles has been investigated. Thereby the profiles shown in *Figure 4-17* are imposed to the model for 25 cycles at initial temperature of 35°C and initial SOC of 50%. The corresponding capacity loss and temperature are simulated and presented in *Figure 4-19*. Higher temperature increase and capacity loss is obtained for the case of applying a 3C current than 1C current profile.

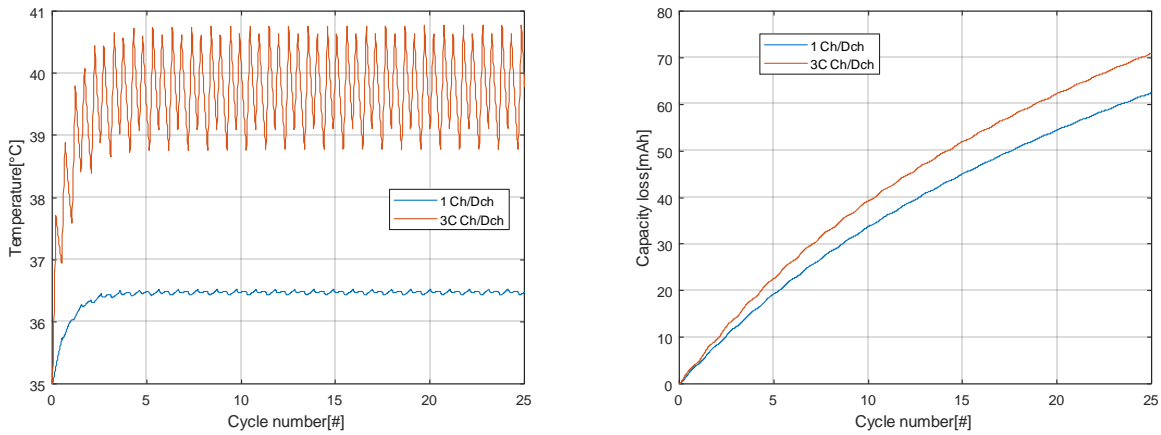


Figure 4-19 Cyclic behavior of the electro-thermal aging model using two different profiles

For a more comprehensive validation to meet the third and fourth requirements, the last validation test has been done to investigate the impact of C-rate and SOC on aging together on an aging map. *Figure 4-20* shows the simulation results on a three dimensional aging map.

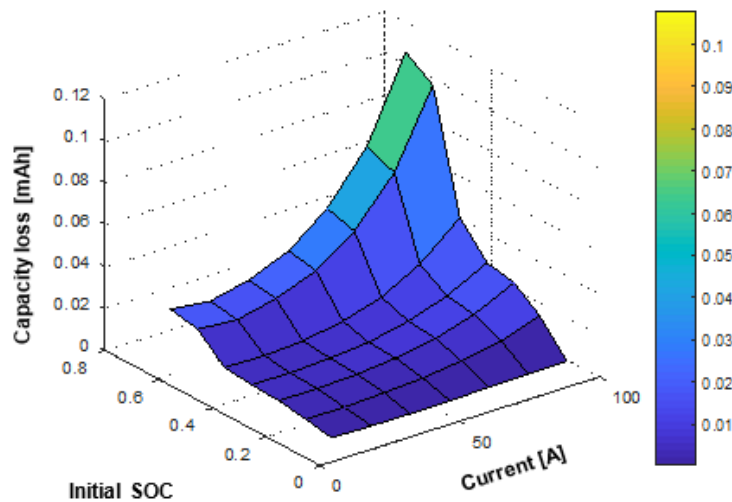


Figure 4-20 Investigation of C-rate and SOC effect on aging

It is obtained by applying a charging pulse current to increase the SOC by 10% at constant temperature of 35°C. The initial SOC varies in interval of 0 to 80% and the charging current ranges

between 0 to 100A. The increase of capacity fade at larger initial SOC and charging currents is very well in accordance with expectation such as the experimental results shown in *Figure 4-12*. Another characteristic of the SEI layer is its larger growth rate during charging rather than discharging. This phenomenon was analyzed on the model.

4.4 Conclusion and future work

A coupled electro-thermal aging model for lithium-ion batteries is proposed in this study based on the requirement of having a model implementable for on-board applications and according to the aging measurement results. The electrical fractional model proposed, captures the low frequency diffusion dynamics (the operating frequency range of BMS) with high accuracy. The aging model is capable of showing the dependency of degradation mechanisms as a function of SOC, temperature and C-rate. It provides the possibility to distinguish between various aging mechanisms and to estimate the contribution of each one to the overall capacity fade. This useful information can be used for developing optimized charging protocols. To the best knowledge of the author, such a global modeling is quite rare in the literature. This feature has led to achieve a very good agreement of the model to the experiments. That is proved with several validation tests. The application of this model for fast charging profile optimization and model-based design of an intelligent charging controller is explained in details in the next chapter.

Chapter 5

INTELLIGENT CHARGING

Summary

5.1 Concept of intelligent charging.....	66
5.2 Trajectory planning	68
5.3 Model linearization	71
5.4 State-space representation of the nonlinear battery system.....	71
5.5 Determination of the system operating points	72
5.6 Uncertain linear model of the nonlinear battery model	73
5.7 Robust controller design	74
5.7.1 Overview of control system design and performance assessment.....	74
5.7.1.1 Output feedback control system.....	74
5.7.1.2 Feedforward control system	77
5.7.1.3 Assessment of control systems.....	77
5.7.1.3.1 Plant Stability	77
5.7.1.3.2 Uncertainty and robustness.....	78
5.7.2 Closed-loop control.....	78
5.7.2 CRONE control methodology.....	79
5.7.2.1 Three generations of Crone controller.....	80
5.7.2.2 3 rd generation of Crone controller	82
5.7.3 CRONE controller design	84
5.7.4 CRONE controller performance analysis	87
5.7.5 Conclusion and future work.....	90

5.1 Concept of intelligent charging and bibliography analysis

Relatively long charging time of Li-ion batteries is a barrier to their commercialization for application of automotive industry. In order to accelerate the charging process, aggressive charging profiles are applied to reach the desired State of Charge (SOC). This leads to evolution of higher internal cell temperature and consequently acceleration of undesirable side reactions. The side reactions consume the Li ions and prevent them to take part into the intercalation reaction. This phenomenon gives rise to aging and poor performance of the Li-ion batteries.

As already discussed in chapter 1, in order to tackle this problem, it is necessary to optimize the operation methods of batteries. The operation during discharging depends mainly on the demand of the user, while the charging method can be improved by the manufacturer to decrease the charging time while minimizing the aging effects.

The Battery Management Systems has been widely used in the electric vehicles for non-destructive detection of the battery states. This includes monitoring the State of Charge, the State of Health (SOH), the internal cell temperature and controlling the battery charging current to minimize the charging time and its impact on aging.

Figure 5-1 shows a block diagram of the fast charging functions of a BMS. The battery observer based on the battery model, simulates the behaviour of the battery under various operating conditions. A control-oriented battery model is described in details in [71]. The fast charging controller adapts the operating limitation based on the information obtained from the battery model. Various control strategies have been incorporated to the BMS to control the fast charging process while improving the battery performance. The control scheme can be classified into whether open-loop or closed-loop control.

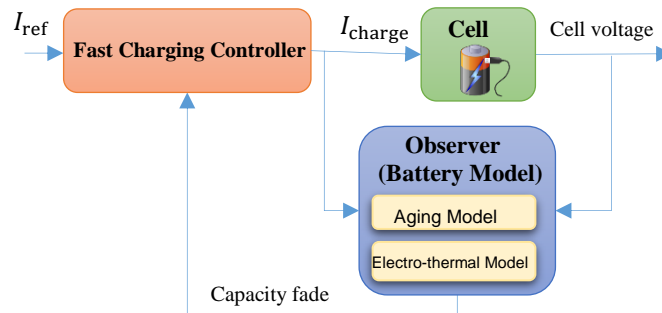


Figure 5-1 Fast charging function in BMS

Several works have been focused on open-loop model-based optimal control of battery charging. Tu Vo [72], used a Taguchi-based algorithm to minimize the effort for finding the optimal profile that meets a trade-off between charging time, energy efficiency and temperature variation. An Equivalent Circuit Model (ECM) is used to derive the battery dynamics while cell degradation is not taken into account. Abdollahi [73], proposed an open-loop optimal charging strategy to find an analytical solution for the current profile by solving an optimization problem. The optimization is to minimize a multi-objective function including time to charge, energy loss and temperature rise index based on a simple ECM. Perez [74] presented the results of an open-loop multi-objective optimization technique, using a more comprehensive battery model consisting of coupled ECM, empirical aging model, and thermal model. The objective function is the weighted sum of charging time and aging.

All the open-loop schemes are highly subject to the parametric uncertainties arising from an inaccurate simplified battery model. Thus a feedback loop is essential for fast charging control to compensate the errors of the model and let the system to adjust its performance for achieving a desired response [75].

Some investigations have been done on closed-loop optimal charging control. Choe [75], has employed a feedback controller to minimize the charging time. The aging is assumed to be caused only by excessive anode surface concentration and increase of temperature which are taken into account as optimization constraints. Battery state detection is done by a physic-based coupled electro-thermal model. In this study, the main problem is with low observability of the states, such as anode and cathode solid-phase concentrations. Klein [76], has introduced a state-feedback Nonlinear Model Predictive Control (NMPC) approach based on a simplified electrochemical model. The objective is minimization of charging time with constraints on temperature and Solid Electrolyte Interphase (SEI) overpotential (identified as root causes of aging). Another work focusing on the use of MPC framework for charging control, is done by Yan [77]. In this study an online genetic algorithm is used within a MPC framework for minimizing charging time while keeping the temperature below a specified maximum limit to lower the battery degradation.

Despite the achieved results, the weakness of MPC approach is lack of robustness with respect to fast variation of state variables such as anode potential. Since the system is highly nonlinear, the linear behaviour could vary depending on the level of the signals (state and input variables). MPC is designed on the nominal plant of the model, but the model parameters can be

uncertain. Besides that, it needs information regarding the exact dynamic behaviour of the system and all of the disturbances, which cannot be easily provided in each control sequence. Thus the MPC strategy is not efficient with respect to disturbances and uncertainties.

Another major shortcoming of the already mentioned closed-loop schemes is the fact that the aging caused by magnitude of applied charging current is not considered in none of the studies. This factor is known to be the main contributor to degradation of the battery during aggressive fast charging [70].

As already discussed, there are still challenges in this growing field of research. This work proposes solutions to address the main challenge regarding:

- implementing an intelligent charging method to achieve fast charging target while minimizing aging caused by temperature and also aggressive charging current by means of a comprehensive battery model
- robustness with respect to large process variations.

Therefore in this chapter first of all, optimal charging problem is formulated in section 5.2 and an example of resulting optimal current profile and respective system response have been shown followed by introducing a novel numerical linearization method in section 5.3 to linearize the battery model. Section 5.4 to 5.6 are devoted to clarify the steps to obtain an appropriate set of linearized models for the design and implementation of the intelligent charging controller. Finally design and implementation of an appropriate fast charging controller is explained in section 5.7.

5.2 Trajectory planning

The model-based charging controller in Figure 5-1, is responsible for finding the optimal charging current profile. Optimal in this case means a current profile as large as possible (to minimize the charging time) while considering a certain time-variant upper bound for the side reaction current. Thus it can be ensured that the fast charging target is achieved while a certain aging is not exceeded. The time-variant value of side reaction current is a function of the SOC and depends on the optimal charging current. It is computed offline before starting the charging process as explained in this section. During charging, the limitation on the side reaction current is provided in a lookup table over SOC. The bound at each time interval, corresponds to the optimal trajectory

for the side reaction current. In the real-time application the controller interpolates the stored data to find the optimal profile.

Therefore, as the first step towards designing a robust controller, a trajectory planning for the charging current and thus for the side reaction current is performed. The aim is to minimize the capacity loss during a fixed charging time of 20 minutes, subject to bounds on the control variable (I_{ch}), in order to avoid exceeding a maximum charging current of 3.5C (where the unit C-rate is the current normalized against the cell capacity of 22.5 Ah) due to safety reasons and to increase the SOC from initial SOC of 5% to a target SOC of 80% (fast charging target in this study) to complete the charging procedure.

For initialization of optimization problem, a Multi-stage Constant Current (MCC) profile is used as it has proved to be a promising candidate for maximizing the energy efficiency, enhancing the battery lifetime during rapid charging [78] and also for its flexibility as it permits to reach large number of shapes for the charging profiles. The MCC profile is equally split into four stages, where each stage has the time range of 5 minutes inspired from the charging profile proposed by Tu Vo *et al.* [72]. Therefore, the following relation formulates the optimal control problem:

$$\min_{I_{ch}(t)} \int_0^{t_f} \Delta C_{loss}(t) dt \quad (5-1)$$

subject to:

$$\dot{x}(t) = f(x(t), I_{ch}(t)), x(0) = x_0 \quad (5-2)$$

$$\frac{1}{3600} \int_0^{t_f} I_{ch}(t) dt \geq Q_{trans} , \quad (5-3)$$

$$0 \leq I_{ch}(t) \leq 3.5C \quad (5-4)$$

where $\Delta C_{loss}(t)$ is the capacity loss (A.h), $x(t)$ is system state variable vector, $Q_{trans}(t)$ is the amount of Lithium ions transferred by charging in (A.h), and t_f (s) is the charging time. The nonlinear constrained optimal control problem has been solved using Sequential Quadratic Programming (SQP) under various operating conditions.

Figure 5-2 shows the optimization result and corresponding SOC, capacity loss, side reaction, and anode potential variation at 35°C in comparison with a conventional Constant Current

Constant Voltage (CCCV) profile. It can be observed that using the optimal current profile the capacity loss has been decreased by approximately 15% in comparison with a CCCV profile. The optimization is performed for various ambient temperatures of 10, 17, 27, 30, 47, and 77°C and various aging levels, starting from Begin of Life (BOL) to Middle of Life (MOL) and finally End of Life (EOL).

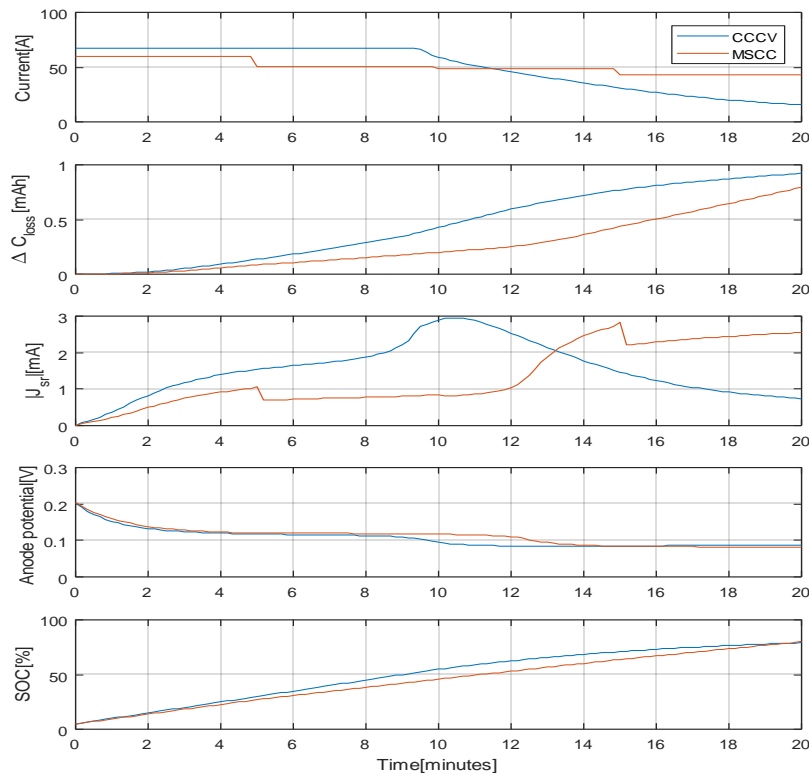


Figure 5-2 Trajectories obtained at $T=35^{\circ}\text{C}$ for a cell at BOL in SOC range of 5-80% with fixed charging time of 20 minutes

This section presented the optimization of the charging current profile for a perfectly known cell. Unfortunately, this ideal case does not exist and applying an optimized charging current does not necessarily lead to reach the target SOC with minimum amount of aging. Thus as explained in section 5.1, a closed-loop strategy should be developed. Another problem encountered in the trajectory planning was the comparably long simulation time of the optimization script. This problem will be addressed in details in chapter 6.

As it can be observed from Figure 5-2, the side reaction current J_{sr} is highly sensitive to the charging current that provokes aging. Therefore it has been chosen as the control signal to manage the charging process.

5.3 Model linearization

In sections 5.1 and 5.2, the necessity of having a closed-loop control scheme was discussed. It is proposed to design a linear controller using a linearized model of the cell.

The battery model used for this purpose is the model developed and explained in chapter 4 (shown in *Figure 4-13*), a physically-based single particle model that represents the underlying electrochemical phenomena with optimized number of parameters and reasonable computational effort. It consists of three coupled sub-models:

- an electrical sub-model, based on a fractional transfer function used to estimate the ion concentration variation during charge and discharge and to simulate the terminal voltage;
- an aging sub-model, used to simulate the degradation processes mainly happening inside the Solid Electrolyte Interphase (SEI) layer on the anode;
- a lumped-parameter thermal sub-model to predict the temperature of the cell and its impact on aging and kinetics of lithium intercalation.

Such a model is highly nonlinear. The simulation results show a large nonlinearity and high sensitivity in the battery model response especially at different stages of lifetime, temperature variation, and level of charging current. This nonlinear behaviour is taken into account through a set of linearized models computed for particular operating points (whether stage of life, temperature or charging current) and different optimized charging profiles and thus corresponding side reaction current (J_{sr}) profiles.

5.4 State-space representation of the nonlinear battery system

The battery model can be represented by the nonlinear state-space model:

$$\begin{cases} \dot{x}(t) = f(x(t), u(t)) \\ y(t) = g(x(t), u(t)) \end{cases} \quad (5-5)$$

where the input $u(t)$ is the charging current $I_{ch}(t)$, the output vector $y(t)$ and the state vector $x(t)$ are described by the following relations:

$$x = [\Delta C_{loss}, \delta_{SEI}, C_{avg,n}, C_1^{part,n} \dots C_5^{part,n}, C_{avg,p}, C_1^{part,p} \dots C_5^{part,p}]^T, \quad (5-6)$$

$$y = [J_{sr}, U_{bat}, \phi_{en}, OCV, T, SOC]^T. \quad (5-7)$$

Symbol	Parameter	Unit
ΔC_{loss}	Capacity loss	mA.h
δ_{SEI}	SEI layer thickness	m
C_{avg,i^*}	Electrode average concentration	A.h
$C_{1...5}^{part,i^*}$	Electrode partial concentration	A.h
U_{bat}	Battery terminal voltage	V
ϕ_{en}	Anode potential	V
OCV	Open Circuit Voltage	V

* i= n (anode) or, p (cathode)

Table 5-1 Battery state and output variables

The approach to represent such a nonlinear model by a set of linear models (each one for a specific operating point) is described in the next part.

5.5 Determination of the system operating points

The operating points are defined based on a set of optimized charging profiles obtained in section 5.2. The optimization is performed for different ambient temperatures and aging levels in the SOC range of 5-80%. For each optimal MCC current profile, in addition to constant current phases, relaxation intervals are considered to reach equilibrium conditions. Taking into account 18 ambient (and internal) temperatures, 8 operating conditions provided by each charging profile, and 3 aging levels, a total of 432 operating points are identified. **Figure 5-3** represents an example of determining the operating points under steady-state conditions. All the corresponding state-variables have been recorded as well.

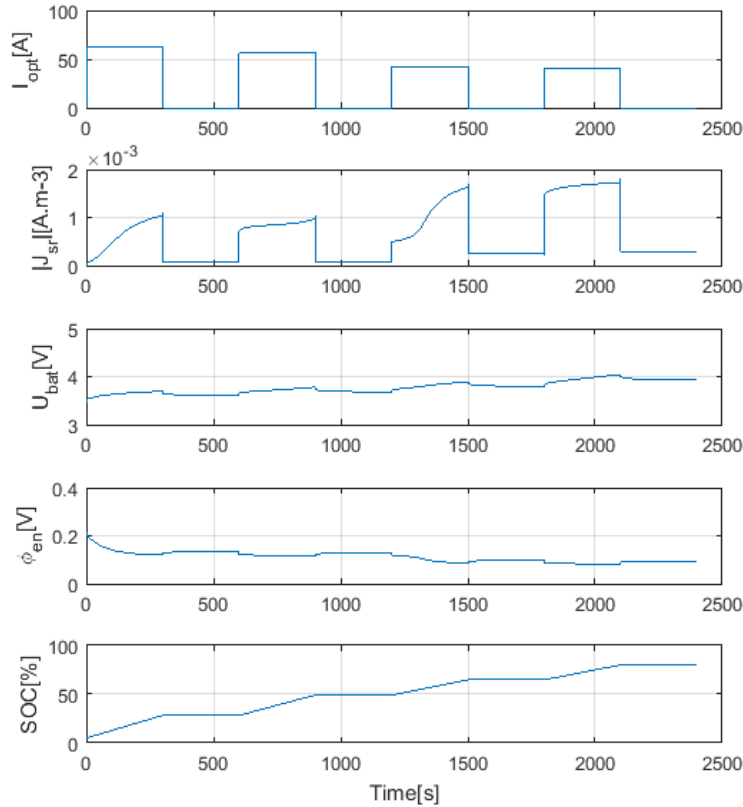


Figure 5-3 Determination of operating points for an optimal charging profile at 10°C and BOL.

5.6 Uncertain linear model of the nonlinear battery model

Using a numerical linearization method (*linmod* command in *Matlab*), the model is then linearized around the set of operating points. For this purpose, the states are parametrized with the equilibrium values obtained in section 5.5. The set of 432 uncertain linear models of transfer function $J_{sr}(s)/I_{ch}(s)$ using a logarithmically spaced frequency distribution are presented in Bode plot of **Figure 5-4**. This diagram permits a good definition of the uncertain frequency response of the plant. Among these set of uncertain linear transfer functions, one is arbitrarily chosen as the nominal one. It can be seen that the magnitude of this transfer function $J_{sr}(s)/I_{ch}(s)$ depends strongly on the operating point. The resulting uncertainty in the gain and phase can be used to design a fast charging robust controller.

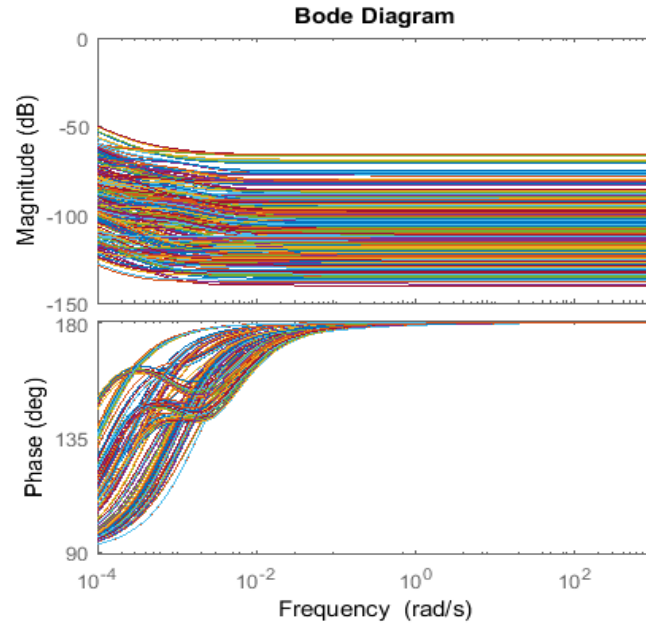


Figure 5-4 Frequency responses of transfer function $J_{sr}(s)/I_{ch}(s)$ for various operating points

5.7 Robust controller design

After linearization of the battery model, an appropriate robust controller can be designed and associated to the original model to accomplish desired performance for the overall system. The following section summarizes an overview of different types of control strategies and the methods to evaluate their performance that can be used for this purpose.

5.7.1 Overview of control system design and performance assessment

In this part, a general review on the concept of feedback and feedforward controller design is presented, followed by a section explaining about the criteria for stability and robustness evaluation.

5.7.1.1 Output feedback control system

Assuming a Single Input Single Output (SISO) system, **Figure 5-5** represents the concept of output unity negative feedback control system. The control system component are introduced in Table 5-2. The measured output is compared with the reference value ($y_{ref}(t)$) and the controller computes a corrective action to achieve a desired performance.

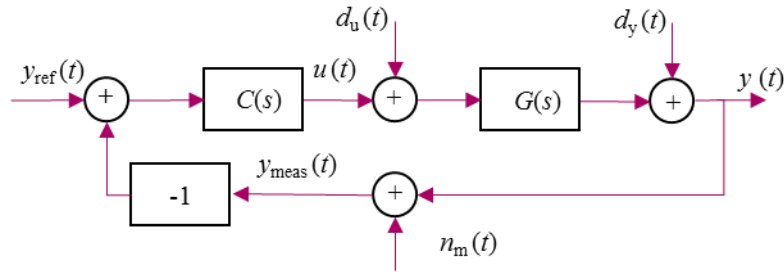


Figure 5-5 Unity-feedback control system

Symbol	Description
$G(s)$	Transfer function of linear plant model
$u(t)$	Control effort input
$y(t)$	Output (controlled signal)
$y_{meas}(t)$	Measured output (e.g. measured by sensor)
$C(s)$	Transfer function of controller
$y_{ref}(t)$	Reference value of output
$d_u(t)$	Disturbance on the plant input
$d_y(t)$	Disturbance on the plant output
$n_m(t)$	High frequency measurement noise

Table 5-2 Unity-feedback Control system components

The control system in Figure 5-5 is influenced by four external signals, the reference signal, the disturbance on the plant input, the disturbance on the plant output and the measurement noise. The variation of control signal, measured output, disturbance on output and disturbance on the control signal with respect to each other are of great interest for control engineering problems. The following relations are the closed-loop transfer functions of interest (for simplicity of relations, the argument of all Laplace transforms are dropped):

$$T = \frac{Y_{meas}}{Y_{ref}} = -\frac{Y_{meas}}{N_m} = -\frac{U}{P_u} = \frac{GC}{1 + GC'} \quad (5-8)$$

$$S = \frac{Y_{meas}}{P_y} = \frac{1}{1 + GC'} \quad (5-9)$$

$$SG = \frac{Y_{meas}}{P_u} = \frac{G}{1 + GC'} \quad (5-10)$$

$$CS = \frac{U}{Y_{ref}} = -\frac{U}{N_m} = \frac{U}{P_y} = \frac{C}{1 + CG} \quad (5-11)$$

These transfer functions are able to fully characterize a unity-feedback control system and their interesting properties can be used for the design of controllers.

Based on the previous set of equations, function S can be re-written as the ratio between relative uncertainties of T and G by:

$$S = \frac{\frac{\partial T}{T}}{\frac{\partial G}{G}} \quad (5-12)$$

It actually maps the output/input gain variation against the plant uncertainty, therefore it is called *sensitivity function*. Respectively, T which is obtained by:

$$T = 1 - S \quad (5-13)$$

is called *complementary sensitivity function*. Accordingly relation (5-10), mapping the output to the input disturbance is called *load disturbance* or *input sensitivity function* and equation (5-11) relating the control signal to the measurement noise is called the *noise sensitivity* or *control sensitivity function*.

Various design issues have to be respected for implementation of a control system. Basic requirements such as: stability, reference tracking, robustness disturbance and noise attenuation need to be taken into account depending on the application. For instance, the major goal in process control is often reduction of load disturbance while the main focus of motion control would be reference signal tracking. In this study, the primary target of the controller design is reference tracking in presence of plant uncertainties which is explained in details in section 5.7.3, therefore the requirements for achieving this target are reviewed shortly.

The aim is to observe convergence of the control system output y to the desired reference signal y_{ref} under steady state conditions (long durations or low frequency range). This goal can be achieved by having open-loop gain of $\beta = GC$ much greater than one at low frequencies i.e.:

$$|GC| \gg 1 \rightarrow |T| = \left| \frac{GC}{1 + GC} \right| \approx 1 \quad (5-14)$$

5.7.1.2 Feedforward control system

A controller with two degrees of freedom is shown in **Figure 5-6**. It consists of a feedback controller C_{FB} , mainly to deal with process uncertainties and to reduce the disturbance effects, and a feedforward controller C_{FF} designed to cope with the reference signal and to reduce the settling time of the control system. This kind of design with two degrees of freedom can provide a nice separation of control problem and compromises between the control effort (magnitude of control sensitivity function CS) and the bandwidth.

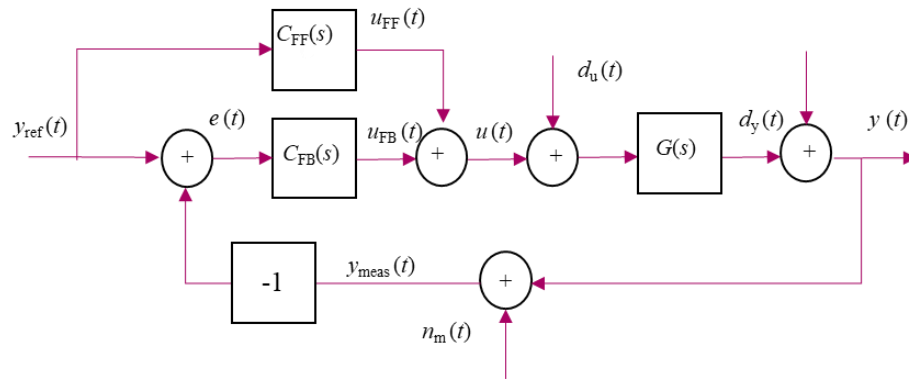


Figure 5-6 Feedback-Feedforward control system

5.7.1.3 Assessment of control systems

Apart from achieving a good performance from a closed-loop system such as ability to follow the command signal, it is crucial to check its stability and robustness. Next two sections focus on this topic.

5.7.1.3.1 Plant Stability

Stability of the control system can be analysed using the Nyquist stability criterion, but more interesting in this study is to analyse the stability degree of the control system whether based on the open-loop or the closed-loop transfer functions.

Here the main focus is on the closed-loop stability degree which can be obtained whether in time domain or in frequency domain features. The diagram in **Figure 5-7** shows the summary of the ways to estimate the stability degree using both features.



Figure 5-7 Criteria for analysis of stability degree

5.7.1.3.2 Uncertainty and robustness

The other important characteristic of the control system to be investigated is the ability to deal with variations in the plant components. Trade-offs between robustness and performance is a key issue for design. A multiplicative uncertainty $\Delta G(s)$ for a perturbed SISO system $G_{nom}(s)$, can be defined as:

$$G(s) = G_{nom}(s)\Delta G(s). \quad (5-15)$$

The frequency uncertainty domain associated to the Nichols plot of $G_{nom}(s)$ is defined by all the possible values of the pair $\{|\Delta G(j\omega)|, \arg\Delta G(j\omega)\}$. A novel approach for robustification of intelligent charging controller in frequency domain is employed in section 5.7.3 by minimizing the variations in the resonant peak of the complementary sensitivity function. This approach ensures the robustness of time-domain characteristics as well, which is the final goal of robust controller design.

5.7.2 Closed-loop control

As shown by Figure 5-8, the goal is to design a controller with two degrees of freedom using separated controller signals. The robust feedback is to ensure an accurate tracking of the desired output whereas the feedforward permits the initialization of the plant input. In our case study, both the reference signals (optimal trajectories) of the plant model input $I_{Ch,traj}$ and output $J_{sr,traj}$ are available. A Low Pass Filter (LPF) is used to smooth the reference current profiles. When the battery parameters are those used to optimize a charging profiles, the charging current I_{Charge}

permitting the tracking of the optimal $J_{sr,traj}$ equals the feedforward current $I_{Ch,FF}$ and the feedback controller has no effect. In the opposite situation, in presence of process uncertainties, the feedback loop modifies the charging current in order to impose the computed optimal side reaction current to the cell. Since cell voltage U_{cell} , temperature T , and charging current I_{Charge} are the only measurable signals, the side reaction current is estimated by an aging observer based on the cell model.

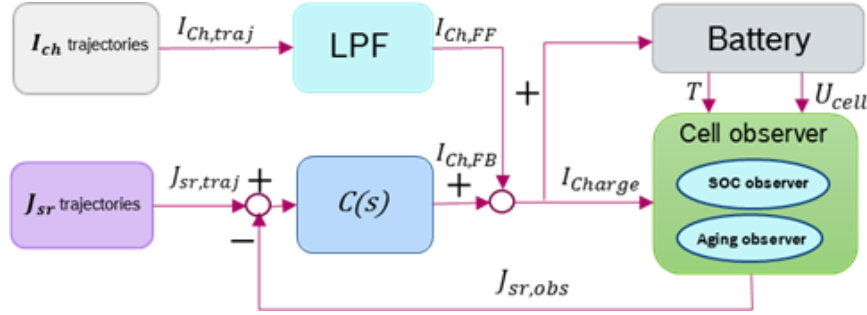


Figure 5-8 Closed-loop configuration for the fast charging control

5.7.2.1 CRONE control methodology

The CRONE control methodology is the strategy used to design the controller $C(s)$ of Figure 5-8 in this study. CRONE is French acronym which means: fractional order robust control. This is a frequency domain based technique that uses fractional differentiation orders as high-level design parameters [79]. Thus the tuning of the controller includes optimization of these parameters.

Fractional controllers can increase the robustness properties of a closed-loop system, as proved by Bode [80]. Based on his proposal, considering uncertainties originating from plant's magnitude, the ideal shape of the Nyquist plot for open loop frequency response $\beta(s)$ is a straight line in the complex plane. $\beta(s)$ has thus a flat Bode phase plot, i.e. even if the gain changes, the gain margin is infinite. Infinite gain margin leads to insensitivity of the plant to the gain variations and that means robustness of the stability degree with respect to the parametric plant perturbation. $\beta(s)$ can ensure such a property also in a closed-loop configuration. As proposed by the CRONE methodology Bode's ideal open loop transfer function can be obtained from the fractional-order transfer function of non-integer order α :

$$\beta(j\omega) = CG(j\omega) = \left(\frac{\omega_{CS}}{s}\right)^\alpha. \quad (5-16)$$

The fractional order α enables parameterization of the open-loop transfer function with a reduced number of parameters.

Another advantage of using CRONE methodology is facilitating non-conservative robust control system with better performance. This feature is due to assessment of well-structured frequency uncertainty domains of the plant (also called templates or perturbations), resulting to avoid overestimation of perturbations and better performance of the overall system.

The above-mentioned interesting characteristics of CRONE methodology makes it a promising candidate to be incorporated in the design and control of unstable systems, time varying plants and, nonlinear systems whose nonlinear behaviors are taken into account by sets of linear equivalent behaviors like our case of study, batteries. [81]

5.7.2.1.1 Three generations of CRONE controller

Three CRONE methods have been developed, successively extending the field of application of each generation in the control system design. In these three methods the controller or open-loop transfer function is defined using fractional order integro-differentiation.

The main criterion for the classification of different generations of Crone controllers is the plant uncertainty origin, whether coming from the gain and/or phase of the plant. According to this criterion, the three generations of CRONE controller are now defined as:

1st Generation- 1st generation of CRONE controller is applicable in the case of observing gain-like perturbations of the plant and constant phase in the frequency range around open loop gain cross-over frequency ω_{cg} . Thus for the configuration shown in Figure 5-5, the controller $C(s)$ is defined by:

$$C(s) = C_0 \left(\frac{\omega_l}{s} + 1 \right)^{n_I} \left(\frac{1 + \frac{s}{\omega_l}}{1 + \frac{s}{\omega_h}} \right)^n \frac{1}{\left(1 + \frac{\omega_F}{s} \right)^{n_F}}. \quad (5-17)$$

It consists of a gain, an integrator, a band-limited fractional order operator in the frequency range of interest $[\omega_l, \omega_h]$, and a low pass filter. The combination of the mentioned operators ensures a limited control effort level and reduction of steady-state errors. The desired closed-loop performance is obtained by tuning of integer parameters n_I, n_F and the fractional order n . A 1st

generation CRONE controller can be considered as a PID controller with a constant phase fractional order derivative part.

2nd Generation- The 2nd generation of Crone controller is used when in addition to gain-like perturbations, plant phase variation is also observed around the gain crossover frequency ω_{cg} . This robust controller is designed based on a fractional order open-loop transfer function inspired by Bode's ideal transfer function explained in section 5.7.1.

$$\beta(s) = \left(\frac{\omega_{cg}}{s}\right)^n \quad (5-18)$$

In order to reach the desired closed-loop behavior, parameters ω_{cg} and n can be tuned resulting a constant phase open-loop frequency response, also called *template*, as presented by the Nichols chart of **Figure 5-9**. Even after vertical displacement of the template, uncertainties shown by the gray area on **Figure 5-9**, does not vary the phase margin M_ϕ and the resonant peak M_r , ensuring the robustness property.

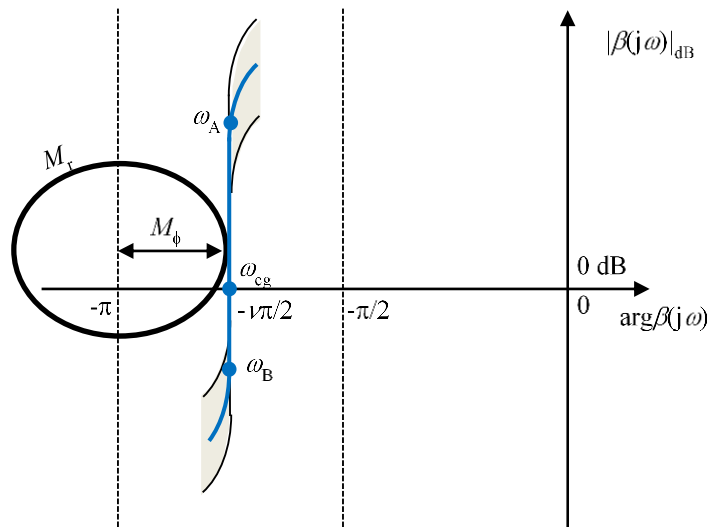


Figure 5-9 Robustness of stability degree in presence of uncertainties for 2nd generation CRONE controller

3rd Generation- By replacing the real fractional order n by a complex order, the 3rd generation of the CRONE controller is defined for any perturbed SISO system. It widens the application domain of the 1st generation by permitting to change gain-crossover frequency and widens the application of the 2nd generation by providing the possibility to handle more general uncertainties using a complex number for the fractional order. As shown in **Figure 5-10**, the vertical template of the

second generation is replaced by a generalized template with any angle. The designing method of 3rd generation CRONE controller is explained in more details in the following section.

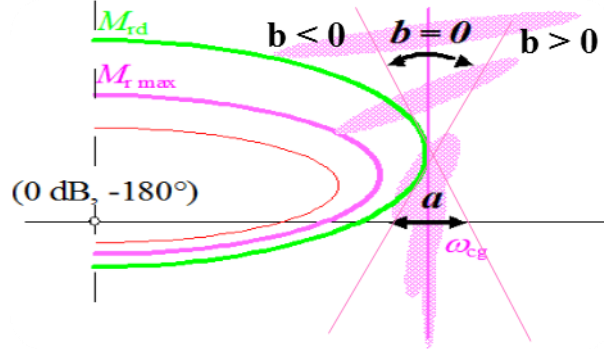


Figure 5-10 Generalized template for the 3rd generation of CRONE controller

5.7.2.1.2 3rd generation of CRONE controller

The main concept of the 3rd generation CRONE controller is to optimize the parameters of a nominal open-loop transfer function $\beta_{nom}(s)$ based on a band-limited complex fractional order integration:

$$\beta_{nom}(s) = \beta_l(s)\beta_m(s)\beta_h(s) \quad (5-19)$$

where $\beta_l(s)$ represents a n_l integer order proportional integrator described by:

$$\beta_l(s) = C_1 \left(\frac{\omega_{N^-}}{s} + 1 \right)^{n_l}, \quad (5-20)$$

and $\beta_m(s)$ is a set of band-limited generalized templates:

$$\beta_m(s) = \prod_{k=-N^-}^{N^+} \beta_{mk}(s), \quad (5-21)$$

with

$$\beta_{mk}(s) = C_k \left(\alpha_k \frac{1 + \frac{s}{\omega_{k+1}}}{1 + \frac{s}{\omega_k}} \right)^{a_k} \left(\Re_i \left\{ \left(\alpha_k \frac{1 + \frac{s}{\omega_{k+1}}}{1 + \frac{s}{\omega_k}} \right)^{ib_k} \right\} \right)^{-q_k \text{sign}(b_k)} \quad (5-22)$$

where

$$\alpha_k = \left(\frac{\omega_{k+1}}{\omega_k}\right)^{0.5} \text{ for } k \neq 0, \text{ and } \alpha_0 = \left(\frac{1 + \left(\frac{\omega_r}{\omega_0}\right)^2}{1 + \left(\frac{\omega_r}{\omega_1}\right)^2}\right)^{0.5} \quad (5-23)$$

and $\beta_h(s)$ is a low-pass filter of order n_h :

$$\beta_h(s) = C_h \left(\frac{s}{\omega_{N^+}} + 1\right)^{-n_h}. \quad (5-24)$$

Order n_l can be tuned to cancel steady-state error and reach the desired controller accuracy. C_l , C_k , and C_h are adjusted in a way to set ω_r as the resonant frequency. By modifying the value of order n_h , a proper or strictly proper controller can be achieved. The optimization of the open-loop parameters are done in a way to minimize the variations of the resonant peak M_r of the complementary sensitivity function $T(s)$, which is equivalent to minimizing the following robustness objective function:

$$J = \sup_G M_r - M_{rnom} \quad (5-25)$$

where M_{rnom} is a desired value of the nominal closed-loop resonant peak (for the nominal plant G_{nom}), while considering the following set of performance inequality constraints on the sensitivity functions for $\omega \in R^+$:

$$\begin{aligned} \inf_G |T(j\omega)| &\geq T_1(\omega), \quad \sup_G |T(j\omega)| \leq T_u(\omega) \\ \sup_G |S(j\omega)| &\leq S_u(\omega), \quad \sup_G |CS(j\omega)| \leq CS_u(\omega) \\ \sup_G |GS(j\omega)| &\leq GS_u(\omega) \end{aligned} \quad (5-26)$$

where $T(s)$, $S(s)$, $CS(s)$, and $SG(s)$ are defined by relations (5-8) to (5-11).

In the Nichols chart, the frequency uncertainty domains of the open-loop frequency response are invariant and equal to those of the plant. By minimizing J in (5-25), the optimal parameters place the uncertainty frequency domains so that they overlap as little as possible with the low stability margin areas of the Nichols chart. Since the uncertainties are taken into account by the least conservative method, only a nonlinear optimization method can be used. For $N^- = N^+ = 0$ in (5-21), only four independent open-loop parameters should be optimized. They can be ω_0 ,

ω_l , ω_r and $Y_r = |\beta(j\omega_r)|_{dB}$. The other open loop parameters such as a_0 and b_0 are then derived in order to ensure the tangency of $G_{nom}(j\omega)$ to the desired M_{nom} circle of the Nichols chart.

Finally, the closed-loop fractional controller $C(s)$ can be found from the ratio of the frequency responses of the optimal open-loop and nominal plant inversion:

$$C_F(j\omega) = \frac{\beta_{nom}(j\omega)}{G_{nom}(j\omega)}. \quad (5-27)$$

For this purpose, by means of an appropriate frequency domain system identification method such as pole/zero allocation, parameters of an integer-order transfer $C_R(s)$ function are tuned to fit the ideal frequency response of $C_F(s)$. An advantage of this design method is that low values of the controller order (usually less than 6) can be used, regardless of the control problem complexity. Besides that, avoiding overestimation of plant perturbation leads to achieve a better performance by implementing a non-conservative robust control system.

5.7.3 CRONE controller design

The gain behavior of the plant is respectively of order 1 and 0 at low and high frequencies. Thus, the open loop orders $n_l = 2$ and $n_h = 1$ ensure that the controller behaves as an integrator at low-frequency and as a low-pass filter at high-frequency. The parameters of the nominal open-loop transfer function (5-19) are optimized to minimize the variation of complementary sensitivity function resonant peak through criterion (5-25) and to ensure the following design specifications:

- a nominal resonant peak M_{Tnom} of T of 1.7dB for a small nominal overshoot of the step response corresponding to the reference signal of J_{sr} ;
- a resonant peak of sensitivity function S lower than 6dB to achieve a good stability degree;
- a bandwidth of higher than 0.2 rad/s;
- control effort noise lower than 10A (I_{ch}) for a 10^{-5} A high-frequency variation of J_{sr} .

The optimal parameters of the open-loop plant meeting the specified requirements are obtained using the CRONE control toolbox [28, 82]. They are: $Y_r = 3.8 \text{ dB}$, $\omega_r = 1.5 \text{ rad.s}^{-1}$, $\omega_0 = 0.1 \text{ rad.s}^{-1}$ and $\omega_1 = 7.5 \text{ rad.s}^{-1}$. Thus, the fractional integration order is given by $a_0 = 1.42$ and $b_0 = -0.46$. **Figure 5-11** shows the Nichols chart of the optimized nominal transfer function and respective frequency uncertainty domains. It can be seen that the closed-loop system is stable since the nominal open-loop and its corresponding uncertainty domains are far enough from the

instability point ($-180^\circ, 0 \text{ dB}$). The green curve is actually a set of convex hulls, where each convex hull defines the frequency uncertainty domain of $G(j\omega)$ for a specific frequency. The Nichols chart contains all the possible values of $G(j\omega)$ for frequencies logarithmically spaced between 10^{-4} rad/s and 10^3 rad/s .

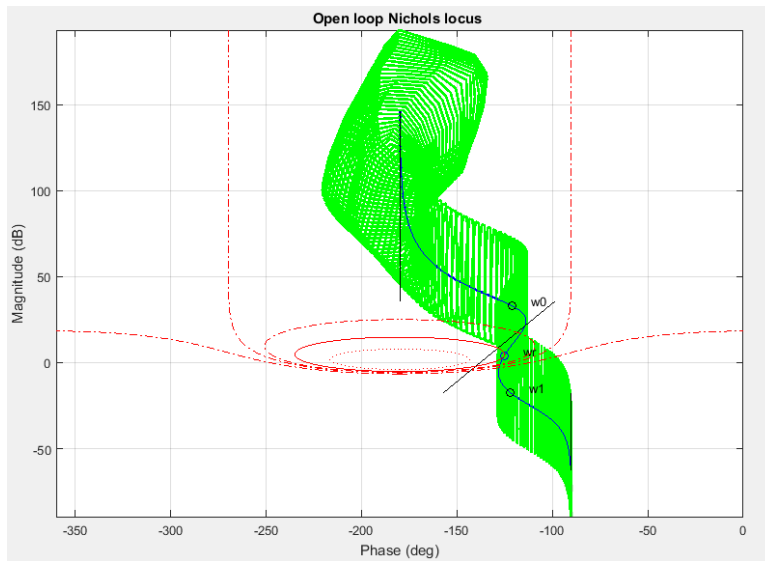


Figure 5-11 Nichols chart of the nominal plant and associated uncertainties

At this step, fulfilling the design specifications is verified using the magnitude plots of the four sensitivity functions in Figure 5-12. The magnitude of the complementary sensitivity function T , sensitivity function S , load disturbance sensitivity function SG and control sensitivity function KS do not cross the defined constraints (dashed lines). The small resonant peaks on T and S functions ensure the robustness. As the plant output has to converge to a reference value, for low frequency (long durations) the complementary sensitivity function T , has to be close to one (0 dB) within this frequency range.

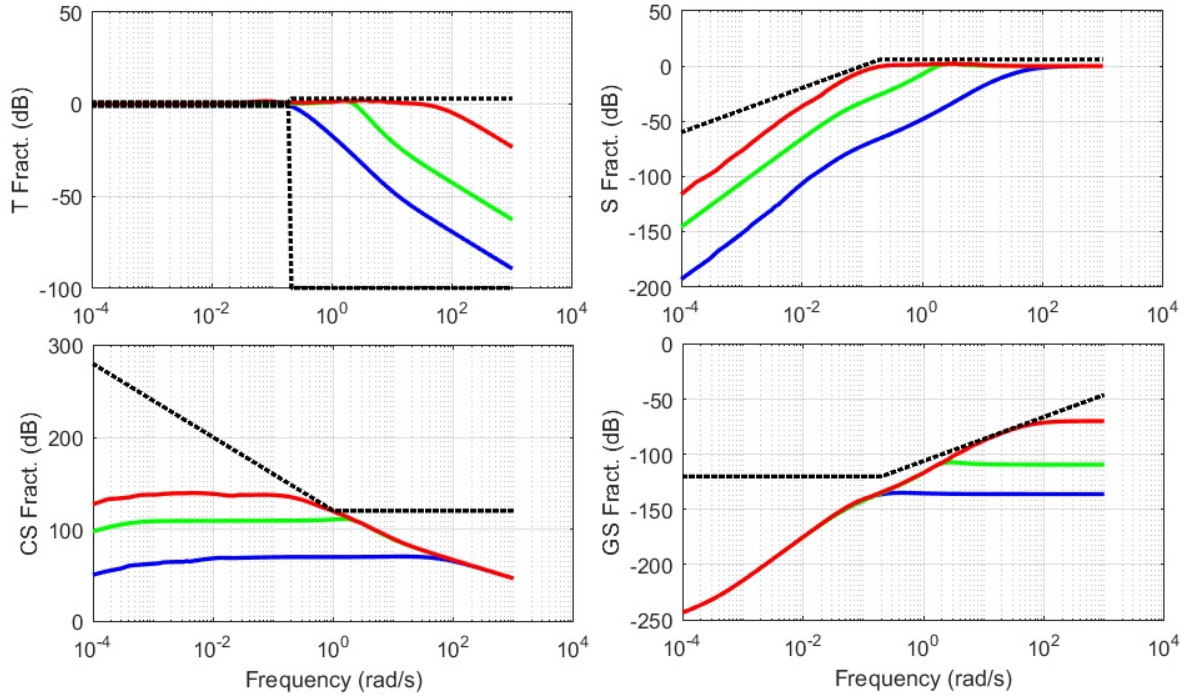


Figure 5-12 Magnitude plots of the four sensitivity functions

From the desired frequency response of the controller, an order 4 rational transfer function is synthesized. The block diagram is shown in Figure 5-13.

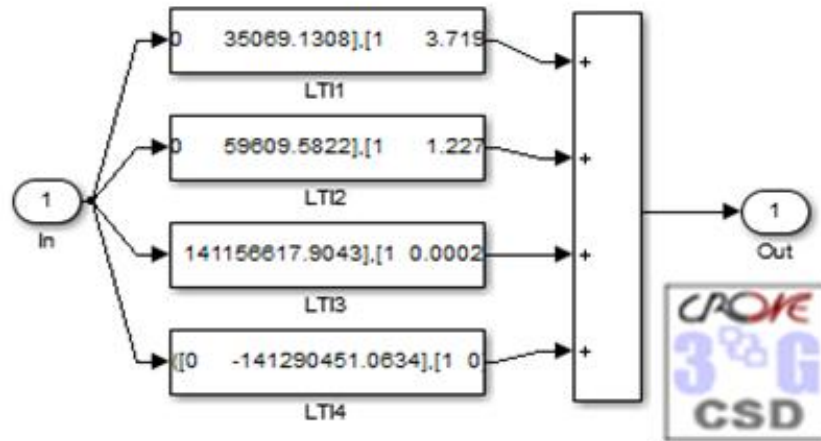


Figure 5-13 3rd generation CRONE controller

Due to the integrating nature of the designed controller, it was observed that the output charging current exceeds saturated value of the input current and the windup phenomenon could lead to instability of the closed-loop system. On the other hand, applying large input currents results in short settling time for the system which is desirable. Thus in case of windup phenomenon, a

promising solution used in this work is to feedback the integral part of the linear controller so that the controller output remains close to the saturated values during saturation time. The concept is depicted in Figure 5-14, where the anti-windup system is incorporated with the primary controller.

Figure 5-14 represents the block diagram of the resulting controller. It is able to suppress the undesired increase of charging current due to the integrator error accumulation. The safety limit for the battery under investigation is the maximum charging current of 3.5 C.

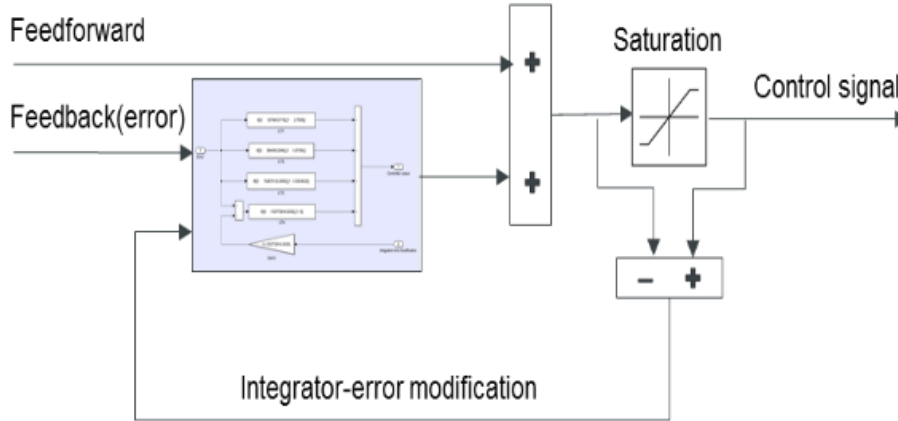


Figure 5-14 Block diagram of the fast charging controller

5.7.4 CRONE controller performance analysis

The fast charging controller is implemented in the control loop of *Figure 5-8* including the nonlinear battery model described in chapter 4. Battery dynamics vary by aging and large temperature variation. Thus the sensitivity of the closed-loop system to the process dynamics is an important issue that should be dealt. In order to investigate the performance and robustness of the controller to changes in the battery parameter values, a robustness analysis has been made, where the changes in the system response is monitored with response to relative changes in the battery parameters. *Figure 5-15* presents the tracking of a previously optimized side reaction profile at 10°C, for the cell at BOL, but with a model in which parameters indicating the aging, including the cell high frequency resistance (Ω), cell actual capacity (Ah), initial thickness of SEI layer (nm), and specific surface area of anode (m^{-1}) were varied by $\sim \pm 20\%$. It can be concluded from J_{sr} diagram that the tracking performance is guaranteed with respect to plant uncertainties with a maximum tracking error of approximately $2 \mu A.m^{-3}$.

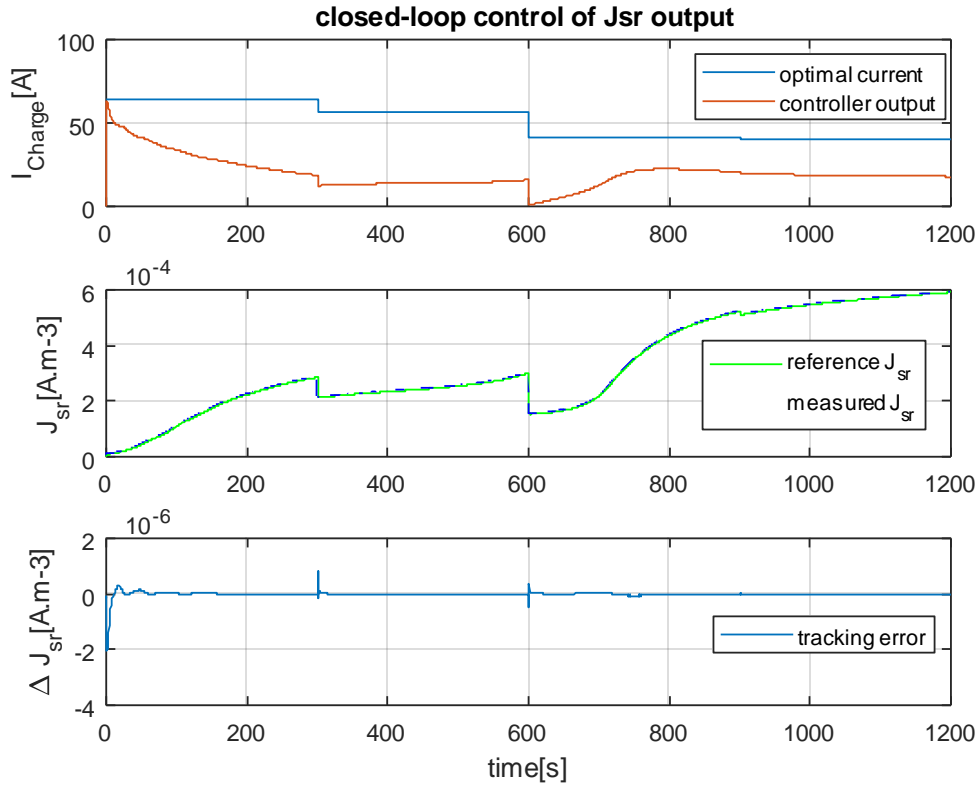


Figure 5-15 Reference tracking in case of parameter variations

Thanks to a robust CRONE feedback loop, the controller provides an enhanced closed-loop performance to track the side reaction current trajectories (corresponding to an optimal charging current) and responding well to slow system dynamics. To the best knowledge of the author, this is the first work proposing a closed-loop control strategy for a health-conscious fast charging based on a thorough electro-thermal aging battery model.

However, using this strategy, reaching the final value SOC is not guaranteed. Therefore in a subsequent step, some modifications to the control strategy are proposed to attain the desired target SOC level. The designed controller in Figure 5-14 is incorporated in an inner loop of a cascade setup, to design a comprehensive controller being able to also achieve the target SOC during charging. The target is achieved by re-scaling the recorded optimal trajectories of charging current and side reaction current profiles against the SOC.

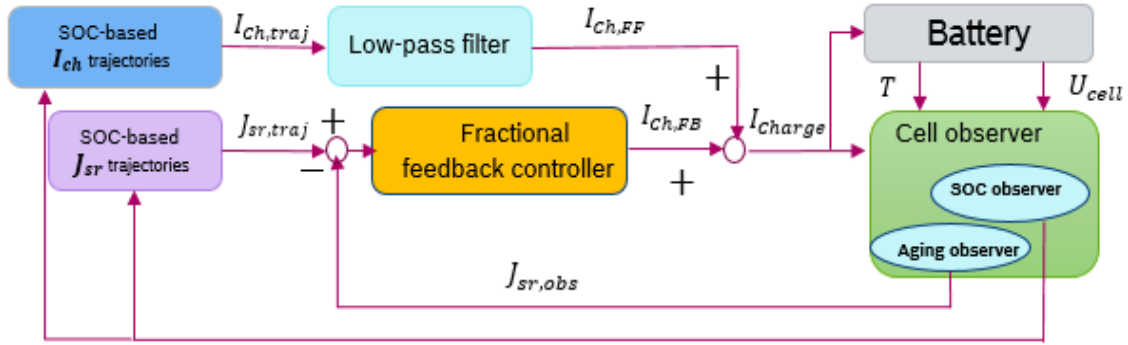


Figure 5-16 Cascade charging controller

The robustness property of the modified control strategy is examined by moderate variation (up to 10%) of some process parameters including initial temperature, electrolyte resistance, and initial thickness of SEI layer. The simulation is performed at 10°C for the cell at its BOL. The results are depicted in Figure 5-17, where the first diagram is representing the comparison between the optimal charging current from the trajectory planning and the current generated by the controller. In this case, the controller output deviates from the optimal current profile in order to keep the track of the optimal side reaction current shown in the second diagram of Figure 5-17 with neglectable tracking error presented in the third diagram. It can be seen that using the modified control loop, target SOC of 80% is reached within the desired charging time of 20 minutes.

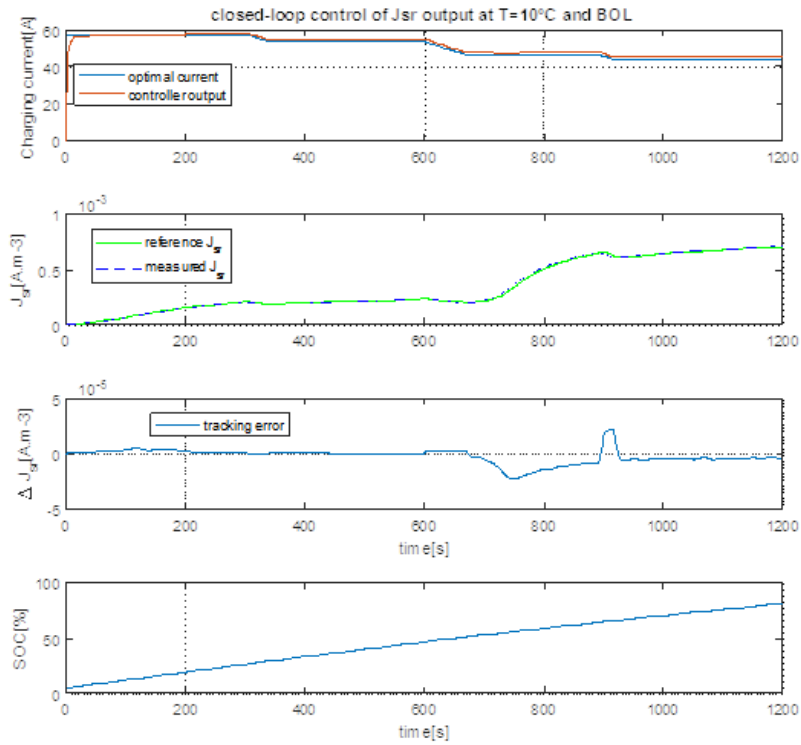


Figure 5-17 Charging in presence of process uncertainties using the cascade controller

5.8 Conclusion and future work

It is demonstrated in this chapter that the dynamic behavior of the battery model varies substantially according to the battery age. This issue needs to be addressed specially during optimal charging of batteries. Thus a cascade feedforward-feedback controller is designed in order to track specific reference trajectories in presence of large parametric uncertainties. Using feedforward technique, the open loop performance is highly improved by acting quickly towards fast dynamics. Thanks to a robust CRONE feedback loop, the controller provides an enhanced closed-loop performance to track the side reaction current trajectories (corresponding to an optimal charging current) and responding well to slow system dynamics. To the author's best knowledge this is the first work proposing a closed-loop control strategy for a health-conscious fast charging based on a thorough electro-thermal aging battery model.

For a future study, a thorough investigation can be performed to identify the best aging criteria in terms of observability. After trajectory planning and based on a sensitivity analysis, this signal can be used as the best candidate for control signal and for design of a charging controller.

In spite of its efficiency, the control loop of figure 5-18 cannot be implemented easily in a car controller. The charging controller indeed requires the computation of the side reaction current and charge current trajectories. In this chapter, they are obtained after the optimization of a charging profile using the method described in section 5.2. However, this optimization problem involves a large number of parameters and requires implementation of a nonlinear optimization routine. Such an approach is really time and resource consuming and prevents any implementation in a car BMS. That is why the next chapter is dedicated to the design of an efficient profile optimization method.

Chapter 6

CHARGING-PROFILE OPTIMIZATION FOR ONBOARD APPLICATIONS

Summary

6.1 Empirical simplification of charging profiles.....	93
6.1.1 Affine profile pattern	94
6.1.2 Polynomial profile pattern	95
6.2 Simplifications in the structure of the battery model.....	97
6.2.2 Simplification of the nonlinear model by Volterra series	102
6.2.2.1 Validation of the Volterra-based model	109
6.3 Simplification in the optimization scheme.....	112
6.4 Conclusion and future work	116

The intelligent charging methodology developed in the previous chapter (see Figure 5-6) requires a reference current that is captured offline using an optimization algorithm described in section 5.2. The optimization algorithm runs the battery model under different conditions iteratively to find the best possible scenario for fast charging. As observed in chapter 5.2, comparably long simulation time of the nonlinear battery model is problematic for implementing the algorithm on a battery control unit.

In order to succeed in achieving an efficient online charging current profile optimization, three types of simplifications can be investigated:

- 1- Simplification in definition of **charging profiles**
- 2- Simplification in the structure of the **battery model**
- 3- Simplification in the **optimization scheme**

In the following sections, some proposals are given to solve this issue in order to reach an easily implementable solution for charging profile optimization.

6.1 Empirical simplification of charging profiles

The goal is to find general patterns for the optimal charging profiles by interpreting the behaviour of the profiles obtained in chapter 5.2. According to this concept, each optimal profile pattern will be characterized by only a few independent parameters comparing to other profiles such as MCC. This simplification by using pre-defined charging profiles leads to reduce the execution time of the optimization and to facilitate an online optimization method.

Decision on the general shape of an optimal profile is based on an investigation on the previous researches done in this field and the observations from trajectory planning results in chapter 5. For the first time, Mas [83] introduced an ideal charging acceptance diagram to minimize the rate of gassing reaction in Lead-Acid batteries. According to his hypothesis, large current is permissible to be applied in the beginning of charging procedure. Charging efficiency maintains very well until start of the unwanted gassing phenomenon. By continuing the charging, mass transport for the reaction triggers the polarization effect. As a result of polarization, battery charging efficiency reduces gradually. When battery voltage reaches the critical voltage of gassing, charging current has to be reduced in order to slow down the unwanted gassing reaction. Thus to keep high efficiency for fast charging, it is recommended to input as much charge as possible before

start of gassing. This means a monotonically decreasing shape for the charging profile. Besides that, by analysing the results obtained from the trajectory planning, it can be observed that the optimal profiles have a strictly decreasing behaviour versus SOC (resp. time).

Another issue with charging profile optimization method used in chapter 5 was with using *fmincon* as the optimizer. The problem with *fmincon* is that, it is not implementable for the real-time application on Electronic Control Units (ECU). Besides that, it is an iterative approach that runs the battery model several times in each iteration which is very resource consuming and computationally intensive. Thus, the optimization method in this case, can be simplified with less optimization parameters and a more efficient algorithm. One idea is to replace *fmincon*, by a user-defined function, implementable on ECU and with less computational effort. This topic will be discussed in more details in section 6.3

According to the mentioned points, two patterns with *affine* shape and *polynomial* shape have been investigated in the following sections. For all the different possible patterns, two conditions hold:

- fixed charging time of t_{ch}
- fixed amount of charge denoted by Q_c is transferred (correlating to a certain *SOC* range)

6.1.1 Affine profile pattern

This kind of profile is specified by initial charging current I_0 (y-axis intersection) and slope α . Taking into account the constraints on a fixed charging time and a given amount of transferred charge (area under the curve), the following relation is deduced:

$$\alpha = \frac{2(I_0 t_{ch} - Q_c)}{t_{ch}^2} . \quad (6-1)$$

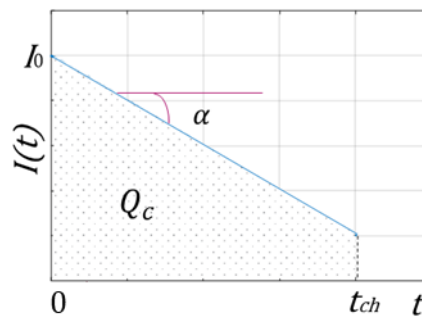


Figure 6-1 Affine-shape profile pattern

It means, searching for an optimal charging profile using affine profile pattern reduces the optimization to search for only one independent parameter α .

6.1.2 Polynomial profile pattern

A Polynomial shape can be a good candidate providing a smooth transition from a semi-constant current phase to a semi-constant voltage phase. Analytical relation for a minimum-degree polynomial is:

$$I(t) = a + bt + ct^2 + dt^3. \quad (6-2)$$

The following constraints hold for a polynomial shape charging profile that can further reduce the complexity of the expression in (6-2):

$$(I) : \quad \left. \frac{dI(t)}{dt} \right|_{t=0} = 0 \rightarrow b = 0 ; \quad (6-3)$$

$$(II) : \quad \left. \frac{dI(t)}{dt} \right|_{t=t_{ch}} = 0 \rightarrow c = -1.5dt_{ch} ; \quad (6-4)$$

$$(III) : \quad \int_0^{t_{ch}} I(t)dt = Q_c \rightarrow a = \frac{Q_c + 0.25 dt_{ch}^4}{t_{ch}} ; \quad (6-5)$$

$$(IV) : \quad 0 \leq a = I_0 \leq 3.5C_{cell} \rightarrow d_{min} \leq d \leq d_{max} . \quad (6-6)$$

Figure 6-2 represents the conceptual profile with polynomial shape with the corresponding boundary conditions specified on the diagram.

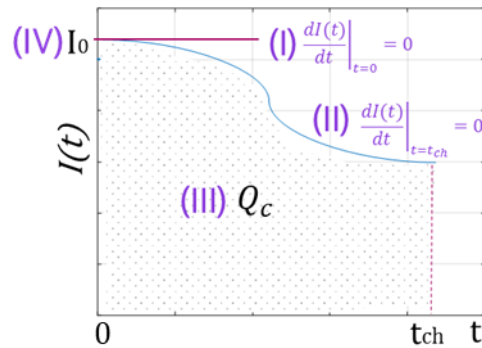


Figure 6-2 Polynomial-shape profile pattern

From the mentioned constraints on the shape of the profile, relation (6-1) is reduced to the following equation, where only one independent parameter d exists. After optimization of

parameter d , parameters c and a can be computed accordingly from (6-4) and (6-5), and relation (6-2) becomes:

$$I(t) = a + ct^2 + dt^3. \quad (6-7)$$

The performance of both affine and polynomial profiles are evaluated in the next section.

6.1.3 Comparison of the simplified profiles with the state of the art profiles

The two empirical profile patterns introduced are obtained at temperature of 35°C to charge a fresh cell from 5 to 80% SOC. The charging profiles are applied to the battery model as the input and corresponding capacity loss, side reaction current, temperature, SOC, and voltage are monitored. Based on the simulation results presented in **Figure 6-3**, the polynomial profile appears to be a promising candidate in reduction of aging in terms of capacity loss and side reaction current comparing to other profiles including CCCV, MSCC and Affine.

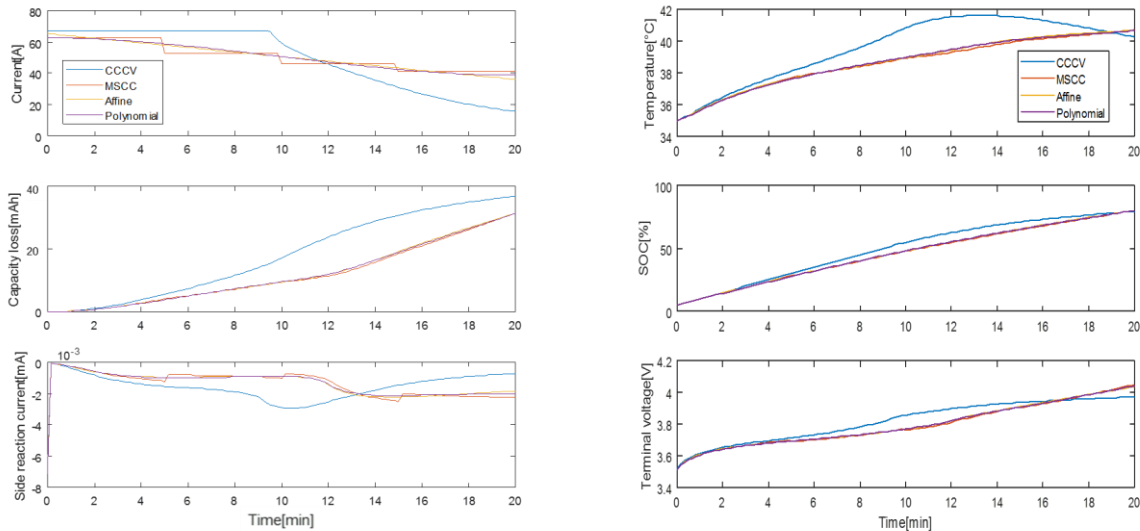


Figure 6-3 Performance comparison of the optimal patterns with state of the art CCCV

All of the different types of the optimal profiles demonstrate a reduction in the capacity loss and consequently less side reaction current. It can be seen that the side reaction current obtained by applying the polynomial profile has the smoothest variation especially rather than MSCC due to abrupt change of current amplitude in each constant current phase. The increase of temperature for the conventional CCCV profile is also greater than of the one using optimal charging profiles. Excessive temperature increase is one of reasons leading to higher capacity loss. Therefore,

polynomial profile is taken as the best pattern with least complexity and best performance for reduction of battery degradation.

6.2 Simplifications in the structure of the battery model

The battery model shown in chapter 4 (Figure 4-13), is a nonlinear model including several feedback loops with high computational effort leading to resource consumption problem. Various techniques can be employed to simplify the nonlinear battery model. Before exploring different possible methods for transformation of the model into a less complicated structure, some simplifications can be regarded in the arrangement of the model in Figure 4-13.

First, the electrode model for the anode and the cathode illustrated in Figure 6-7 is taken into account and the following modifications are proposed to decrease the model simulation time:

- 1- substituting the OCP lookup table (referred as OCP LUT) by its equivalent polynomial function with the method introduced in section 6.3
- 2- suppression of the loop including the side reaction current j_{sr} ;
- 3- linearization of inverse Butler-Volmer sub-system;
- 4- simplification of the thermal sub-system using *Volterra series*

In the following parts, each proposal is explained and validated. The first proposal is already discussed in chapter 3. The second proposal concerns relation (4-6) and is based on two hypotheses:

- the magnitude of side reaction current j_{sr} , is negligible in relation to the magnitude of the intercalation (main reaction) current j_I .
- SEI thickness remains almost constant during a single fast charging cycle

In order to evaluate the truth of these hypotheses, a simulation test has been performed. In this test a current profile (Figure 6-4) is imposed to the model once before cutting the loop including j_{sr} and with a variable SEI thickness, and once after cutting the side reaction loop and with a constant SEI thickness. Subsequently the side reaction (Figure 6-5) and the cell terminal voltage, (

Figure 6-6) for both cases are measured and compared. It can be deduced that cutting the closed-loop (i.e $j_{remain} = j_I$) and assuming a constant SEI layer thickness during one fast

charging cycle has no significant influence on the outputs of the model and is a valid hypothesis that leads to simplicity of the battery model.

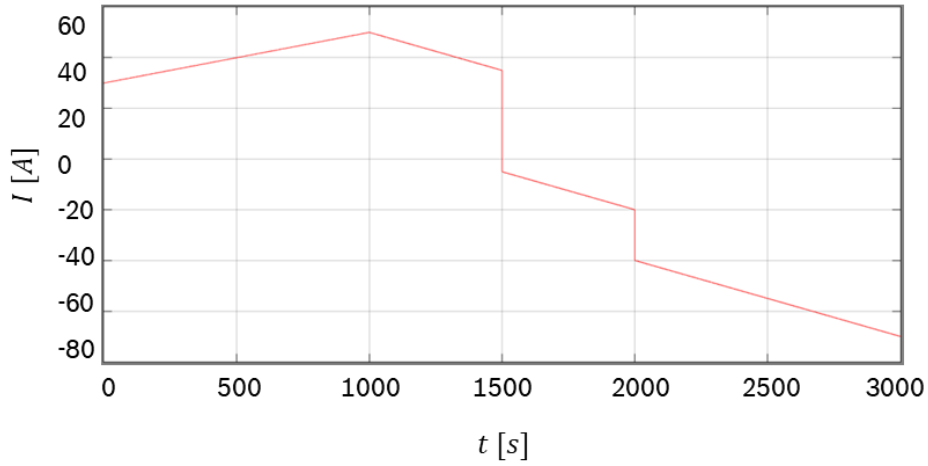


Figure 6-4 Current profile for validation of the second proposal

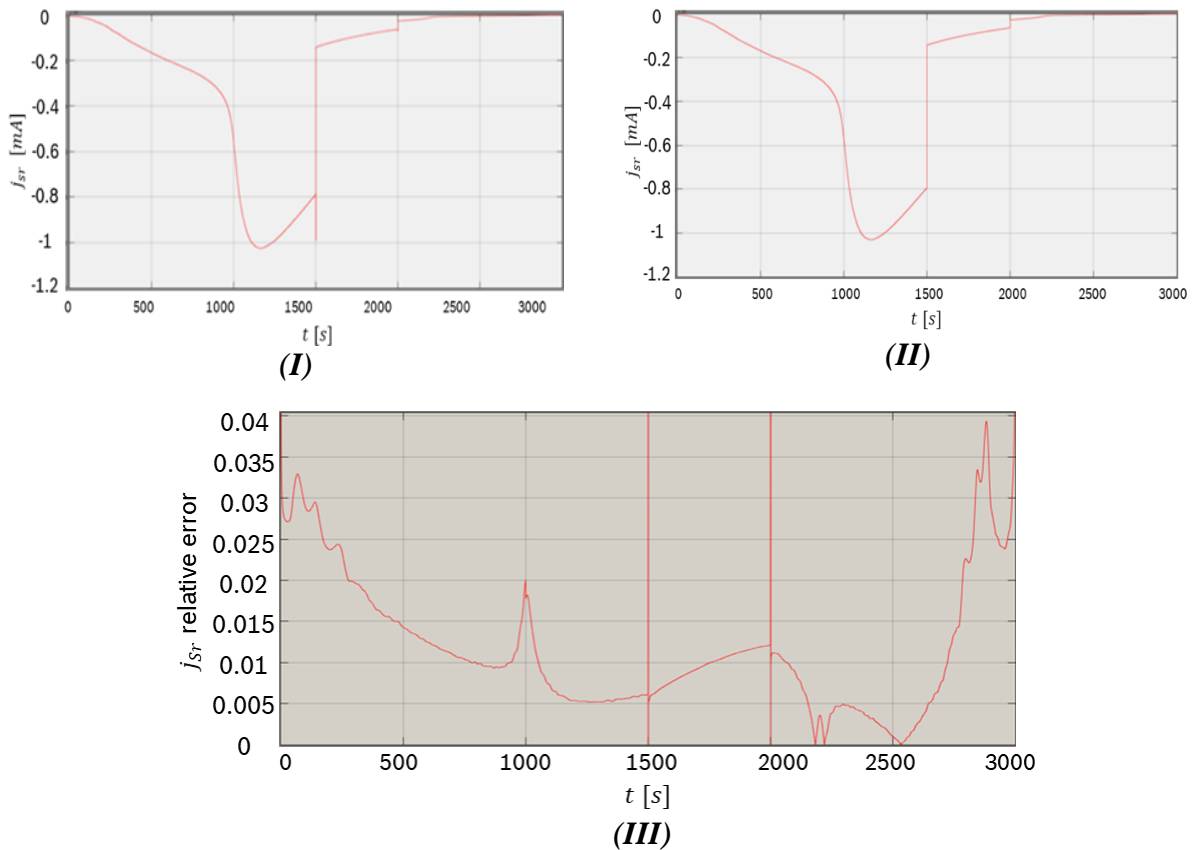


Figure 6-5 Side reaction current **(I)** by assuming a variable SEI thickness **(II)** by assuming a constant SEI thickness and **(III)** relative error of both cases

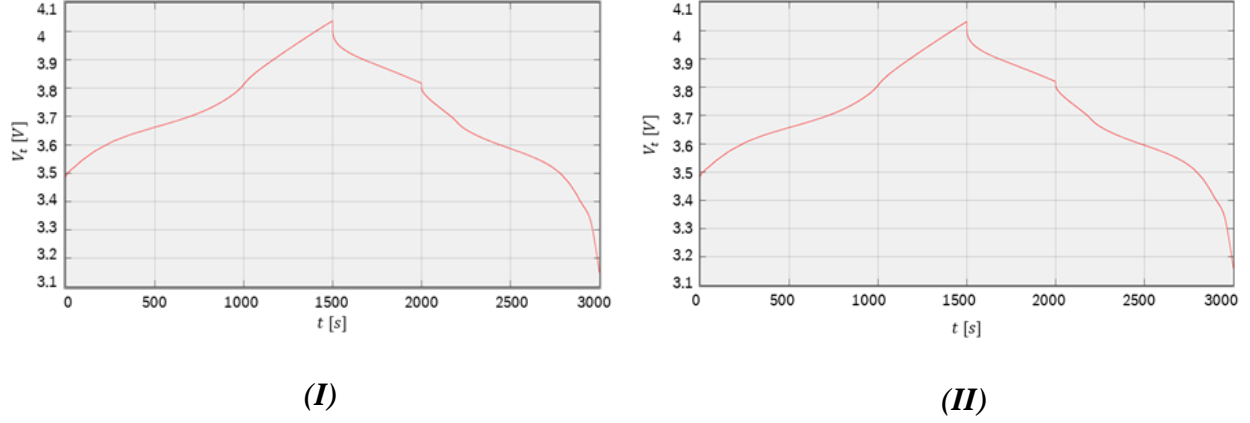


Figure 6-6 Cell terminal voltage **(I)** before and **(II)** after breaking the j_{sr} loop

The third proposal is related to the inverse Butler-Volmer sub-system introduced by relation (3-9). The polarization voltage of the cell U_{pol} , which represents the variation of cell voltage from its steady state value, (also input to the thermal sub-model) is defined by relation (6-8). U_i^{SS} denotes the steady-state electrodes potential (where $i = n$ (anode) or p (cathode)).

$$U_{pol} = \underbrace{(\phi_{sp} - \phi_{ep})}_{U_p + \eta_p} - \underbrace{(\phi_{sn} - \phi_{en})}_{U_n + \eta_n + R_{SEI}I} - (U_p^{SS} - U_n^{SS}). \quad (6-8)$$

By rearranging the above equation, a distinction between the contribution from the Butler-Volmer sub-model V_y and electrode concentration model V_x , is made:

$$U_{pol} = \underbrace{(U_p - U_n - R_{SEI}I - U_p^{SS} + U_n^{SS})}_{V_x} + \underbrace{(\eta_p - \eta_n)}_{V_y}. \quad (6-9)$$

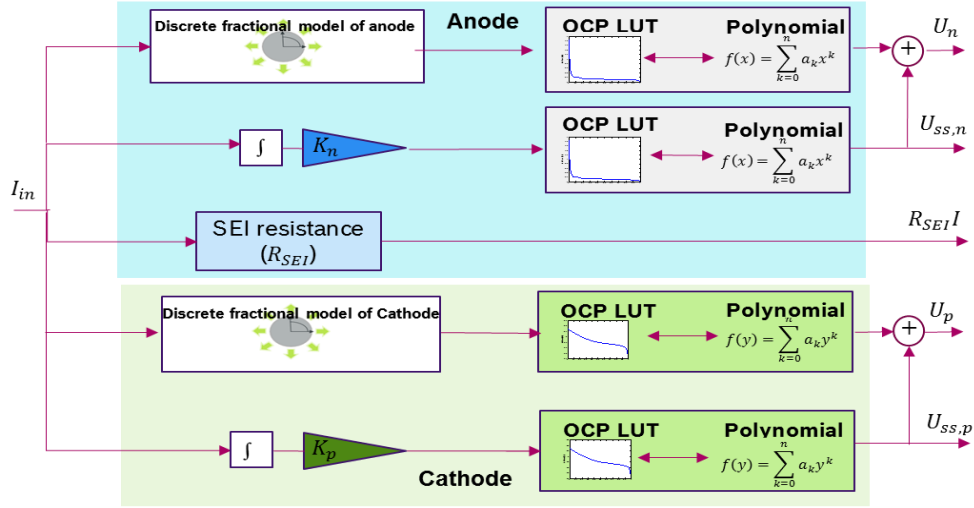


Figure 6-7 Simplified model of the electrodes

By assuming the proposed modifications, the remaining part of the global model in Figure 4-13 which includes the thermal, aging and Butler-Volmer sub-models turns into the model of Figure 6-8.

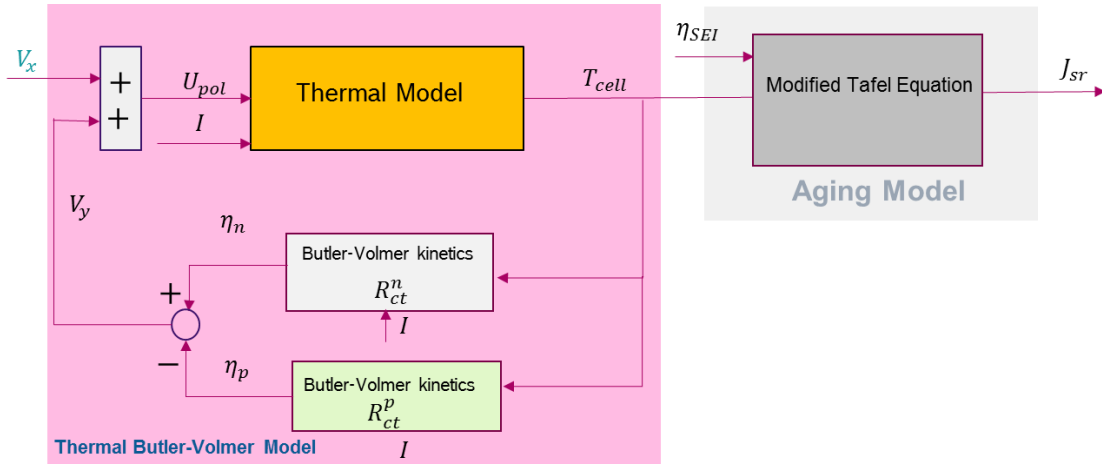


Figure 6-8 Coupled aging-thermal-Butler-Volmer model after simplification

The state-space representation of the Thermal-Butler-Volmer sub-model (denoted by thermal-BV sub-model) is derived. Assuming the temperature T_{cell} as the state-variable, V_x and I as inputs, the nonlinear multiple-input single-output (MISO) ordinary differential equation (ODE) of the system is given by:

$$\dot{T}_{cell} = f(T_{cell}, V_x, I, T_{init}, T_{amb}). \quad (6-10)$$

Thus based on the heat transfer equation (4-1), it expands to:

$$\dot{T}_{cell} = \frac{1}{mC_p} \left(-hA_{tot}(T_{cell} - T_{amb}) + R_f I^2 + V_x I + (\eta_n - \eta_p) I \right) \quad (6-11)$$

At this point, the behaviour of the Butler-Volmer sub-model is investigated by applying a constant current to the model in the range of $0 < I_{ch} \leq 100$ (A) to do a full charge and the respective average anode and cathode overpotential is measured. The results shown on diagrams of figure Figure 6-9, reveal a linear dependency of the electrode overpotential with respect to the input current.

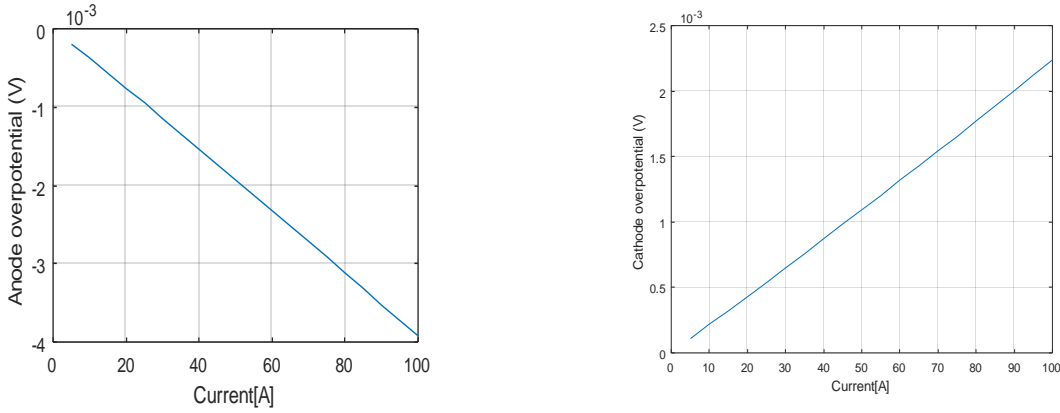


Figure 6-9 Variation of the electrode overpotential against input current in Butler-Volmer sub-model

Therefore the inverse Butler-Volmer function to obtain the electrode overpotential is approximated by a linear relationship, where m_n and m_p are the slopes of the diagrams in Figure 6-9 for anode and cathode respectively. This permits the following simplifications:

$$\begin{aligned} \eta_n &= \frac{RT}{\alpha_n F} \sinh^{-1} \left(\frac{j_n}{2a_s^n i_{0n}} \right) \approx m_n T I \\ \eta_p &= \frac{RT}{\alpha_p F} \sinh^{-1} \left(\frac{j_p}{2a_s^p i_{0p}} \right) \approx m_p T I \end{aligned} \quad (6-12)$$

Incorporating relation (6-19) into (6-18) results in:

$$\dot{T}_{cell} = \frac{1}{mC_p} \left(-hA_{tot}(T_{cell} - T_{amb}) + R_f I^2 + V_x I + m_n T_{cell} I^2 - m_p T_{cell} I^2 \right). \quad (6-13)$$

From (6-13), assuming that $T_{cell} = T_{init} + \delta T_{cell}$, a nonlinear Multi-Input Single-Output (MISO) differential equation is derived where δT_{cell} is the state-variable and four input signals I^2 , $V_x I$, T_{amb} and T_{init} are identified:

$$\delta \dot{T}_{cell} = \frac{1}{mC_p} \left(-hA_{tot}(T_{init} - T_{amb} + \delta T_{cell}) + R_f I^2 + V_x I + m_n(T_{init} + \delta T_{cell})I^2 - m_p(T_{init} + \delta T_{cell})I^2 \right) \quad (6-14)$$

The whole thermal-BV sub-model thus is summarized by the block diagram of **Figure 6-10**:

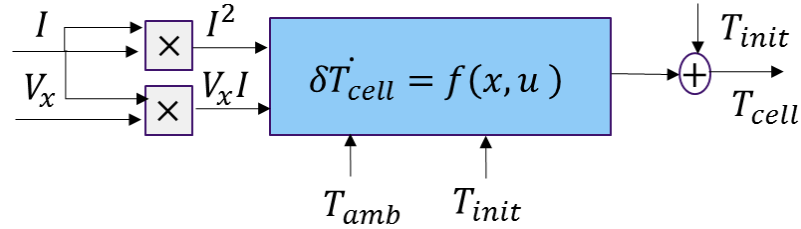


Figure 6-10 Input-Output System representation of coupled thermal-BV sub-model

This sub-model incorporates a nonlinear MISO equation with plenty of parameters. Thus after the simplifications proposed by the first three hypotheses, this sub-model would be the main source of nonlinearity and computationally expensive. Based on this conclusion, thermal sub-model is the focus of the next section to be transformed to a less complicated structure using Volterra series approximation. Volterra series permit an implementation with only linear systems (whose output are combined with multiplication) that are thus easy to discretize and realizable with low level of complexity. Besides that it reduces the simulation and optimisation time of the model.

6.2.2 Simplification of the nonlinear thermal model by Volterra series

Volterra series are recently widely used for representation of input-output relationship of nonlinear dynamical systems. The concept was firstly introduced by Vito Volterra in 1887 [85] but due to high computational complexity of the method it was only extensively employed until 1990s, at the same time with advancement of computer and software technology. It is known as a good tool for modeling and analyzing the nonlinear systems. Use of Volterra series for representation of dynamical systems covers a wide range of application in several fields of engineering and physics. In field of mechanical engineering, it has been employed for systems modeling and identification, system design and fault diagnosis [86, 87]. It has a widespread application in electronic and

electrical engineering for instance in nonlinear distortion analysis, speech modeling and image processing [88, 89]. The application in control engineering is also of great interest, especially for accurate consideration of nonlinear factors in modelling of observers or controllers. There has been also an application of Volterra series for control of electrochemical storage systems. A study by Gruber where Volterra series are used for design of a nonlinear model predictive controller to adjust the airflow in a fuel cell [90].

Volterra Series are of a similar character as Taylor series but with advantage of considering memory effects. In addition to Volterra series, there exist a variety of mathematical tools for description and handling of nonlinear dynamic systems such as *Taylor series*, *Wiener series*, *Hammerstein model*, etc. For example *Taylor series* is a common method for representing nonlinear systems, where the output of the system depends on the input at a particular time. *Wiener series* which is the orthogonal expansion of functional series for nonlinear-time invariant systems, is developed to deal with the strict convergence region of Volterra series. The main issue with this method is difficult identification of kernel functions. *Hammerstein model* is used for a specific case of a static nonlinear system followed by a linear dynamic system [91]. The main advantage of using Volterra series is in its generality that enables displaying the intrinsic characteristics of a nonlinear system in a rather simple and convenient way.

The principal of the method lies in extension of standard convolution of linear systems to nonlinear systems. According to this method, $y_n(t)$ the n -th order output of the system with $u(t)$ as the input, can be represented by multi-dimensional convolution of n -th order Volterra kernel h_n (comparable to impulse response for a linear system with $n=1$), given by:

$$y_n(t) = \int_{-\infty}^{+\infty} \dots \int_{-\infty}^{+\infty} h_n(\tau_1, \dots, \tau_n) \prod_{i=1}^n u(t - \tau_i) d\tau_i \quad (6-15)$$

The identification of Volterra kernel function can be done whether in time domain or frequency domain. Multi-dimensional Fourier transform of Volterra kernel function is called the Generalized Frequency Response Function (GFRF). In this work, the frequency domain identification is performed using harmonic probing or exponential input method proposed by Peyton Jones and Billings [92]. Based on this approach, input is a periodic multi-frequency excitation consisting of the sum of n exponentials presented by:

$$u(t) = \sum_{r=1}^n \exp(s_r t). \quad (6-16)$$

The system output $y(t)$, can be expressed as a Volterra functional polynomial of the input $u(t)$ (where \bar{N} denotes the maximum order of the system nonlinearity):

$$y(t) = \sum_{n=1}^{\bar{N}} y_n(t) = y_1(t) + y_2(t) + \dots \quad (6-17)$$

A recursive algorithm is introduced in this study, to compute the n th-order frequency response function of a nonlinear model described by a nonlinear differential equation. The method involves essentially in derivation of system's respective GFRFs under harmonic excitation. The GFRF of n -th order leads to the following relation for n -th order kernel:

$$H_n(s_1, \dots, s_n) = \int_{-\infty}^{+\infty} \dots \int_{-\infty}^{+\infty} h_n(\tau_1, \dots, \tau_n) \exp(-(s_1 \tau_1 + \dots + s_n \tau_n)) d\tau_1 \dots d\tau_n. \quad (6-18)$$

Thus the n -th order Volterra transfer function for a nonlinear system with exponential input covering the frequency spectrum up to ω_r is obtained by:

$$H_n(s_1, \dots, s_n) = \frac{1}{n!} \times [\text{coefficients of } \exp((s_1 + \dots + s_n)t) \text{ in } y(t; \theta, \omega_r)]. \quad (6-19)$$

The term in the brackets states to extract the coefficients of the exponential functions having non-repetitive combinations of frequencies $\{\omega_1, \dots, \omega_r\}$ the n th harmonics for n th order kernel.

For the thermal nonlinear model, as the first step towards computing the Volterra kernels, the governing nonlinear differential equation of the coupled Thermal-BV sub-system is rewritten. Referring to the simplifications proposed in section 6.2 the original differential equation is given by relation (6-14). Four inputs, u_1 , u_2 , u_3 , and u_4 and one output, δT_{cell} (temperature gradient) are identified for the nonlinear system, with:

$$\begin{cases} u_1(t) = I^2(t) \\ u_2(t) = V_x(t)I(t) \\ u_3(t) = T_{amb}(t) \\ u_4(t) = T_{init} \end{cases} \quad (6-20)$$

Renaming the coefficients by:

$$a = -\frac{hA_{tot}}{mC_p}, b = \frac{m_n - m_p}{mC_p}, c = -\frac{R_f}{mC_p}, d = \frac{m_n - m_p}{mC_p}, e = -\frac{1}{mC_p}, f = -\frac{hA_{tot}}{mC_p}, g = \frac{hA_{tot}}{mC_p} \quad (6-21)$$

and by dropping the time-dependency notation of the signals, relation (6-19) changes to a compact standard form of:

$$\delta \dot{T}_{cell} = -a\delta T_{cell} - b\delta T_{cell}u_1 - cu_1 - eu_2 - gu_4 - du_4u_1 - fu_3. \quad (6-22)$$

For each kernel, the input is sum of exponentials up to kernel's order. Thus the first kernel, which is indeed the Fourier transform of the linear part of the nonlinear system and therefore identical to a linear transfer function, is calculated by defining the input signals as:

$$\begin{cases} u_1(t) = r_1 \exp(s_1 t) \\ u_2(t) = r_2 \exp(s_1 t) \\ u_3(t) = r_3 \exp(s_1 t) \\ u_4(t) = r_4 \exp(s_1 t) \end{cases} \quad (6-23)$$

The resulting output signal $y(t)$ (temperature gradient) is then supposed given by :

$$y_1(t) = H_1(s_1)\exp(s_1 t). \quad (6-24)$$

Subsequently, the defined signals are replaced in equation (6-22) and by collecting the coefficients of the terms including $\exp(s_1 t)$, following expression is obtained for first kernel:

$$H_1(s_1) = \frac{-er_2 - fr_3 - gr_4}{a + s_1}. \quad (6-25)$$

The result shows traces of inputs u_2 , u_3 , and u_4 yield in the formation of the first-order kernel. **Figure 6-11** represents the corresponding block diagram of first-order kernel, where the contribution of u_4 is in initialization of the integral block.

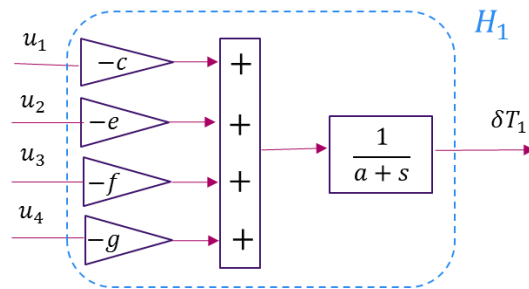


Figure 6-11 Block diagram of the first order Volterra kernel

For calculation of the second order kernel, a more general periodic excitation composed of two harmonics is imposed shown by:

$$\begin{cases} u_1(t) = r_1 \exp(s_1 t) + r_1 \exp(s_2 t) \\ u_2(t) = r_2 \exp(s_1 t) + r_2 \exp(s_2 t) \\ u_3(t) = r_3 \exp(s_1 t) + r_3 \exp(s_2 t) \\ u_4(t) = r_4 \exp(s_1 t) + r_4 \exp(s_2 t) \end{cases} \quad (6-26)$$

Substituting the input signals in relation (6-15), yields the following expression for the output:

$$y_2(t) = H_1(s_1) \exp(s_1 t) + H_1(s_2) \exp(s_2 t) + H_2(s_1, s_1) \exp(2s_1 t) + 2H_2(s_1, s_2) \exp(s_1 t) \exp(s_2 t) + H_2(s_2, s_2) \exp(2s_2 t). \quad (6-27)$$

The same procedure is employed to obtain the relation for the second order kernel. Extracting the coefficients of the terms with two harmonics $\exp(s_1 t) \times \exp(s_2 t)$ leads to:

$$H_2(s_1, s_2) = -\frac{1}{2} \frac{r_1 (bH_1(s_1) + bH_1(s_2) + 2dr_4)}{a + s_1 + s_2}. \quad (6-28)$$

In order to implement its block diagram, firstly the obtained formula for the second kernel is decomposed to lower degree components based on Volterra realization theory [93]. As (6-28) can be rewritten by:

$$H_2(s_1, s_2) = \left(-\frac{b}{2}\right) \times H_1(s_1) \times 1 \times \frac{1}{a + s_1 + s_2} \times r_1 + \left(-\frac{b}{2}\right) \times 1 \times H_1(s_2) \times \frac{1}{a + s_1 + s_2} \times r_1 + (-d) \times 1 \times 1 \times \frac{1}{a + s_1 + s_2} \times r_1 \times r_4 \quad (6-29)$$

The corresponding block diagram is presented by **Figure 6-12** (assuming: $G(s) = \frac{1}{a+s}$).

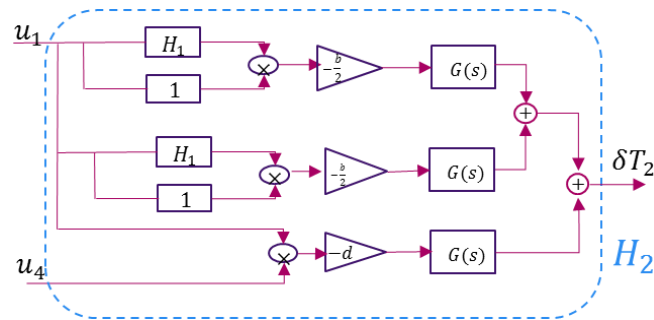


Figure 6-12 Block diagram of the second order Volterra kernel

Due to the symmetry observed in the two upper branches, the block diagram of **Figure 6-12** is further simplified (**Figure 6-13**).

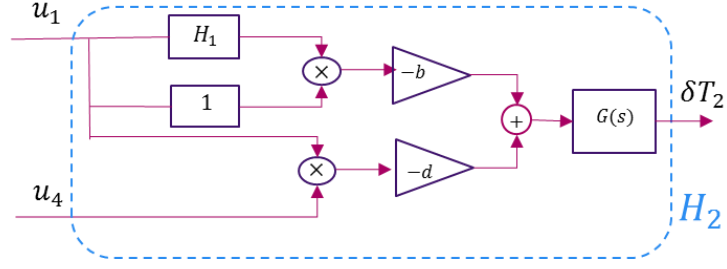


Figure 6-13 Simplified block diagram of the second order Volterra kernel

The calculation of Volterra kernel is done for the third kernel as well. For the third order kernel calculation, a periodic input composed of three harmonics is used for perturbation of system:

$$\begin{cases} u_1(t) = r_1 \exp(s_1 t) + r_1 \exp(s_2 t) + r_1 \exp(s_3 t) \\ u_2(t) = r_2 \exp(s_1 t) + r_2 \exp(s_2 t) + r_2 \exp(s_3 t) \\ u_3(t) = r_3 \exp(s_1 t) + r_3 \exp(s_2 t) + r_3 \exp(s_3 t) \\ u_4(t) = r_4 \exp(s_1 t) + r_4 \exp(s_2 t) + r_4 \exp(s_3 t) \end{cases} \quad (6-30)$$

The corresponding output is then given by:

$$\begin{aligned} y_3(t) = & H_1(s_1) \exp(s_1 t) + H_1(s_2) \exp(s_2 t) + H_1(s_3) \exp(s_3 t) \\ & + H_2(s_1, s_1) \exp(2s_1 t) \\ & + 2H_2(s_1, s_2) \exp(s_1 t) \exp(s_2 t) + H_2(s_2, s_2) \exp(2s_2 t) \\ & + 2H_2(s_1, s_3) \exp(s_1 t) \exp(s_3 t) \\ & + H_2(s_3, s_3) \exp(2s_3 t) + 2H_2(s_2, s_3) \exp(s_2 t) \exp(s_3 t) \\ & + H_3(s_1, s_1, s_1) \exp(3s_1 t) + 3H_3(s_1, s_1, s_2) \exp(2s_1 t) \exp(s_2 t) \\ & + 3H_3(s_1, s_2, s_3) \exp(2s_1 t) \exp(s_3 t) \\ & + 3H_3(s_1, s_2, s_2) \exp(s_1 t) \exp(2s_2 t) \\ & + 6H_3(s_1, s_2, s_3) \exp(s_1 t) \exp(s_2 t) \exp(s_3 t) \\ & + 3H_3(s_1, s_3, s_3) \exp(s_1 t) \exp(2s_3 t) + H_3(s_2, s_2, s_2) \exp(3s_2 t) \\ & + 3H_3(s_2, s_2, s_3) \exp(2s_2 t) \exp(s_3 t) \\ & + 3H_3(s_2, s_3, s_3) \exp(s_2 t) \exp(2s_3 t) + H_3(s_3, s_3, s_3) \exp(3s_3 t) \end{aligned} \quad (6-31)$$

Thus the third order kernel is:

$$H_3(s_1, s_2, s_3) = -\frac{b r_1 (H_2(s_2, s_3) + H_2(s_1, s_3) + H_2(s_1, s_2))}{3(a + s_1 + s_2 + s_3)} \quad (6-32)$$

The simplified form of the kernel function split into lower degree kernels is given by:

$$\begin{aligned} H_3(s_1, s_2, s_3) = & \frac{b}{3} (H_2(s_1, s_2) \times 1) \frac{1}{a + s_1 + s_2 + s_3} \times r_1 + \frac{b}{3} (H_2(s_2, s_3) \times \\ & 1) \frac{1}{a + s_1 + s_2 + s_3} \times r_1 + \frac{b}{3} (H_2(s_1, s_3) \times 1) \frac{1}{a + s_1 + s_2 + s_3} \times r_1. \end{aligned} \quad (6-33)$$

The respective block diagram is shown by **Figure 6-14**.

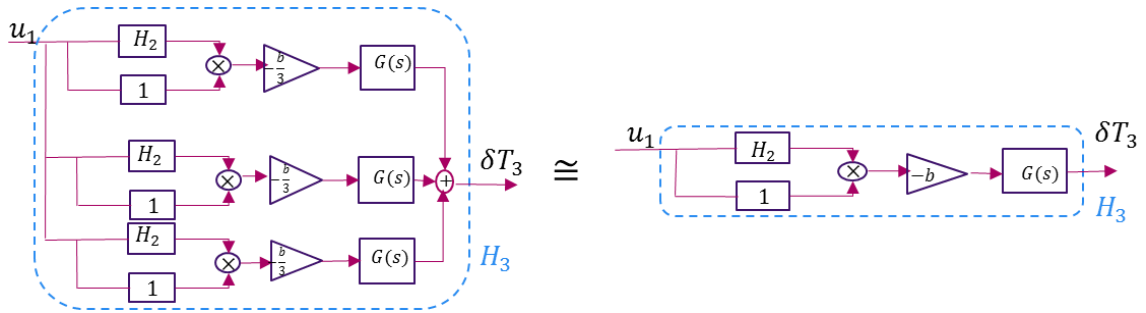


Figure 6-14 Simplified block diagram of the third order Volterra kernel

At this stage, the overall output of the system, temperature gradient δT can be reconstructed from the Volterra system components: $H_1(s_1)$, $H_2(s_1, s_2)$, and $H_3(s_1, s_2, s_3)$ represented in **Figure 6-15**. The underlying system components in Volterra approximated system is illustrated in **Figure 6-16** with aim of reducing the computational complexity.

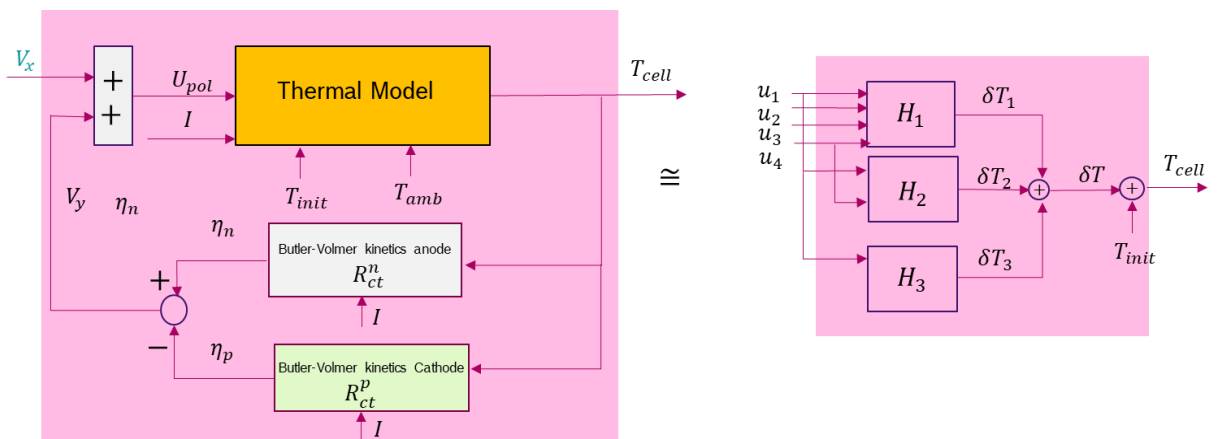


Figure 6-15 Replacing the Thermal-BV sub-system by its Volterra approximated equivalent

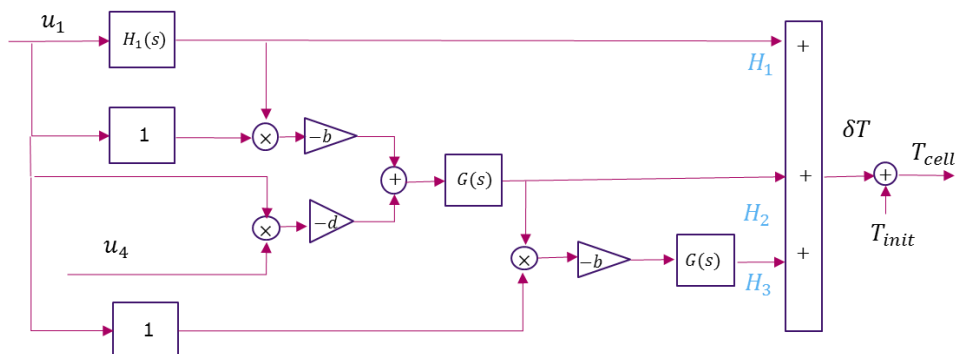


Figure 6-16 Interconnection of the elementary blocks with a simpler structure

Figure 6-17 depicts the magnitude Bode plots of the Volterra kernels. It is observable from the diagrams that the magnitude of the kernel decreases with the order. The steady-state gain of 5

dB, -130 dB, and -120 dB (for the case with $\omega_3 = 0 \frac{rad}{s}$) are obtained for the first, second and third kernel respectively. Thus under steady-state conditions, the contribution of each kernel for a charging current with amplitude of I_{ch} drastically reduces.

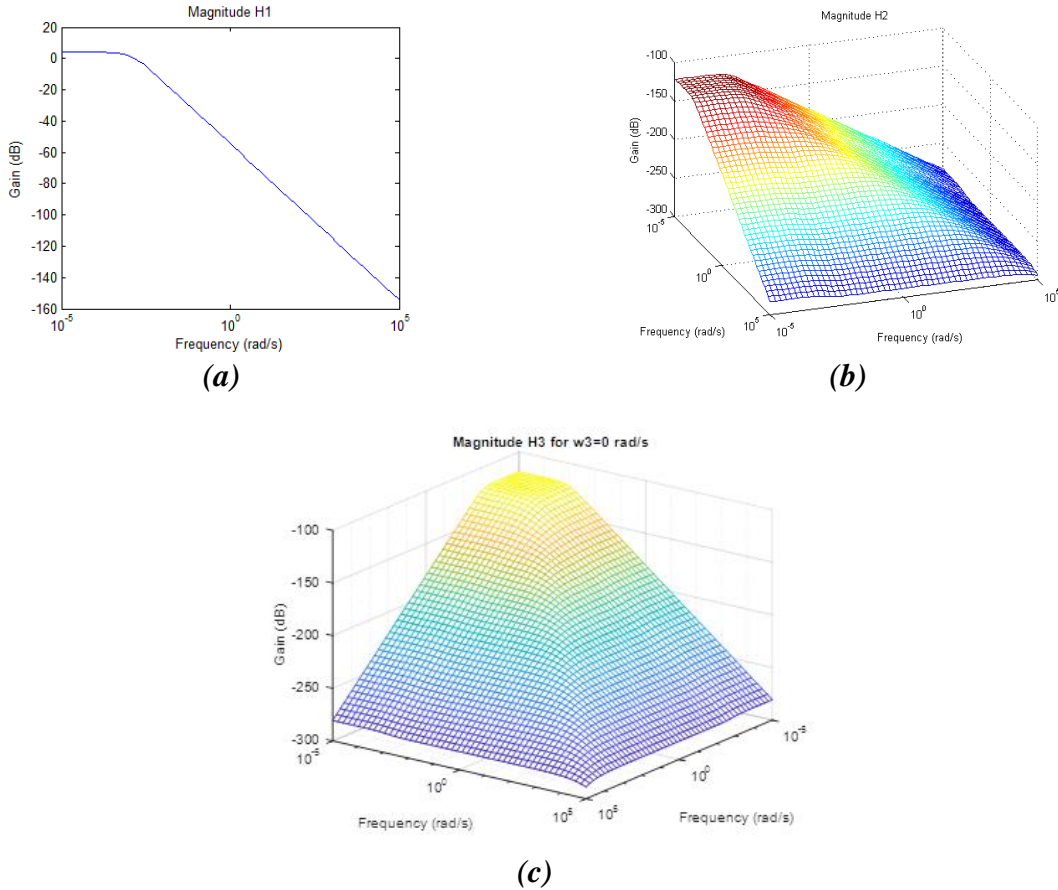


Figure 6-17 Magnitude Bode plot of the Volterra kernels: (a) first kernel magnitude plot, (b) second order kernel magnitude plot third order kernel magnitude plot at frequencies of (c) $\omega_3 = 0 \frac{rad}{s}$

6.2.2.1 Validation of the Volterra-based model

In this section, the ability of the Volterra-based model in simulation of aging phenomenon is examined which is of main interest for online charging optimization. For this purpose, various test conditions are considered to cover a big operating range of the cell. As already discussed in chapter 4, temperature and SOC range are identified as highly influencing factors on battery aging. Thus validation tests conditions employed are summarized in table Table 6-1:

SOC (%) \ T (°C)	5-80	10-85	15-90	20-95
0	1	2	3	4
10	5	6	7	8
25	9	10	11	12
35	13	14	15	16

Experiment number

Table 6-1 Test specifications for validation of Volterra-based model

According to these test specifications, model-based optimization using the polynomial profile pattern explained in section (6.1.2) is carried on both original nonlinear model and the simplified Volterra-based model. The optimal profile obtained by each optimization is imposed to the original nonlinear model, and the respective aging in terms of capacity loss (the value of optimization cost function) is measured and presented on a diagram against the experiment number in Figure 6-18.

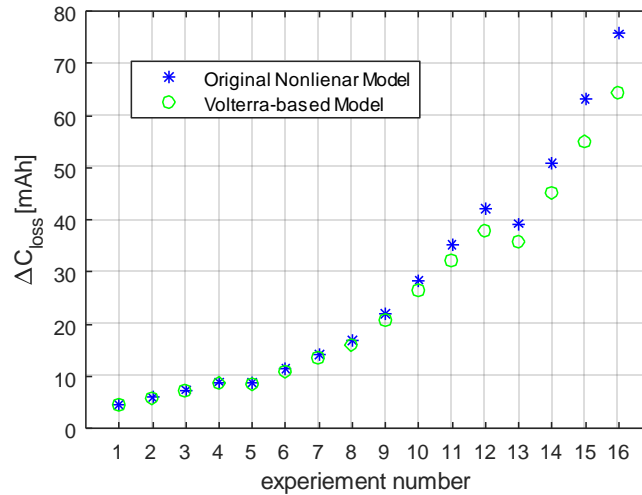


Figure 6-18 Comparison of Nonlinear model and Volterra-based model in aging estimation

The results show that the aging estimated by the optimal profile using Volterra-based model matches well the aging predicted by imposing the current profile obtained from optimization of original nonlinear model. The deviation in aging estimation is more noticeable by charging at larger SOC ranges, where the Volterra-based model underestimates the capacity loss comparing to the nonlinear model. The reason is that the nonlinear nature of the battery appears strongly at extremely

low and high SOC levels, due to larger gradient of Li-ions at the electrode/electrolyte interface [47].

An example of the performed experiments is shown in Figure 6-16. Optimization with interior-point algorithm is performed at temperature of 0°C and SOC range of 10-85% (experiment number 2) once based on the nonlinear model and once with respect to the Volterra-based model (left diagram). Due to simpler structure of the Volterra-based model, optimization algorithm converges to the minimum faster and with less iterations. The simulation time for each optimization, is also given in the table. Using the Volterra-based model the time needed for the model-based optimization is reduced by 37%. The optimal current profiles for each model obtained from the optimization are presented on the right diagram in Figure 6-16.

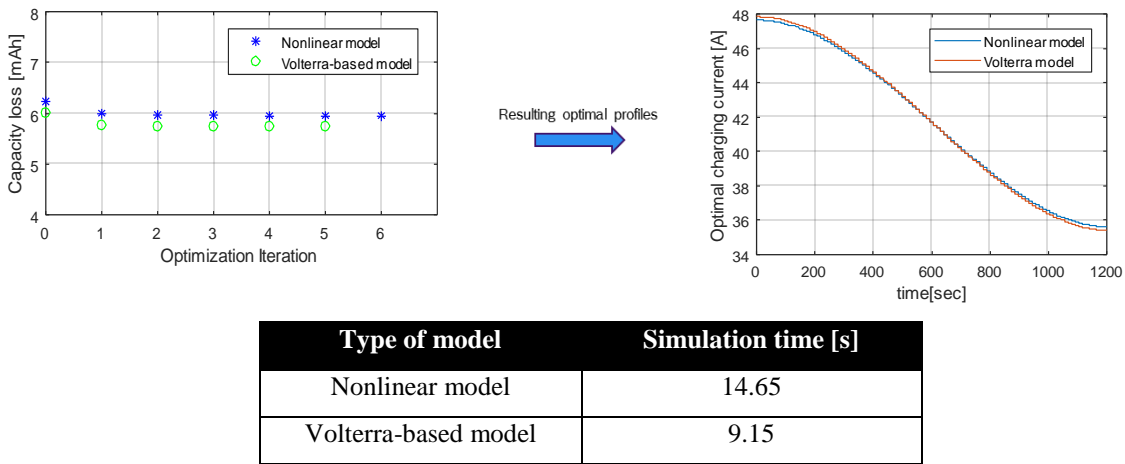


Figure 6-19 Optimization cost function against iteration number

In a subsequent step, the optimal profiles are imposed to the original nonlinear model to estimate the capacity loss and the temperature rise and respective estimation error shown in Figure 6-20. Since the thermal sub-model in the original nonlinear model is partly replaced by Volterra-based sub-model, it is of great interest for the application of intelligent charging, to evaluate its accuracy in estimation of temperature and the corresponding capacity loss. The relative error of maximum 0.18% in capacity loss estimation and 0.28% in temperature estimation confirm the high precision of the model simplified by Volterra series.

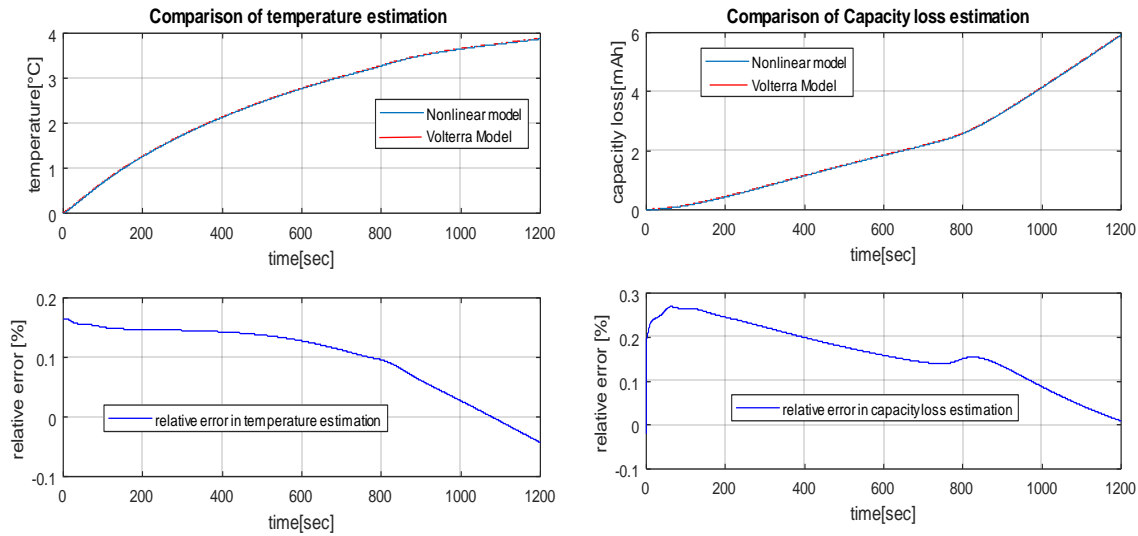


Figure 6-20 Optimization results and respective aging estimated by the nonlinear model

At this step, the validated Volterra-based model can be used to further simplify the online charging optimization by designing a less complex user-defined optimization algorithm, which is the topic of the next section.

6.3 Simplification in the optimization scheme

The ultimate objective of this study is to propose an online charging optimization methodology to be integrated on real-time Electronic Control Units (ECUs). *fmincon*, the built-in function of Matlab for optimization, is not appropriate for this purpose, since the transformation to an executable script is very resource consuming. Furthermore, the optimization options cannot be easily tuned according to scaling of the optimization problem. Thus the solution lies in developing a simplified user-defined optimizer that replaces the time-consuming iterative dynamic optimization and facilitates easy tuning of constraints and optimization options by the user.

Various optimization techniques can be used for this aim. In general, optimization methods can be classified based on the order of the cost function derivative used for the direction of search method to: 0th–order, 1st-order, and 2nd–order optimizers.

0th–order optimizer or direct-search method, relies only on evaluation of the cost function value for searching the optimum. This includes a few methods such as dichotomous and black box search. Dichotomous optimization involves in dividing the search space into four regions and computing the cost function values at each point, then comparing the values in each iteration and

eliminating the part of the interval with larger cost function value, until reaching the minimum point. The disadvantages of this method is its slow convergence speed. Furthermore, the cost function should be always continues with sign change in the optimization interval.

1st- order methods also referred as gradient-based methods, use derivative information (1st derivative of the cost function) to guide the search process of the minimum point. With this additional information, the convergence of the search algorithm can be significantly enhanced.

2nd-order optimization techniques use additional information on the curvature of the cost function by calculating the 2nd derivative (or 2nd order Taylor expansion) of the cost function also referred as Hessian. This method is only applicable in case of existing a positive definite Hessian throughout the whole search space [94].

In order to decide about the best technique, a sensitivity analysis on the behavior of the cost function against the optimization variable is conducted. In this analysis, the polynomial pattern introduced in section 6.1.2 that requires only one parameter to optimize is used. It involves in the representation of the cost function C_{loss} as a function of the parameter to tune (parameter d). The analysis is repeated for several test conditions represented in Table 6-2.

According to the diagrams Table 6-2, the objective function is continuous and unimodal in the given interval for optimization of parameter d . Having a single-variable optimization problem and a monotonic gradient function, a combination of dichotomous and gradient descent approach is employed for online charging profile optimization. It means that the 1st order derivative (gradient) of the cost function is included in the dichotomous optimization algorithm. **Figure 6-21** clarifies the concept for a unimodal cost function over interval of $[d_{min}, d_{max}]$.

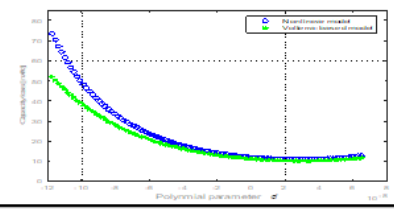
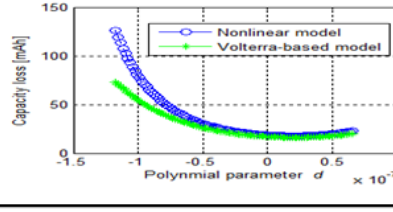
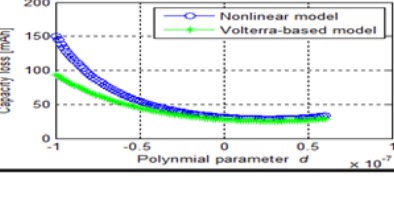
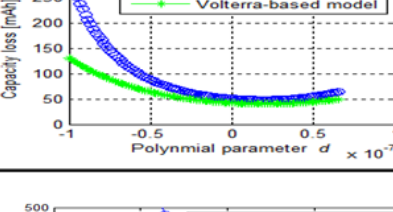
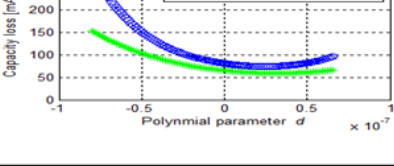
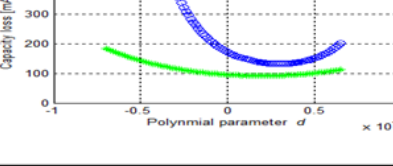
SOC		5-80%		20-95%	
T					
0 °C	Capacity loss [mAh]				
					
					

Table 6-2 Sensitivity analysis of cost function C_{loss} versus optimization parameter d

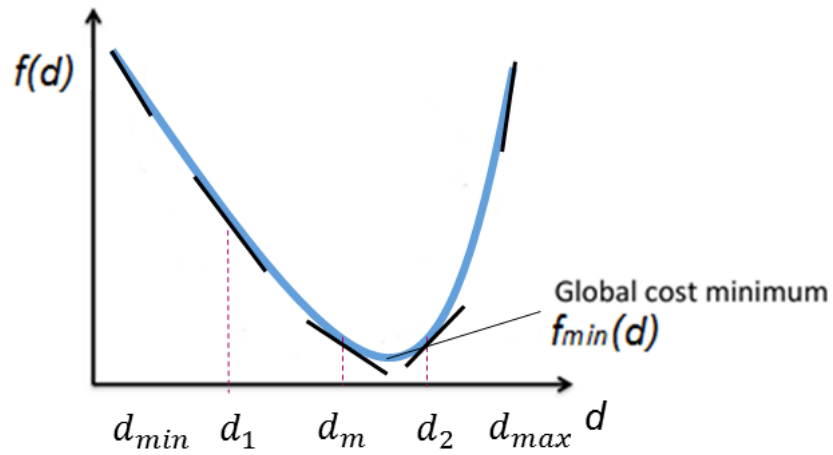


Figure 6-21 Gradient-based dichotomous optimization

The gradient-based Dichotomous approach can be implemented by using the following procedure:

- 1- Start by computing lower bound and upper bound values of d , from the boundary conditions in equation (6-6)
 - 2- Set a value for cost function tolerance $TolFun$ according to scaling of the optimization problem.
- >> Iteration starts
- 3- Calculation of the middle point $d_{mean} = \frac{lb + ub}{2}$
 - 4- Gradient computation at d_{mean} by using forward difference approximation:

$$\hat{f}(d) = \frac{f(d + h \cdot e) - f(d)}{h}$$
 where h is a small step size value depending on the scale of optimization variable and e is an arbitrary unit vector in the parameter space.
 - 5- Computing the termination criterion:

$$LF = |\hat{f}(lb) - \hat{f}(ub)|$$
- >> Checking whether the termination criterion is reached:
- 6- This procedure continue until a point, where the difference between the gradient of lower and upper bound reaches the pre-determined value of $TolFun$ ($LF < TolFun$).
 - 7- Optimal result is the middle point of the last sub-interval: $d_{opt} = \frac{lb + ub}{2}$

The gradient-based dichotomous method was employed to minimize the capacity loss for the same experiments explained in **Table 6-1**. By having a pre-knowledge about the problem and variables scale and relaxing the tolerances, promising results are obtained. The obtained results are compared with the results using *fmincon* optimizer on diagram in Figure 6-22.

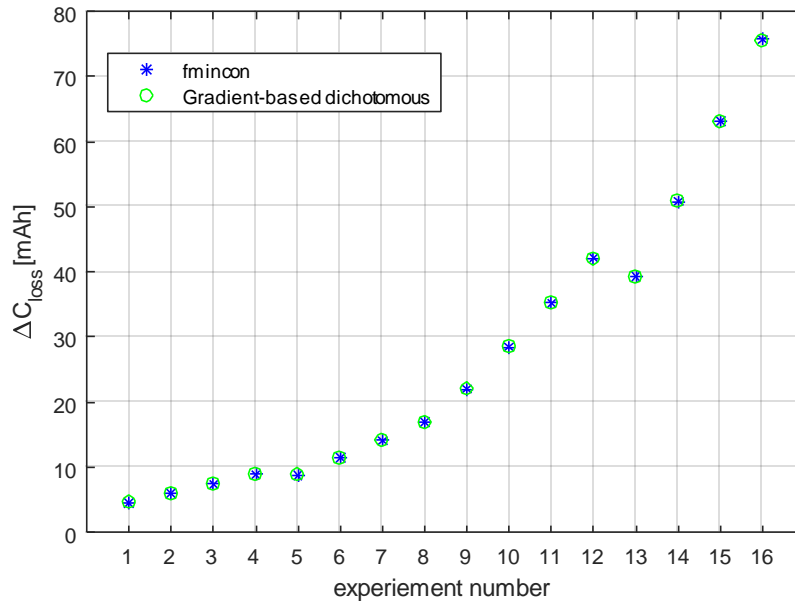


Figure 6-22 Comparison of Matlab *fmincon* optimizer with self-written gradient-based dichotomous optimization method in minimization of capacity loss

6.4 Conclusion and future work

The requirement to have a battery model realizable under real-time conditions, led to propose possible simplifications for the whole intelligent charging process. The simplifications were investigated firstly in the definition of charging profile patterns, then in the second part, in the structure of the nonlinear battery model, and finally in the optimization method.

Based on empirical observations two types of charging patterns were identified: Affine profile and Polynomial profile. These profiles could reduce the initial multi-variable optimization to a single-variable optimization, which can greatly improve the speed of online fast charging.

In the next section, Volterra series were introduced for further simplification of the battery model. Volterra series provide an interesting alternative in the modelling by replacement of resource consuming nonlinear functions in the coupled thermal Butler-Volmer sub-model. Using this approach the simulation executed faster as it can be concluded from Figure 6-19.

Last analysis on the cost function of the optimization problem (capacity loss) is conducted to evaluate its behaviour against the optimization variable. The continuous unimodal cost function in the optimization interval provides the possibility to design a straight-forward optimization scheme. The new method is an attractive alternative to the well-known *fmincon*, comprising a gradient-

based search and dichotomous algorithm to guide the minimum point search direction very fast and with easy user-adjustable optimization options.

All the concepts introduced in this chapter are presented in *Figure 6-23* that shows the closed-loop framework of on-board charging profile optimization. By using a Volterra-based battery model aging in terms of capacity loss can be estimated and that is the criterion for the gradient-based dichotomous optimizer to adapt the shape of the polynomial charging profile to be applied to the cell to reduce aging during charging.

Further studies can be conducted using other modelling frameworks such as multiple model approach. The main principle lies in decomposition of the nonlinear model operating regime into finite number of zones, where the nonlinear model can be approximated locally by an equivalent linear model. . During charge and for instance in order to take into account some modelling errors, it should also be interesting to make an online optimisation of the charging profile. This will imply a modification of the diagram in *Figure 6-23* to decide when the optimisation is requested to update the charge profile.

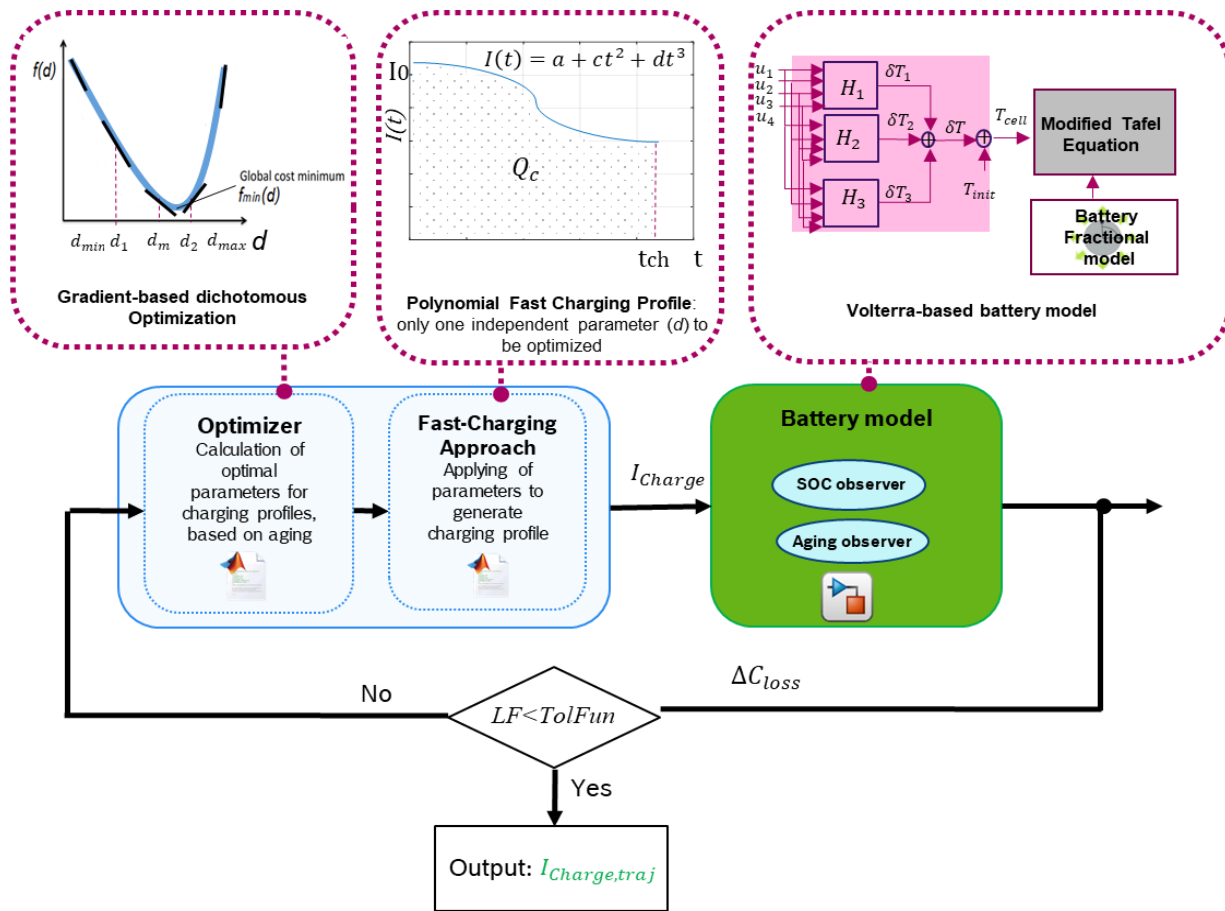


Figure 6-23 Charging profile optimization framework using the concepts introduced in chapter 5 and 6

Chapter 7

Conclusion and future work

This research was conducted at *Bosch Battery Systems GmbH* in collaboration with *IMS* laboratory (Laboratoire de l'Intégration du Matériau au Système) at University of Bordeaux between October 2015 and October 2018. The main goals of this study was to develop concepts, functions and models to improve the state of the art battery models and algorithms used in Battery Management Systems (BMS). The case study was a prismatic Li-ion cell for application of Plug-in Hybrid Electric Vehicles. The conventional battery management strategies employ extremely conservative methods to adapt the battery operation and thus do not use the maximum available energy of the battery. This problem is addressed in this work by proposing novel algorithms that permit to utilize the maximum capacity in an efficient way. Furthermore the developed models facilitate better understanding, prediction and control of the states of the battery in a wide operating range.

In Chapter 2, comprehensive literature review is done on the different battery modelling approaches. The existing modelling methods are briefly introduced and respective advantages and disadvantages are compared. In section 2.3 , a single particle fractional order model is presented. It is based on Fick's first law of diffusion. The analytical solution of the governing diffusion equation results in a fractional order transfer function, which is able to precisely capture the dynamics of the system at lower frequencies which the operating frequency of BMS lies. However the problem is model implementation on the digital battery control unit, where requires the functions to be discretizable. For this reason, using Oustaloup recursive algorithm, the fractional order transfer function of the system is converted to an integer order transfer function with a very similar behavior in the frequency domain. Subsequently, the model is calibrated using some measurement results and literature parameters. Validation tests are carried out by imposing real world driving cycles and the accuracy of the model in simulating the battery behavior is compared to the convenient battery modeling approach of Equivalent Circuit Model (ECM). From the simulation results shown in section 2.3.2 Model validation, it can be deduced that the fractional order model is more accurate than ECM approach while having a comparable computational efficiency. It also provides the possibility to interpret the battery behavior based on physics and electrochemistry.

Chapter 3 deals with developing a new algorithm to assign a function to the Open Circuit Potential (OCP) of the electrodes (half-cell) and similarly to the Open Circuit Voltage (OCV) on the full cell level. OCV has a significant contribution in the terminal voltage and varies notably over the battery lifetime. Thus the algorithm takes the aging into account and models the full cell OCV out of half-cell OCP measurement data using a polynomial function. In section 3.6 Aging correction of OCV curve at MOLthe algorithm is verified by comparing the measured and modeled OCV, where a good accuracy is achieved. The observed deviations of the simulation from the measurement are attributed to neglecting the heterogeneity of the cell surface.

Due to strong influence of aging on the battery behavior, Chapter 4 is dedicated to better understanding and modeling of degradation mechanisms. Firstly a general review of the various aging mechanisms is given. In section 4.2.2 Aging Model, by interpreting the aging measurement results of the studied battery, its underlying aging phenomena are determined. Cell temperature is identified as an influencing factor on aging, thus a lumped-parameter thermal model of the cell is implemented. Subsequently, a modified aging model is proposed that features decoupling of calendar and cycling aging. Additionally, it can show the dependency of degradation mechanisms (in terms of capacity loss) as a function of SOC, temperature and C-rate. It is a very important aspect of the aging model that permits to distinguish the root-cause of the capacity loss, especially applicable for aging control of batteries during aggressive fast charging cycles which is discussed in Chapter 5. In section 4.3 , the thermal and aging model and the fractional order electrical model from Chapter 2 are coupled together to form a unified ‘‘electro-thermal aging’’ battery model. Several validation test results are demonstrated to justify the model accuracy.

Chapter 5 is focused on designing an intelligent charging controller to reach the fast charging target while minimizing the degradation effects. As the first step towards implementing the charging controller, offline trajectory planning is performed to obtain the optimal charging profiles and respective side reaction current under different conditions, covering the whole operating range of the battery. The optimal charging profiles are compared to the convenient CCCV charging strategy (Figure 5-2), where using the optimal profiles up to 15% reduction in aging is achieved. The collected trajectories are scaled versus SOC and kept in lookup tables to be used in a feedforward controller for initializing the model and providing reference signal. The trajectory planning is based on the assumption of a perfectly known cell, which is not always the case and thus applying an optimized charging current does not necessarily result in reaching the target SOC

with minimum aging. Therefore a closed-loop strategy should be developed. For this purpose, the uncertain linear model of the nonlinear system is derived, where a big uncertainty both in the magnitude and phase of the system Bode plot is observed (Figure 5-4). Thus a robust closed-loop control strategy is required to deal with this large parametric uncertainty. Later on, concept of CRONE methodology is introduced as a good candidate to achieve intelligent charging targets. CRONE control strategy involves in optimization of fractional differentiation orders as design parameters in frequency domain. Third generation of CRONE controller is parameterized based on the closed-loop system design specifications. The closed-loop CRONE controller and feedforward controller are interconnected and an anti-windup block is integrated to the overall system to account for integral accumulation error. In the following sections, the robustness of the controller is examined by applying uncertainties in the operating conditions and battery model parameters. The controller has shown a very good tracking of the optimal side reaction current profile (to minimize aging) while achieving the fast charging target (5-80% SOC) in the desired charging time of 20 minutes (Figure 5-17). Despite the good results obtained from the closed-loop intelligent charging strategy, the control loop is not easily implementable for onboard application such as BMS. The optimization algorithm to obtain the side reaction and optimal charging profile trajectories involves a nonlinear optimization routine with large number of parameters. Such an approach is computationally expensive and thus the next chapter deals with the design of an efficient profile optimization method.

Chapter 6 deals with possible simplifications of the intelligent charging process to permit its application under real-time conditions. The simplifications are considered firstly in the definition of the charging profiles. According to this proposal, two semi-empirical shapes (affine and polynomial) are identified for the optimal charging current. The profiles are applied to the model and good performance is achieved comparing to other convenient charging profiles. In the second part, the structure of the model is simplified by linearization of the Butler-Volmer sub-system and replacing the thermal sub-system using Volterra series. From the validation test shown in section 6.2.2.1 , it can be concluded that the capacity loss estimated by the Volterra-based simplified model and the original nonlinear model are in a good agreement while the simulation time of the Volterra-based model is reduced significantly by 37%. In the third part, a user-defined optimization strategy is proposed to replace *fmincon* (Matlab built-in optimizer) in the framework of intelligent charging. The main advantage is that the user-defined optimizer is straight-forward

and easily realizable for onboard application. In another validation test, the optimized values of capacity loss using the newly proposed optimization method are compared to the ones by *fmincon* and the obtained results are in a good agreement.

Further studies can be conducted to include the electrolyte dynamics into the electrical fractional-order model. In Chapter 2, only the high frequency resistance of the cell is accounted for the influence of electrolyte on the cell behaviour. However, considering the ion diffusion phenomenon inside the electrolyte would increase the model accuracy in estimation of the terminal voltage.

In Chapter 3, considering the heterogeneity of the electrode surface would increase the accuracy of OCV modelling. This idea can be realized by investigating the influence of aging on the OCP of electrodes.

A comprehensive aging model can be accomplished by implementing a mechanical model of the cell, taking into account the fracture formation and mechanical pressure. The cell mechanical model should be then coupled to the proposed electro-thermal aging model in Chapter 4. With this extension, one can predict the cell behaviour under long-term cycling and its EOL.

For a future in context of Chapter 5, a control problem considering a fixed aging rate to minimize the charging time can be formulated and respective trajectories can be obtained. Moreover by means of sensitivity analysis on the trajectories, best aging criteria in terms of observability (for example anode potential) can be figured out to be used as the controlled signal and for design of a charging controller.

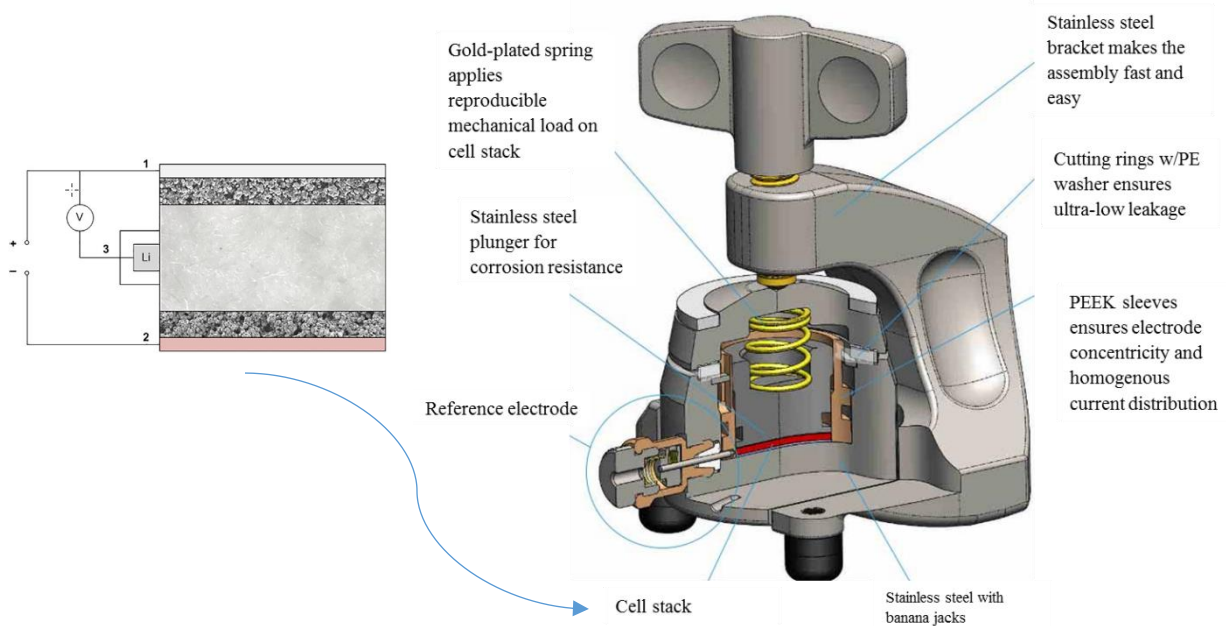
Volterra series are employed for further simplification of the nonlinear model in Chapter 6. This will permit its application under real-time conditions for example on the controller of the BMS. However other methods such as multiple model approach can be applied to obtain a simplified model. Multiple model approach is also a powerful tool for modeling a large class of nonlinear systems. It involves in decomposition of the operating space and finding an appropriate weighting function for each sub-system in a specific operating space.

Most of the proposed algorithms and methods in this thesis were validated by means of simulations. Evaluation of the internal battery states is not possible using real cell and measurement, but simulation provides this possibility. However, importance of experimental validations cannot be ignored and thus should be pursued in a future work. Upon successful

validation of simulation results presented in this work, the electro-thermal aging battery model and the intelligent charging strategy can be implemented as a part of a BMS.

Appendix A - ELcell setup

EL-CELL ECC-Combi measurement device, shown in Figure 3-1 is briefly described in this appendix. This measurement setup can provide two different modes, firstly the electrochemical test for two-electrode battery testing referred as ECC-Std. The most typical application in this mode is the characterization of a lithium-ion battery electrode (anode or cathode) against a lithium metal counter electrode. The second mode of usage, referred as ECC-Ref is for electrochemical test cell with reference electrode. A typical application in this case is the characterization of a full lithium-ion battery (e.g. graphite anode and lithium metal oxide cathode) with a lithium metal reference. The experimental setup used for half-cell potential measurements using a reference electrode in ECC-Ref mode is shown in the following figure where it comprises of a 3 electrode configuration (1: working electrode, 2: counter electrode and 3: reference electrode. It is used to measure the open circuit potential of the coin cells by applying charging/discharging current of $C/50$. The cross-section of the measurement setup with its main components is presented in on the right side of the figure. A detailed explanation about the usage of the setup can be found in the device manual available on the manufacturer website. [96]



References

- [1] Eckhard Karden, Ed., *Microhybrid Goes Mainstream: Battery Selection and Trends*, 2011.
- [2] P. Huang, Q. Wang, K. Li, P. Ping, and J. Sun, “The combustion behavior of large scale lithium titanate battery,” (eng), *Scientific reports*, vol. 5, p. 7788, 2015.
- [3] K. M. Colbow, J. R. Dahn, and R. R. Haering, “Structure and electrochemistry of the spinel oxides LiTi_2O_4 and $\text{Li}_4\text{Ti}_5\text{O}_{14}$,” *Journal of Power Sources*, vol. 26, no. 3-4, pp. 397–402, 1989.
- [4] T. Horiba, “Lithium-Ion Battery Systems,” *Proc. IEEE*, vol. 102, no. 6, pp. 939–950, 2014.
- [5] Green Car Congress, *Porsche introducing new plug-in Cayenne S E-Hybrid SUV; third plug-in from Porsche*, 2014.
- [6] R. Hu, “Battery Management System For Electric Vehicle Applications,”
- [7] “Battery Management Systems,” in *Battery Systems Engineering*, C. D. Rahn and C.-Y. Wang, Eds., Oxford, UK: John Wiley & Sons Ltd, 2013, pp. 191–229.
- [8] C. D. Rahn and C.-Y. Wang, Eds., *Battery Systems Engineering*. Oxford, UK: John Wiley & Sons Ltd, 2013.
- [9] 06120, Jens Groot, 031-3220983, CTP9D, “State-of-Health Estimation of Li-ion Batteries: Cycle Life Test Methods,”
- [10] S. Buller, M. Thele, E. Karden, and R. W. de Doncker, “Impedance-based non-linear dynamic battery modeling for automotive applications,” *Journal of Power Sources*, vol. 113, no. 2, pp. 422–430, 2003.
- [11] A. Seaman, T.-S. Dao, and J. McPhee, “A survey of mathematics-based equivalent-circuit and electrochemical battery models for hybrid and electric vehicle simulation,” *Journal of Power Sources*, vol. 256, pp. 410–423, 2014.
- [12] G. L. Plett, *Battery management systemsnVolume 2*. Boston, London: Artech House, 2016.
- [13] S. Buller, M. Thele, R. DeDoncker, and E. Karden, “Impedance-Based Simulation Models of Supercapacitors and Li-Ion Batteries for Power Electronic Applications,” *IEEE Trans. on Ind. Applicat.*, vol. 41, no. 3, pp. 742–747, 2005.
- [14] A. Fotouhi, D. J. Auger, K. Propp, S. Longo, and M. Wild, “A review on electric vehicle battery modelling: From Lithium-ion toward Lithium–Sulphur,” *Renewable and Sustainable Energy Reviews*, vol. 56, pp. 1008–1021, 2016.

- [15] J. S. Newman and K. E. Thomas-Alyea, *Electrochemical systems*, 3rd ed. Hoboken, N.J., Chichester: Wiley, 2004.
- [16] A. Jokar, B. Rajabloo, M. Désilets, and M. Lacroix, “Review of simplified Pseudo-two-Dimensional models of lithium-ion batteries,” *Journal of Power Sources*, vol. 327, pp. 44–55, 2016.
- [17] K. A. Smith, “Electrochemical Modeling, Estimation and Control of Lithium Ion Batteries,” PhD dissertation, Pennsylvania state university, 2006.
- [18] *2014 International Conference on Fractional Differentiation and its Applications (ICFDA)*.
- [19] M. Guo, G. Sikha, and R. E. White, “Single-Particle Model for a Lithium-Ion Cell: Thermal Behavior,” *J. Electrochem. Soc.*, vol. 158, no. 2, A122, 2011.
- [20] Jocelyn Sabatier, Mbala Junior Francisco, Franck Guillemard, *Proceedings of the 12th European Control Conference (ECC): July 17 -19, 2013, Zuerich, Switzerland*. Zürich, 2013.
- [21] J. Sabatier *et al.*, “Lithium-ion batteries modeling: A simple fractional differentiation based model and its associated parameters estimation method,” *Signal Processing*, vol. 107, pp. 290–301, 2015.
- [22] “Algorithms for Advanced Battery-Management Systems,” *IEEE Control Syst.*, vol. 30, no. 3, pp. 49–68, 2010.
- [23] W.B. Gu and C.Y. Wang, “Thermal-electrochemical coupled modeling of a lithium ion cell,” vol. 99-25, pp. 748–762, 2000.
- [24] J. Li, N. Lotfi, R. G. Landers, and J. Park, “A Single Particle Model for Lithium-Ion Batteries with Electrolyte and Stress-Enhanced Diffusion Physics,” *J. Electrochem. Soc.*, vol. 164, no. 4, A874-A883, 2017.
- [25] G. G. Botte, “Influence of Some Design Variables on the Thermal Behavior of a Lithium-Ion Cell,” *J. Electrochem. Soc.*, vol. 146, no. 3, p. 914, 1999.
- [26] G. K. Prasad and C. D. Rahn, “Model based identification of aging parameters in lithium ion batteries,” *Journal of Power Sources*, vol. 232, pp. 79–85, 2013.
- [27] Mathieu MERVEILLAUT, “ESTIMATION DE L’ETAT DE CHARGE D’UN ACCUMULATEUR LITHIUM-ION A BASE D’OBSERVATEUR,” PhD Dissertation, Laboratoire de l’Intégration du Matériau au Système, Talence, France, 2010.
- [28] Oustaloup A., Melchior P., Lanusse P., Cois O., Dancla F., Ed., *The CRONE toolbox for Matlab*, 2000.

- [29] J. Sabatier, “Solutions to the Sub-Optimality and Stability Issues of Recursive Pole and Zero Distribution Algorithms for the Approximation of Fractional Order Models,” *Algorithms*, vol. 11, no. 7, p. 103, 2018.
- [30] M. Doyle, J. P. Meyers, and J. Newman, “Computer Simulations of the Impedance Response of Lithium Rechargeable Batteries,” *J. Electrochem. Soc.*, vol. 147, no. 1, p. 99, 2000.
- [31] J. Callis, *Final Report*, 2016.
- [32] L. K. Frevel and L. J. Kressley, “Modifications in Mercury Porosimetry,” *Anal. Chem.*, vol. 35, no. 10, pp. 1492–1502, 1963.
- [33] maarten, “Autolab_Application_Note_BAT03,”
- [34] B. Müller and G. Meyer, *Electric vehicle systems architecture and standardization needs: Reports of the PPP European Green Vehicles Initiative*. Cham: Springer, 2015.
- [35] M. T. McDowell, S. W. Lee, W. D. Nix, and Y. Cui, “25th anniversary article: Understanding the lithiation of silicon and other alloying anodes for lithium-ion batteries,” (eng), *Advanced materials (Deerfield Beach, Fla.)*, vol. 25, no. 36, pp. 4966–4985, 2013.
- [36] A. A. Hussein, “Kalman Filters versus Neural Networks in Battery State-of-Charge Estimation: A Comparative Study,” *IJMNTA*, vol. 03, no. 05, pp. 199–209, 2014.
- [37] J. P. Schmidt, H. Y. Tran, J. Richter, E. Ivers-Tiffée, and M. Wohlfahrt-Mehrens, “Analysis and prediction of the open circuit potential of lithium-ion cells,” *Journal of Power Sources*, vol. 239, pp. 696–704, 2013.
- [38] Y.-S. Lee, M. Liu, C.-C. Sun, and M.-W. Cheng, “State-of-charge estimation with aging effect and correction for lithium-ion battery,” *IET Electrical Systems in Transportation*, vol. 5, no. 2, pp. 70–76, 2015.
- [39] K. Honkura, H. Honbo, Y. Koishikawa, and T. Horiba, “State Analysis of Lithium-Ion Batteries Using Discharge Curves,” in *ECS Transactions*, Phoenix, AZ, 2008, pp. 61–73.
- [40] M. Dubarry and B. Y. Liaw, “Identify capacity fading mechanism in a commercial LiFePO₄ cell,” *Journal of Power Sources*, vol. 194, no. 1, pp. 541–549, 2009.
- [41] D. K. Karthikeyan, G. Sikha, and R. E. White, “Thermodynamic model development for lithium intercalation electrodes,” *Journal of Power Sources*, vol. 185, no. 2, pp. 1398–1407, 2008.

- [42] D. K. Karthikeyan, G. Sikha, and R. E. White, “Thermodynamic model development for lithium intercalation electrodes,” *Journal of Power Sources*, vol. 185, no. 2, pp. 1398–1407, 2008.
- [43] V. Pop *et al.*, “Battery Aging and Its Influence on the Electromotive Force,” *J. Electrochem. Soc.*, vol. 154, no. 8, A744, 2007.
- [44] V. Pop *et al.*, “Battery Aging and Its Influence on the Electromotive Force,” *J. Electrochem. Soc.*, vol. 154, no. 8, A744, 2007.
- [45] P. Ramadass, B. Haran, P. M. Gomadam, R. White, and B. N. Popov, “Development of First Principles Capacity Fade Model for Li-Ion Cells,” *J. Electrochem. Soc.*, vol. 151, no. 2, A196, 2004.
- [46] M. T. Lawder, P. W. C. Northrop, and V. R. Subramanian, “Model-Based SEI Layer Growth and Capacity Fade Analysis for EV and PHEV Batteries and Drive Cycles,” *Journal of the Electrochemical Society*, vol. 161, no. 14, A2099-A2108, 2014.
- [47] A. Barré *et al.*, “A review on lithium-ion battery ageing mechanisms and estimations for automotive applications,” *Journal of Power Sources*, vol. 241, pp. 680–689, 2013.
- [48] J. Vetter *et al.*, “Ageing mechanisms in lithium-ion batteries,” *Journal of Power Sources*, vol. 147, no. 1-2, pp. 269–281, 2005.
- [49] V. Agubra and J. Fergus, “Lithium Ion Battery Anode Aging Mechanisms,” (eng), *Materials (Basel, Switzerland)*, vol. 6, no. 4, pp. 1310–1325, 2013.
- [50] P. Liu *et al.*, “Aging Mechanisms of LiFePO₄ Batteries Deduced by Electrochemical and Structural Analyses,” *J. Electrochem. Soc.*, vol. 157, no. 4, A499, 2010.
- [51] dli, “Microsoft Word - thesis defense dongjiang Li 5.docx,”
- [52] M. Ecker *et al.*, “Calendar and cycle life study of Li(NiMnCo)O₂-based 18650 lithium-ion batteries,” *Journal of Power Sources*, vol. 248, pp. 839–851, 2014.
- [53] J. Xu, R. D. Deshpande, J. Pan, Y.-T. Cheng, and V. S. Battaglia, “Electrode Side Reactions, Capacity Loss and Mechanical Degradation in Lithium-Ion Batteries,” *J. Electrochem. Soc.*, vol. 162, no. 10, A2026-A2035, 2015.
- [54] X. Jin *et al.*, “Physically-based reduced-order capacity loss model for graphite anodes in Li-ion battery cells,” *Journal of Power Sources*, vol. 342, pp. 750–761, 2017.
- [55] B. Shabani and M. Biju, “Theoretical Modelling Methods for Thermal Management of Batteries,” *Energies*, vol. 8, no. 9, pp. 10153–10177, 2015.

- [56] W.-Y. Chang, "The State of Charge Estimating Methods for Battery: A Review," *ISRN Applied Mathematics*, vol. 2013, no. 5, pp. 1–7, 2013.
- [57] Z. Deng *et al.*, "Electrochemical Impedance Spectroscopy Study of a Lithium/Sulfur Battery: Modeling and Analysis of Capacity Fading," *J. Electrochem. Soc.*, vol. 160, no. 4, A553–A558, 2013.
- [58] G. L. Plett, "Extended Kalman filtering for battery management systems of LiPB-based HEV battery packs," *Journal of Power Sources*, vol. 134, no. 2, pp. 277–292, 2004.
- [59] P. Ramadass, B. Haran, R. White, and B. N. Popov, "Mathematical modeling of the capacity fade of Li-ion cells," *Journal of Power Sources*, vol. 123, no. 2, pp. 230–240, 2003.
- [60] M. Ecker *et al.*, "Development of a lifetime prediction model for lithium-ion batteries based on extended accelerated aging test data," *Journal of Power Sources*, vol. 215, pp. 248–257, 2012.
- [61] G. Ning, R. E. White, and B. N. Popov, "A generalized cycle life model of rechargeable Li-ion batteries," *Electrochimica Acta*, vol. 51, no. 10, pp. 2012–2022, 2006.
- [62] H. Akaike, "A new look at the statistical model identification," *IEEE Trans. Automat. Contr.*, vol. 19, no. 6, pp. 716–723, 1974.
- [63] Rampyari, "A COMPREHENSIVE REVIEW ON LI-ION BATTERY AGEING ESTIMATION TECHNIQUES FOR GREEN ENERGY VEHICLES,"
- [64] M. B. Pinson and M. Z. Bazant, "Theory of SEI Formation in Rechargeable Batteries: Capacity Fade, Accelerated Aging and Lifetime Prediction," *J. Electrochem. Soc.*, vol. 160, no. 2, A243–A250, 2012.
- [65] R. Narayanrao, M. M. Joglekar, and S. Inguva, "A Phenomenological Degradation Model for Cyclic Aging of Lithium Ion Cell Materials," *J. Electrochem. Soc.*, vol. 160, no. 1, A125–A137, 2012.
- [66] R. Deshpande, M. Verbrugge, Y.-T. Cheng, J. Wang, and P. Liu, "Battery Cycle Life Prediction with Coupled Chemical Degradation and Fatigue Mechanics," *J. Electrochem. Soc.*, vol. 159, no. 10, A1730–A1738, 2012.
- [67] W. Imamura, N. Eda, K. Tanaka, H. Horie, and H. Akimoto, "Capacity fade model of Lithium-ion batteries for Practical use," 2011.

- [68] A. V. Randall, R. D. Perkins, X. Zhang, and G. L. Plett, "Controls oriented reduced order modeling of solid-electrolyte interphase layer growth," *Journal of Power Sources*, vol. 209, pp. 282–288, 2012.
- [69] P. Guan, L. Liu, and X. Lin, "Simulation and Experiment on Solid Electrolyte Interphase (SEI) Morphology Evolution and Lithium-Ion Diffusion," *Journal of the Electrochemical Society*, vol. 162, no. 9, A1798-A1808, 2015.
- [70] K. Uddin, S. Perera, W. Widanage, L. Somerville, and J. Marco, "Characterising Lithium-Ion Battery Degradation through the Identification and Tracking of Electrochemical Battery Model Parameters," *Batteries*, vol. 2, no. 2, p. 13, 2016.
- [71] S. Mohajer, J. Sabatier, P. Lanusse, and O. Cois, "A Fractional-Order Electro-Thermal Aging Model for Lifetime Enhancement of Lithium-ion Batteries," *IFAC-PapersOnLine*, vol. 51, no. 2, pp. 220–225, 2018.
- [72] T. T. Vo, X. Chen, W. Shen, and A. Kapoor, "New charging strategy for lithium-ion batteries based on the integration of Taguchi method and state of charge estimation," *Journal of Power Sources*, vol. 273, pp. 413–422, 2015.
- [73] A. Abdollahi *et al.*, "Optimal battery charging, Part I: Minimizing time-to-charge, energy loss, and temperature rise for OCV-resistance battery model," *Journal of Power Sources*, vol. 303, pp. 388–398, 2016.
- [74] H. E. Perez, X. Hu, S. Dey, and S. J. Moura, "Optimal Charging of Li-Ion Batteries With Coupled Electro-Thermal-Aging Dynamics," *IEEE Trans. Veh. Technol.*, vol. 66, no. 9, pp. 7761–7770, 2017.
- [75] S.-Y. Choe, X. Li, and M. Xiao, "Fast charging method based on estimation of ion concentrations using a reduced order of Electrochemical Thermal Model for lithium ion polymer battery," in *2013 World Electric Vehicle Symposium and Exhibition (EVS27)*, Barcelona, Spain, pp. 1–11.
- [76] Reinhardt Klein *et al.*, *American Control Conference (ACC), 2011: June 29 - July 1 2011, San Francisco, CA, USA*. Piscataway, NJ: IEEE, 2011.
- [77] J. Yan, G. Xu, H. Qian, Y. Xu, and Z. Song, "Model Predictive Control-Based Fast Charging for Vehicular Batteries," *Energies*, vol. 4, no. 12, pp. 1178–1196, 2011.

- [78] T. Ikeya *et al.*, “Multi-step constant-current charging method for an electric vehicle nickel/metal hydride battery with high-energy efficiency and long cycle life,” *Journal of Power Sources*, vol. 105, no. 1, pp. 6–12, 2002.
- [79] J. Sabatier, P. Lanusse, P. Melchior, and A. Oustaloup, *Fractional order differentiation and robust control design: CRONE, H-infinity and motion control / Jocelyn Sabatier, Patrick Lanusse, Pierre Melchior, Alain Oustaloup ; with contributions by chapter 1: C. Farges, chapter 3: D.Nelson Gruel, chapter 4: L. Fadiga, chapter 5: S. Victor*. Dordrecht: Springer, 2015.
- [80] H. W. Bode, *Network analysis and feedback amplifier design*, 14th ed. Huntington N.Y.: R. E. Krieger Pub. Co, 1975, 1945.
- [81] V. Pommier, J. Sabatier, P. Lanusse, and A. Oustaloup, “Crone control of a nonlinear hydraulic actuator,” *Control Engineering Practice*, vol. 10, no. 4, pp. 391–402, 2002.
- [82] Patrick Lanusse, *CRONE Control System Design, a CRONE toolbox for Matlab*. [Online] Available: <http://www.ims-bordeaux.fr/CRONE/toolbox>.
- [83] J.A. Mas, *Proceedings of the Second International Electric Vehicle Symposium*, 223–246., 1971.
- [84] Y.-H. Liu, J.-H. Teng, and Y.-C. Lin, “Search for an Optimal Rapid Charging Pattern for Lithium–Ion Batteries Using Ant Colony System Algorithm,” *IEEE Trans. Ind. Electron.*, vol. 52, no. 5, pp. 1328–1336, 2005.
- [85] V. Volterra, *Theory of functionals and of integral and integro-differential equations*. Mineola N.Y.: Dover Publications, 2005.
- [86] J. Arruda and J. Santos, “Mechanical joint parameter estimation using frequency response functions and component mode synthesis,” *Mechanical Systems and Signal Processing*, vol. 7, no. 6, pp. 493–508, 1993.
- [87] Z. Q. Lang, X. J. Jing, S. A. Billings, G. R. Tomlinson, and Z. K. Peng, “Theoretical study of the effects of nonlinear viscous damping on vibration isolation of sdof systems,” *Journal of Sound and Vibration*, vol. 323, no. 1-2, pp. 352–365, 2009.
- [88] R. Ishikawa, J. Kimura, and K. Honjo, “Analytical Design Method for a Low-Distortion Microwave InGaP/GaAs HBT Amplifier Based on Transient Thermal Behavior in a GaAs Substrate,” *IEEE Trans. Compon., Packag. Manufact. Technol.*, vol. 3, no. 10, pp. 1705–1712, 2013.

- [89] R. Kumar, A. Banerjee, B. C. Vemuri, and H. Pfister, “Trainable Convolution Filters and Their Application to Face Recognition,” (eng), *IEEE transactions on pattern analysis and machine intelligence*, vol. 34, no. 7, pp. 1423–1436, 2012.
- [90] J. K. Gruber, C. Bordons, and A. Oliva, “Nonlinear MPC for the airflow in a PEM fuel cell using a Volterra series model,” *Control Engineering Practice*, vol. 20, no. 2, pp. 205–217, 2012.
- [91] C. M. Cheng, Z. K. Peng, W. M. Zhang, and G. Meng, “Volterra-series-based nonlinear system modeling and its engineering applications: A state-of-the-art review,” *Mechanical Systems and Signal Processing*, vol. 87, pp. 340–364, 2017.
- [92] J. C. P. JONES and S. A. Billings, “Recursive algorithm for computing the frequency response of a class of non-linear difference equation models,” *International Journal of Control*, vol. 50, no. 5, pp. 1925–1940, 1989.
- [93] W. J. Rugh, *Nonlinear system theory: The Volterra/Wiener approach / Wilson J. Rugh*. Baltimore, London: Johns Hopkins University Press, 1981.
- [94] S. P. Boyd and L. Vandenberghe, *Convex optimization*. Cambridge: Cambridge University Press, 2004.
- [95] R. Orjuela, B. Marx, J. Ragot, and D. Maquin, “Nonlinear system identification using heterogeneous multiple models,” *International Journal of Applied Mathematics and Computer Science*, vol. 23, no. 1, 2013.
- [96] EL-CELL GmbH, *User Manual ECC-Ref: Electrochemical test cell*. [Online] Available: https://el-cell.com/wp-content/uploads/downloads/manuals/Manual_ECC_Std_Release_3.8.pdf.